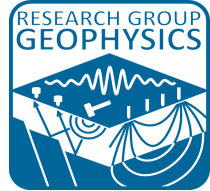




TECHNISCHE
UNIVERSITÄT
WIEN



MASTERARBEIT

Electrical imaging for cave detection: numerical and field studies

zur Erlangung des akademischen Grades

Diplom-Ingenieurin

im Rahmen des Studiums

Geodäsie und Geoinformation

eingereicht von

Barbara Funk

Matrikelnummer 09509540

ausgeführt am Department für Geodäsie und Geoinformation, Forschungsgruppe: Geophysik
der Fakultät für Mathematik und Geoinformation der Technischen Universität Wien

Betreuer: Ass.-Prof. Dr.rer.nat. Adrian Flores-Orozco

Wien, 25.03.2019

(Unterschrift Verfasserin)

(Unterschrift Betreuer)

Contents

Abstract	5
Zusammenfassung	6
1 Introduction	7
1.1 Physical principles	10
2 Methods	12
2.1 Electrical resistivity tomography and induced polarisation	12
2.2 Electromagnetics - CMD	16
2.3 Ground penetrating radar	17
3 Numeric Models	19
3.1 Methods	19
3.2 Models	19
3.2.1 Configuration	20
3.2.2 Detection limits	22
3.2.3 Proof of concept	24
4 Case studies	27
4.1 Die Höhle: Anwendung geophysikalischer Methoden zur Detektion zweier Höhlen nahe Lunz am See (NÖ)	27
4.2 Measurements	37
4.3 Evaluation and Results	37
4.3.1 Profile coordinates	38
4.3.2 ERT/IP	39
4.3.3 CMD	50
4.3.4 GPR	54
5 How to build electrical models from real data in speleology	57
5.1 Cave survey	57
5.2 Comparison	59
5.2.1 Profile 1	60
5.2.2 Profile 2	62
5.2.3 Profile 3	62
5.2.4 Profile 4	64
5.2.5 Profile 5	67
5.2.6 Profile 6	67
5.2.7 Profile 7	69
6 Summary and outlook	72
7 Acknowledgement	74

Abstract

Within the scope of this diploma thesis, the imaging geophysical methods Electrical Resistivity Tomography (ERT) and Ground Penetrating Radar (GPR) were carried out to detect near-surface cavities in two areas. The areas under investigation are located south-west of Lunz am See in the Northern Calcareous Alps and include two caves, the Stiegengraben-Wasserhöhle and the Forststraßeneinbruch. The Stiegengraben-Wasserhöhle has a length of 1 km and was buried with gravel in the 1970s during the construction of a forest road. Here, it is feared that the water pressure will mobilize the unconsolidated material by clogging the episodically active source cave, resulting in a debris-flow and endangering the houses in the valley below. The goal of the geophysical survey was to identify the exact location of the former cave entrance. Both geophysical methods (GPR and ERT) were able to locate the entrance of the Stiegengraben-Wasserhöhle. In addition, the ERT pictures show that probably already larger amounts of sediment and/or water have accumulated in the entrance hall of the Stiegengraben-Wasserhöhle.

The Forststraßeneinbruch was first mentioned in December 2016 due to a hole in a forest road. The purpose of this geophysical survey was to verify that the known cavities of the Forststraßeneinbruch are detectable by geophysical methods. It was also possible to search for additional cavities close to the surface, areas which are threatened by a collapse on the forest road as well. With one exception, the ERT images show clear contrasts in the physical properties of the subsoil, where known cavities are present. By modelling the known cave parts it was shown that these correspond very well with the anomalies of the ERT images. In two areas, however, very high contrasts were found, although no corresponding chamber of the Forststraßeneinbruch is known yet. This might give a hint to the existence of additional, yet unknown cavities.

Zusammenfassung

Im Rahmen dieser Diplomarbeit wurden in zwei Gebieten Messungen mittels der bildgebenden geophysikalischen Methoden Geoelektrik (Electrical Resistivity Tomography, ERT) und Georadar (Ground Penetrating Radar, GPR) durchgeführt, um oberflächennahe Hohlräume zu detektieren. Die Untersuchungsgebiete liegen südwestlich von Lunz am See in den Nördlichen Kalkvoralpen und umfassen zwei Höhlen, den Forststraßeneinbruch und die Stiegengraben-Wasserhöhle. Die auf eine Länge von 1 km vermessene Stiegengraben-Wasserhöhle wurde in den 1970er Jahren beim Bau einer Forststraße mit großen Blöcken und später mit großen Mengen an feinkörnigem Material zugeschüttet. Hier besteht die Befürchtung, dass der Wasserdruck durch das Verstopfen der episodisch aktiven Quellhöhle das unverfestigte Material mobilisiert, was zu einer Mure führen und die Häuser im Tal darunter gefährden könnte. Ziel der geophysikalischen Untersuchung war hier, die exakte Lage des ehemaligen Höhleneingangs zu identifizieren. Mit Hilfe der geophysikalischen Messungen konnte der verschüttete Eingang oberhalb der Stiegengraben-Wasserhöhle lokalisiert werden. Dabei konnte der Eingangsbereich sowohl auf den GPR als auch auf den ERT Bildern identifiziert werden. Außerdem zeigten die ERT Bilder, dass sich wohl bereits größere Mengen Sediment und/oder Wasser in der Eingangshalle der Stiegengraben-Wasserhöhle gesammelt haben.

Der Forststraßeneinbruch wurde im Dezember 2016 aufgrund eines in einer Forststraße eingebrochenen Lochs erstmals erwähnt. Ziel dieser geophysikalischen Untersuchung war es zu überprüfen, ob die bekannten Hohlräume des Forststraßeneinbruchs mit Hilfe geophysikalischer Methoden nachweisbar sind. Zusätzlich sollte dabei auch nach möglichen weiteren, oberflächennahen Hohlräumen gesucht werden, um eventuelle weitere, durch Einsturz bedrohte Bereiche auf der Forststraße feststellen zu können. Im Gegensatz zur Stiegengraben-Wasserhöhle konnten die tieferen und engräumigeren Hohlräume des Forststraßeneinbruchs mit Hilfe der GPR Messungen bis auf eine Ausnahme nicht erkannt werden. Die ERT-Bilder zeigen allerdings auch hier deutliche Kontraste in den physikalischen Eigenschaften des Untergrunds. Durch Modellierung der bekannten Höhlenteile konnte gezeigt werden, dass diese sehr gut mit den Anomalien der ERT-Bilder übereinstimmen. Bei zwei Bereichen wurden allerdings sehr hohe Kontraste festgestellt, obwohl sich dort kein bekannter Raum des Forststraßeneinbruchs befindet. Damit könnte man hier eventuell von der Existenz weiterer, noch unbekannter Hohlräume ausgehen.

1 Introduction

About 20% of Austria's surface area consists of water-soluble rocks such as limestone, dolomite or gypsum (Spötl et al., 2016). By far the largest region are the Northern Calcareous Alps, which also includes the study area near Lunz am See. Mountains that are built up by such rocks can karstify, which means that cavities of various sizes can form. Karst massifs are highly complex systems in which the water moves along different geological discontinuities that range in a broad spatial scale, from intragranular cracks (in the micro- to centimetre range) to fractures and caves systems, which can extend over kilometres. According to the flow behaviour, a karst system can be divided into a vadose (or unsaturated) zone, where the water descends by gravity and a phreatic (saturated) zone (see figure 1). In the latter case, all openings are completely water-filled and the water moves by a combination of gravity and pressure. The surface of the phreatic zone is often called karst water table. According to hydrologic events this water table fluctuates and this temporarily flooded zone is called epiphreatic. From some Alpine caves, fluctuations of up to 200 m were recorded (Spötl et al., 2016). The near-surface part of the vadose zone is called Epikarst and has a typical thickness of few meters (Williams, 1985). Pressure relief, increased corrosion and frost weathering create a dense network of expanded joints and cracks. The porosity can reach values of 5-10% and sometimes even more. Moreover, porosity in the host rock increases with water flow due to dissolution of the bulk rock, which may lead to a further increase in the porosity (Van Hoorn, 2017). The vadose zone below is characterized by gravitational water flow in a few larger solution-extended cavities and only reaches a porosity of up to 2%. Here, the water is usually flowing with a high speed and therefore almost no storage and filtering takes place. Since the flow rate in the vadose zone is significantly lower than in the epikarst, the vadose zone might retain groundwater during strong rain events. As a result, soil material and rock can be washed into the cavities of the epikarst, which act as a storage matrix and retain water by means of capillary forces. Thus, the epikarst can lead to water residence times of more than one year, for example Williams (2008) indicates residence times in the epikarst of 13 months. Although the isotopic composition of the precipitate varies greatly depending on the season, the dripping waters in most caves of the vadose zone below the epikarst showed little seasonal change and corresponded to the annual average of the precipitation isotope values (Williams & Fowler, 2002; Fairchild & Baker, 2012). Taking this into account, it is possible to assume a mixing of older and younger water in the epikarst. Lastly, the phreatic zone below the vadose zone is characterized by a complete filling of all pore spaces with water. In general, the flow velocity decelerates in the phreatic zone, which again leads to longer hydrological residence times. Since space and flow velocity are limited, the water is retained during snowmelt or strong rain events.

The study area is located in a strongly karstified region with many known caves, where the largest is the Stiegengraben Wasserhöhle, which was also one of the studied objects. The Stiegengraben Wasserhöhle was buried by gravel when a forest road was built in the 1970th. The cave acts as a spring during flood conditions but the water could escape through the coarse gravel. Not knowing the rare water activity of the cave, a lot of fine grained material was deposited on top of the coarse gravel recently. It is feared that due to this plugging of the spring the water pressure could rise and mobilize the unconsolidated material, which could result in a debris flow,

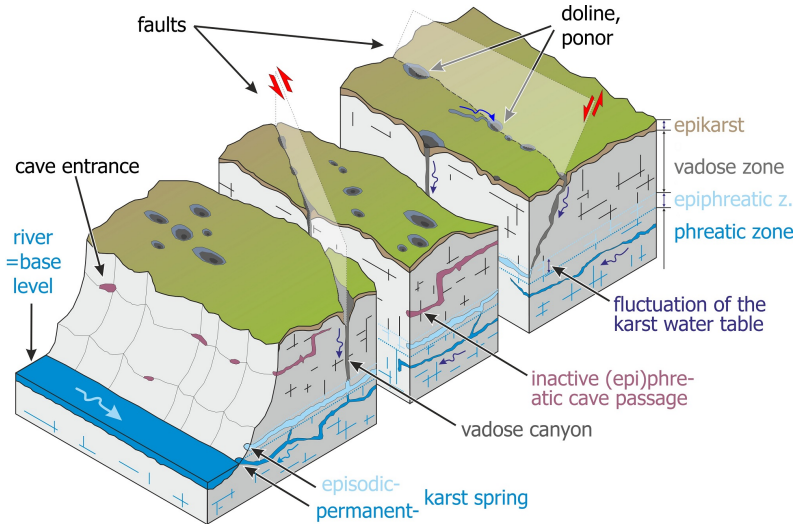


Figure 1: Highly simplified model of a karst massif showing the different hydrological zones (modified after Spötl et al. (2016)).

endangering the houses in the valley below. The aim of the geophysical measurements was the detection of the exact position of the former entrance in order to allow the planned reopening. The second studied object is another cave called Forststraßeneinbruch. Here a hole opened in a forest road and gave access to an underlying cave in December 2016 (figure 2).



Figure 2: Picture of the provisionally covered entrance of Forststraßeneinbruch, also visible the ERT instrument.

It was noticed that also other parts of the cave are close to the surface (adjacent to the forest road) as well. The aim of the geophysical surveys above this cave was to investigate whether geophysical methods can provide information on the location of areas that might collapse as well. A more detailed description of the two study objects and the geology of the study area can be found in the paper (section 4.1).

Geophysical methods offer the possibility to gain non-destructive quasi-continuous information about subsurface structures. In karst systems this may be of particular interest where near-surface cavities are suspected/possible but not accessible. Subsurface materials in karstic systems (limestone, air, water, clay) show strong contrasts in the electrical properties. Thus, electrical

Table 1: Dielectric constant (ϵ) and resistivity (ρ) of some materials expected in karst areas (upper part) and, for comparison, of some other rocks and minerals (lower part).

Material	ϵ	ρ [Ωm]
Limestone	4 - 8	100 - 10000
Air	1	$1.3 - 3.3 \cdot 10^{16}$
Gravel	2 - 3	1500 - 5000
Soil	4 - 30	20 - 9000
Clay	2 - 40	3 - 5000
Water	81	10 - 300
Dry sand	3 - 6	500 - 1500
Saturated sand	20 - 30	100 - 250
Granite	4 - 6	4000 - 2000000
Pyrite	80	< 1.5
Quartz	3.8	$10^1 0 - 10^{14}$

resistivity tomography and ground penetrating radar (GPR) are well established geophysical methods used for the delineation of underground cavities and karstic phenomena (e.g. Carrière et al., 2013; Martel et al., 2018, and references therein). Typical geological materials of the host rocks (e.g., limestones) are related to modest electrical resistivity values ($\rho > 500$ and $< 5000 \Omega\text{m}$); whereas karstic features such as caves and fractures can be linked to (i) an increase in the electrical resistivity values ($\rho > 100000 \Omega\text{m}$) due to conduits filled with air, which is an electrical insulator; or to (ii) a decrease in the electrical resistivity, associated to conduits filled with water, or with wet sediments. Hence, ERT and GPR methods exploit the contrasts in the electrical properties to delineate the geometry of karstic features, such as caves and sinkholes (Leucci & De Giorgi, 2005; Delle Rose & Leucci, 2010; Gómez-Ortiz & Martín-Crespo, 2012; Funk et al., 2018). Moreover, repetition of ERT measurements at different dates allow a time-resolved study of the electrical resistivity, for instance, to characterize water infiltration in karstic systems (Carrière et al., 2015; Watlet et al., 2018) and water flow in conduits and caves (Robert et al., 2012; Deceuster et al., 2013; Meyerhoff et al., 2014; Martel et al., 2018). Other geophysical methods such as seismics and gravimetry have also been deployed in karstic investigations, mostly as complementary techniques for the interpretation of GPR and ERT results (e.g. Chalikakis et al., 2011; Martínez-Moreno et al., 2014).

This work primarily made use of ERT and IP for the detection of cavities in the subsurface. A single geophysical measurement often do not provide an unambiguous solution of the subsurface structure, thus several geophysical methods are used to reduce ambiguities in the geophysical model. Therefore during the field work also measurements with GPR and electromagnetics (CMD) were carried out. The physical principles of these three geophysical methods will be briefly summarized in section 1.1. All of these methods (ERT, IP, GPR and CMD) react to changes in the electrical properties (dielectric constant and conductivity) in the subsurface. Table 1 (upper part) shows literature values (see Martinez & Byrnes, 2001; Knödel et al., 2005; Telford et al., 1990) for some materials expected in karst regions, whereat the large overlap of the values for different materials prevent an unambiguous interpretation. Some more rock specific sediment properties, such as porosity or saturation, play an important role for the used

geophysical methods as well. Table 1 (lower part) shows, for comparison, literature values of different kinds of rocks and minerals. The difference between dry and saturated sand clearly shows the important influence of the saturation. The large difference between pyrite and quartz exemplify the significant influence of metallic minerals on the resistivity.

1.1 Physical principles

This section briefly explains the physical principles of the three used geophysical methods (GPR, CMD, ERT/IP). The basis of all electromagnetic methods are the Maxwell equations (Maxwell, 1864), which are briefly described here:

- Gauß law: states that the electric charge density (ρ_q) is the source of the electric field:

$$\vec{\nabla} \cdot \vec{D} = \rho_q, \text{ with} \quad (1)$$

$$\vec{D} = \epsilon_0 \vec{E} + \vec{P} \text{ where} \quad (2)$$

\vec{D} = electric displacement field,

ϵ_0 = permittivity (dielectric constant),

\vec{E} = electric field,

\vec{P} = polarization density.

- Gauß law for magnetism: states that there are no magnetic monopoles:

$$\vec{\nabla} \cdot \vec{B} = 0, \text{ where} \quad (3)$$

\vec{B} = magnetic flux density.

- Law of induction: indicates that a changing magnetic displacement field leads to an electric field:

$$\vec{\nabla} \times \vec{E} = -\frac{\partial \vec{B}}{\partial t} \quad (4)$$

- Ampere's law: a changing electric field leads to a magnetic field:

$$\vec{\nabla} \times \vec{H} = \vec{j} + \frac{\partial \vec{D}}{\partial t}, \text{ with} \quad (5)$$

$$\vec{H} = \frac{1}{\mu_0} \vec{B} - \vec{M}, \text{ where} \quad (6)$$

\vec{H} = magnetic field,

\vec{j} = current density,

μ_0 = permeability,

\vec{M} = magnetization.

With the law of induction and Ampere's law, the functionality of electromagnetics can be described, in which variable magnetic fields induce currents in the conductive subsurface, which in turn induce magnetic fields (secondary magnetic fields). These can be measured to determine the conductivity of the subsurface (see section 2.2 for more details).

For DC methods (ERT) the Maxwell equations simplifies, since only stationary fields and point sources are used. Hence all time dependencies in the Maxwell equations disappear, which leads to the solution of the equations of electrostatics (Maurer, 2007):

$$U(r) = \frac{I}{4\pi\sigma r}, \text{ where} \quad (7)$$

U = Voltage,

I = Current,

r = distance from the point source,

σ = conductivity.

In addition, polarization effects occur in the subsurface also in DC methods, which leads to the effects of induced polarization (IP)(see section 2.1 for more details).

GPR is based on the reflection of electromagnetic waves at boundaries between two materials with different electrical properties (μ , ϵ , σ) and hence different propagation velocities. The wave properties (velocity (v), attenuation (α), electromagnetic impedance (Z)) can be written as follows (Everett, 2013):

$$\begin{aligned} v &= \frac{c}{\sqrt{\epsilon}} \\ \alpha &= \frac{\mu\sigma v}{2}, \text{ where} \\ Z &= \sqrt{\frac{\mu}{\epsilon}} \end{aligned} \quad (8)$$

c = speed of light.

At such a boundary one part of the electromagnetic wave is reflected and another is transmitted, the reflection coefficient (R) respectively the transmission coefficient (T) indicating the ratio of the amplitudes between incident and reflected respectively incident and transmitted waves (Butler, 2005). Reflection and transmission work according to Snell's law respectively to the law of reflection:

$$\begin{aligned} k_1 \cdot \sin\Theta_e &= k_2 \cdot \sin\Theta_d \\ \Theta_e &= \Theta_r, \text{ where} \end{aligned} \quad (9)$$

k_1, k_2 = refractivity of material 1 respectively material 2,

Θ_e = incidence angle,

Θ_d = angle of transmitted wave,

Θ_r = angle of reflected wave.

Further details to the GPR measurements can be found in section 2.3.

All used geophysical methods depend on the material properties conductivity σ , permittivity ϵ and permeability μ , which are briefly described here:

- Permittivity ϵ : When a material is exposed to an external electric field, different polarization effects, described in section 2.1, occur. The permittivity gives the ability of a material to polarize and to store energy.
- Permeability μ : The permeability indicates how magnetizable a material is.
- Conductivity σ : The electrical conductivity indicates how well the charge transport within a medium, when an external electric field is applied, works.

2 Methods

In the following it will be explained, how the different methods react to changes in the subsurface properties and how they can complement each other to obtain a better overall picture.

2.1 Electrical resistivity tomography and induced polarisation

The electrical resistivity tomography (ERT) is a direct current (DC) technique based on measurements between four electrodes, used to produce a tomography of the subsurface. For this purpose electrodes are placed into the ground and at two of them current is injected while at two others the resulting voltage is measured. The control of the current and voltage electrodes can be carried out by various methods (see figure 3):

1. **Dipole-Dipole-configuration:** The two voltage (M, N) and the two current electrodes (A, B) form a dipole at different distances from each other. Also the dipole length (distance between the two current and the two voltage electrodes, respectively) is varied, referred to as skip level, which gives the number of skipped electrodes, where a higher skip level leads to a higher achievable depth. This method represents a good compromise of high resolution and the greatest reachable depth.
2. **Wenner-configuration:** All the electrodes have the same distance to each other.
3. **Schlumberger-configuration:** The setting is similar to the Wenner-configuration, but the current electrodes have a greater distance than the potential electrodes. This configuration is therefore particularly suitable for a depth sounding.

From the known injected current (I) and the measured voltage (U), the resistance (R) can be calculated ($R = U / I$). However, the resistance determined in this way does not yet reflect the properties of the subsurface, because the geometry, i.e. the distance between the electrodes, has not yet been taken into account. This geometric factor (k) can easily be calculated (see e.g. Knödel et al., 2005):

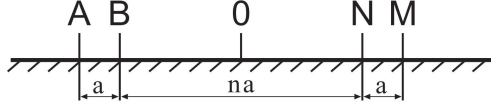
$$k = \frac{1}{2\pi} \left(\frac{1}{r_{AM}} - \frac{1}{r_{AN}} - \frac{1}{r_{BM}} + \frac{1}{r_{BN}} \right)^{-1} [m], \text{ where} \quad (10)$$

r_{AM} , r_{AN} , r_{BN} and r_{BN} are the distances between the current (A, B) and the voltage (M, N) electrodes. With this geometric factor, the apparent resistivity ρ_a can be calculated as follows:

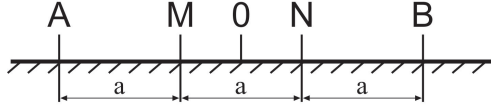
$$\rho_a = k \cdot \frac{U}{I} \quad (11)$$

In the case of a homogeneous material, the apparent resistivity (ρ_a) already equals the resistivity ($\rho = \rho_a$). However, as the subsurface is never homogeneous, the apparent resistivity gives in general no information on the subsurface materials properties. The resistivity is therefore determined by means of an inversion of the data, which tries to best fit the measured data to a model. This model will be improved in an iterative process, using finite-element techniques (for details see e.g. LaBrecque, 1996; Kemna et al., 2000; Binley & Kemna, 2005) until the data fits in the best possible way with the model. However, it should be noted that the same data can

1) Dipol-Dipol-Configuration



2) Wenner-Configuration



3) Schlumberger-Configuration

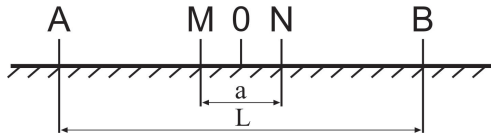


Figure 3: Schematic of the three used electrode configurations.

lead to different, equivalent models.

In order to obtain a model of the resistivity of the subsurface, measurements are taken along a profile with different distances between the electrodes. These correspond to the respective configuration to correctly resolve spatial variations in the subsurface. In this case, multi-electrode instruments allow the recording of successive measurements, where current is injected at two electrodes, but the voltage can be measured simultaneously with several pairs of electrodes. As a result, thousands of measurements can be performed effectively and in an economic way, which, combined with inversion algorithms, allow to solve the quasi-continuous distribution of the resistivity (ρ) in the subsurface. Figure 4 shows a schematic of such a multi-electrode instrument for a dipole-dipole configuration using 8 channels.

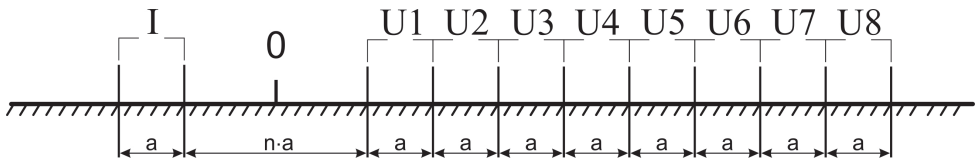


Figure 4: Schematic of a dipole-dipole configuration, where the voltage is measured simultaneously on 8 pairs of electrodes (U (1-8)).

The imaging results of ERT measurements can be given in terms of the resistivity (ρ) as described above or with respect to the conductivity (σ), with:

$$\sigma = \frac{1}{\rho} \quad (12)$$

Achievable depth and resolution of the measurements depend on the total length of the profile and the distance between the individual electrodes, as well as on the properties of the subsurface.

The latter is especially important for the dominant mechanisms of conduction, where the following three can be distinguished (e.g. Niggli, 1948):

- **Electrical conduction through grains and minerals:** This is also called electron conduction, as the charge transport takes place by electrons. The matrix conductivity depends on the minerals occurring in the subsurface, with particularly metallic minerals and semiconductors having a high matrix conductivity. All other minerals generally have a very low matrix conductivity, which, however, can vary greatly from mineral to mineral and also in the same mineral species. Another important feature of the matrix is the conductivity of certain special cases, since it is, for example, dependent on direction in crystals and generally highly temperature-dependent. For example, the matrix conductivity of many minerals and glasses increases with increasing temperature. In general, however, most rock-forming minerals are practically non-conductive at room temperature and therefore their matrix conductivity can generally be neglected in geophysical investigations.
- **Electrical conduction in the fluid:** Geophysical investigations on naturally occurring rock or sediment bodies have shown that their conductivity depends not only on the minerals that build up the electrical properties of the rocks or sediments, but often predominantly on the water present in pores and cracks. This type of electrical conduction is also called ion conduction, because here the transport of the electric charge is by ions and not by electrons. Therefore, the size of the pore spaces between the individual minerals (porosity), the water saturation and the concentration, charge and mobility of the ions are of great importance for the electrical conductivity of the entire rock body. The electrical conductivity of complete or partially saturated sediments can be calculated by Archie's law (Archie, 1942):

$$\sigma_0 = \frac{\Phi^m}{a} \sigma_f S^n \quad [S/m], \quad (13)$$

where

σ_0 : electrical conductivity of the saturated sediment

σ_f : fluid conductivity

Φ : Porosity

S : Saturation

and m, a and n are constants.

Since the liquid body must be connected in the pore spaces for a good conductivity, for example schistose rocks can create strong anisotropies, the conduction works much better parallel than normal to schist. Furthermore, there is also a temperature dependence in the ion conduction in liquids, as higher temperatures increase the mobility of the ions and thus the conductivity is also increased.

- **Electrical conduction at the grain surface:** The third type of conductivity becomes relevant as soon as minerals with charged surface, e.g. clay, which has a negatively charged surface, are present in saturated sediments. In this case, two layers (Stern electrical double layer, Stern (1924)) are formed around the charged particle. Immediately, ions of the fluid accumulate in a tightly bound layer at the surface. Further ions are loosely bound in a disordered layer. As a result, the particle appears electrically neutral, because the charge

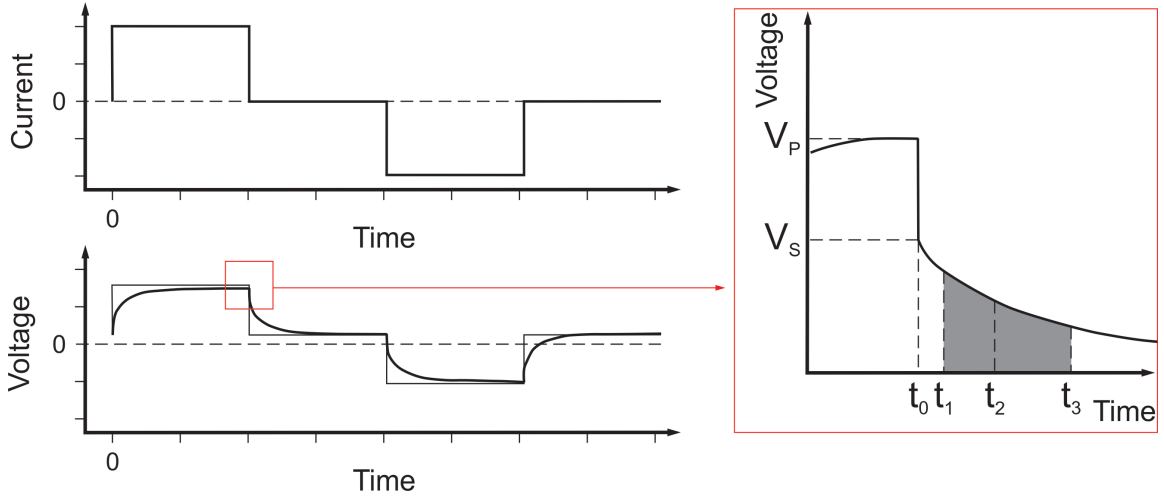


Figure 5: Schematic of a typical time domain IP. Shown are the curves of the injected current (left, upper graph) and of the measured voltage (left, lower graph). The right plot shows an enlargement of the decay curve.

of the particle is compensated by the accumulated ions of the surrounding fluid. However, if the particle is moving, e.g. by applying an electric field (DC field), parts of the loosely bound diffuse layer are sheared off and the particle no longer appears as neutral but again has a potential (zeta potential) and thus contributes to the conductivity. Archie's Law has to be extended then by the surface conductivity (σ_S) (-> conductivity = $\sigma_0 + \sigma_S$). Applying an AC field results in a frequency dependence in the conductivity due to the polarization response of electrical double layers. This effect is used in induced polarization (IP).

The IP method, an extension of the ERT method, provides information on the conductivity (σ , energy loss) and capacitive (energy storage) properties of the subsurface. IP measurements can be done in time and in frequency domain. Since all measurements on the test sites were done in time domain we will give a more detailed description here. In time domain IP a DC field is injected and then turned off. The decreasing voltage is then measured as a function of time (see figure 5, left). With such IP measurements one can determine the chargeability (m) of the soil. This is defined as:

$$m = \frac{V_S}{V_P} \quad [mV/V], \quad (14)$$

where V_P (Primary Voltage) is the voltage just before switching the current injection off, and V_S (Secondary Voltage) is the value immediately after the current injection is switched off. However, since it is not possible to measure V_S directly, an integral value for the chargeability is determined instead, whereby the voltage values are measured at discrete times:

$$m_i = \frac{1}{(t_{i+1} - t_i) V_P} \int_{t_i}^{t_{i+1}} V(t) dt \quad [mV/V] \quad (15)$$

The time of the first measurement (t_1) is always somewhat after the time of the current shut off (see figure 5, right), because one can not measure and inject at the same time. The measurement of the voltage can be carried out until the voltage values comes close the range of the noise, after

which a measurement is no longer reasonable. According to figure 5 (right), the chargeability corresponds to the Gray coloured area under the decay curve.

Similar to mechanisms of conduction, there are two possible polarization mechanisms. Electrode polarization, which occurs in conductors (e.g., metals), and thus plays no role in this study and membrane polarization. Membrane polarization occurs when the electric double layers of two minerals overlap in narrower pore space (the narrower the pore space the higher the polarization). By applying an external field, the narrow area between the two minerals acts as an ion-selective membrane. Ions that have the same charge as the mineral can pass worse than the differently charged ions. This leads to a blockage in the pore space between the minerals, which slowly resolves after switching off the external field and thus leads to the polarization effect.

In summary, one can assume that if one excludes the presence of metallic minerals, which are not expected near the surface in karst areas, the conductivity is mainly influenced by the porosity, connectivity and saturation of the pore space, by the electrical conductivity of the liquid and by surface conduction processes at the grain-water interface (e.g. Slater & Lesmes, 2002; Slater, 2006; Kemna et al., 2012). The chargeability is then caused only by the polarization of the charges in the electrical double layer, which forms at the boundary between grains and pore water (e.g. Marshall, 1959; Kemna et al., 2012). As already mentioned above, clay minerals are charged and therefore form an electrical double layer. Clay often occurs in karst areas, especially along subterranean waterways and in cavities, and could thus provide additional information in the IP images on layer boundaries, faults and preferred waterways.

2.2 Electromagnetics - CMD

In electromagnetics (EM), as in geoelectrics, the conductivity of the substrate is determined. For the measurement, however, no current is injected to the ground, but it is generated contactless by induction. In this case, a magnetic alternating field (primary field, H_P , figure 6, blue lines) is emitted by a transmitter, which induces an electric field (eddy currents, figure 6, red lines) in a conductive substrate. The time-varying electric field in turn induces a magnetic field (secondary field, H_S , figure 6, green lines). A receiver then measures the superposition of primary and secondary magnetic fields. The secondary magnetic field has a lower amplitude and a phase shift (φ) compared to the primary magnetic field (see figure 6). Since the primary magnetic field is artificially generated and thus accurately known, it can be easily removed from the measurements to obtain the secondary magnetic field.

In order to characterize the electromagnetic induction response, the induction number (b) is used, which depends on the conductivity of the subsurface (σ), the geometry, the frequency used (ω) and the magnetic permeability. Low induction numbers ($b \ll 1$) occur if there are no particularly conductive materials (such as metals) in the subsurface, then:

$$Im \frac{H_S}{H_P} \gg Re \frac{H_S}{H_P} \quad (16)$$

It follows that the apparent conductivity (σ_a) can be directly calculated from the known geometry and frequency as well as from the measured imaginary part of H_S/H_P . The achievable depth depends both on the distance between transmitter and receiver coil, as well as on the orientation

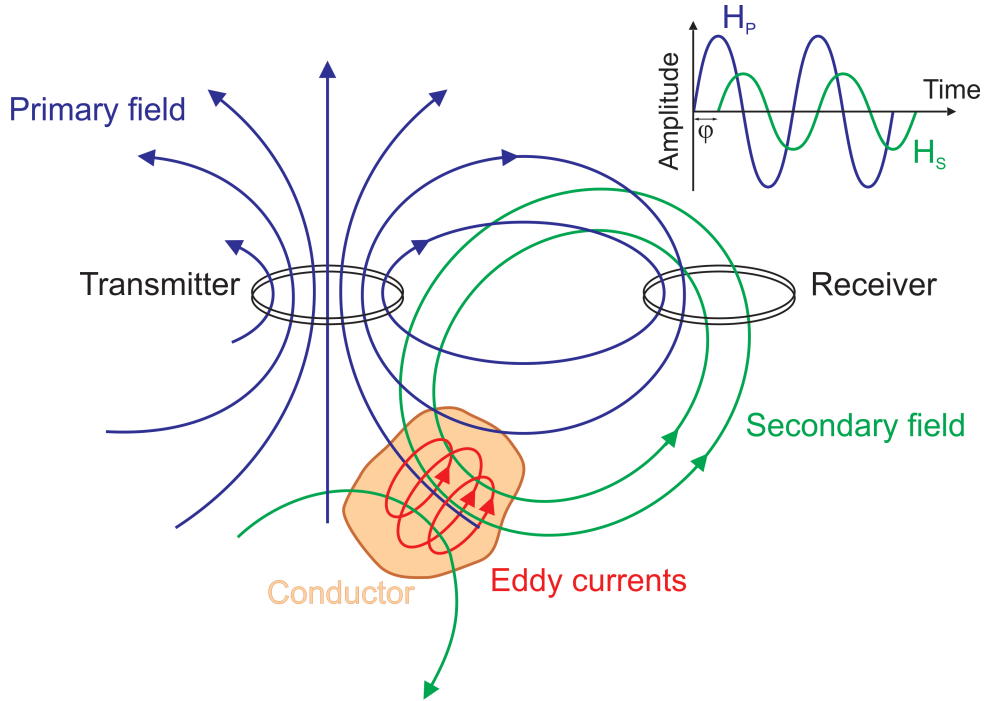


Figure 6: Principle of EM measurements. Shown are the transmitted primary magnetic field (blue), the induced eddy currents (red) and the induced secondary magnetic field (green). The small upper graph shows the received primary and secondary magnetic field. Modified after Reynolds (2011).

of the coils. Electromagnetic Conductivity Meters (CMD) were used for all measurements shown here, in which one transmitter and several receiver coils are installed and thus results can be obtained for several depths.

2.3 Ground penetrating radar

GPR is an electromagnetic pulse reflection method in which pulses are emitted by a dipole antenna and received by an antenna after reflection in the ground, where the electromagnetic waves are sent in pulse form. From the transmitter they spread with a specific velocity, are reflected at discontinuities and can reach the receiver antenna (see figure 7). The amplitudes and run times of the electrical field strength (E) are recorded. While radar waves propagate in air at near vacuum light velocity, their velocity in rock is reduced, depending on their dielectric constant (ϵ). The reflection of the pulses occurs then at boundary layers between materials with different dielectric constants. Since water has a very high dielectric constant of 81 (see table 1), it also has a major influence on the propagation of radar waves. Heavily hydrous rocks or soils become almost impermeable to radar waves. Also of great importance for GPR measurements is the electrical conductivity (σ) of the ground, as the absorption of the radar waves in the ground depends on it. Well conductive rocks therefore reduce the penetration depth very strongly. The achievable depth and spatial resolution also depend on the used pulse frequency, where lower frequencies allow greater penetration depths, but at the expense of spatial resolution. Typical GPR frequencies are in the range between 10 MHz - 1 GHz (Everett, 2013).

In this frequency range, the propagation velocity is independent of frequency and conductivity.

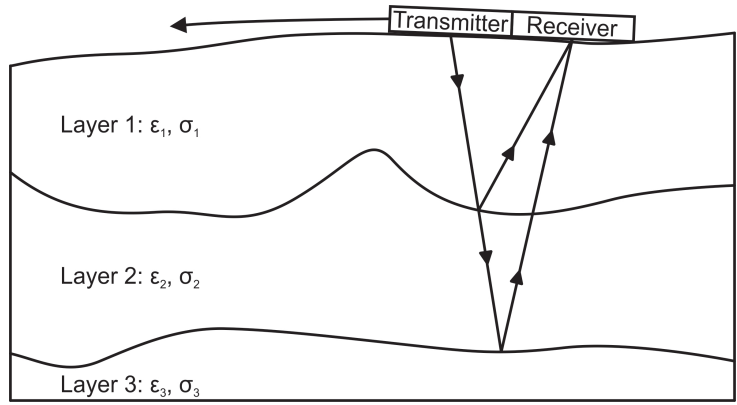


Figure 7: Schematic representation of a GPR measurement.

However, the absorption or attenuation depends on the used frequency and the conductivity of the rock. From the propagation time of the pulse, the correct depth of different boundary layers can be determined at a known propagation velocity of the electromagnetic waves (migration).

3 Numeric Models

3.1 Methods

All models shown in this section are created using the 72-electrode grid shown in figure 8. The individual quadratic elements of the grid have a size of 0.5 x 0.5 in the central area and become larger towards the edges of the grid. For the creation of the models, the 2.5D finite-element modelling code CRMod (Kemna et al., 2000) is used. For the inversion of the created models the program CRTomo (Kemna et al., 2000) was applied. Various studies have already shown that electrical images, resulting from such inversions show spatially variable image resolution (e.g. Oldenburg & Li, 1999; Friedel, 2003; Binley & Kemna, 2005), which should be taken into account when interpreting the images. Weigand et al. (2017) investigated this problem more closely and showed that the sensitivity is a good way to estimate the image resolution. In all following inversion results, this is taken into account by only drawing data points if their sensitivity is above -3.

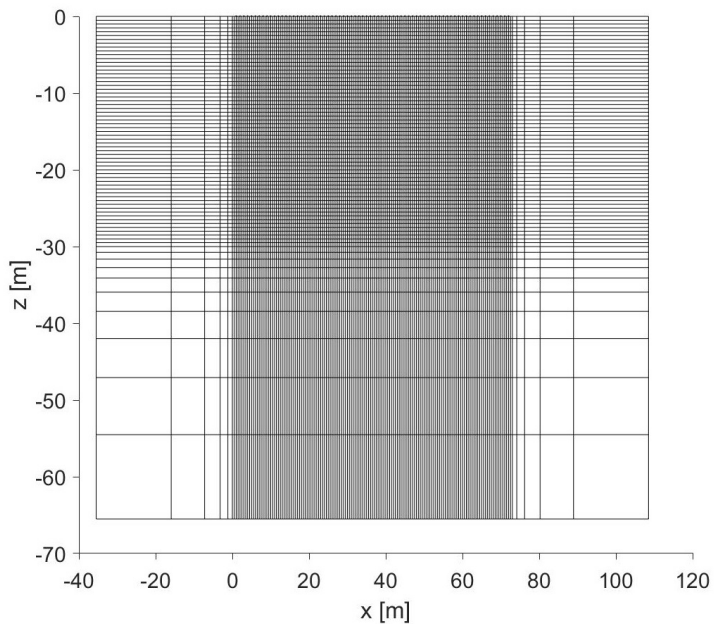


Figure 8: 72 electrode grid used for all models.

3.2 Models

In a first step, different models were tested using different electrode configurations (Wenner, Schlumberger and dipole-dipole). The aim of this study was on the one hand to determine the most favourable electrode configuration and on the other hand the resolution and depth limits. Therefore, models with a background of $100 \Omega\text{m}$ and two anomalies - one with a low resistivity of $10 \Omega\text{m}$ and one with a high resistivity of $1000 \Omega\text{m}$ - were created. For all models we used configurations with 72 electrodes, because this was also used during the field work. In a first step we investigated the three different electrode configurations to find the best solution for the present study (section 3.2.1) and in a next step we tested different distances between the electrodes to find out, which profile length is needed to reach a sufficient depth (section 3.2.2).

Table 2: Summary of all used models and the received results. The depth and the size of the two anomalies is given in column two and three, respectively. The used configuration is given in column four (DD - dipole-dipole, W - Wenner, SB - Schlumberger). The last column gives the result of the inversion: + the anomalies are clearly visible, (+) the anomalies are just visible, - the anomalies are not visible.

Model	Depth [m]	Size [m]	Configuration	Result
1-2	2	1	DD	(+)
1-2	2	1	W	(+)
1-2	2	1	SB	(+)
1-5	5	1	DD	-
1-5	5	1	W	-
1-5	5	1	SB	-
2-5	5	2	DD	(+)
2-5	5	2	W	-
2-5	5	2	SB	-
3-5	5	3	DD	+
3-5	5	3	W	(+)
3-5	5	3	SB	(+)
5-5	5	5	DD	+
5-5	5	5	W	+
5-5	5	5	SB	+
5-10	10	5	DD	(+)
5-10	10	5	W	-
5-10	10	5	SB	-

3.2.1 Configuration

In the first part of this investigation we concentrated on the selection of the best electrode configuration. Therefore we used always 72 electrodes in a distance of 1 m and varied the size and depth of the two anomalies. The used models are summarized in table 2.

In the following some results are shown to explain the procedure in more detail. For this we start with the smallest investigated anomalies with a size of 1m x 1m. These were first placed at a depth of 5 m. Figure 9 shows the result, with the first graph showing the underlying model, the second the resistivity and the third the sensitivity. In the resistivity image all data points with a sensitivity below -3 are not shown, because no meaningful results can be expected here (details in section 3.1). As an example, the result of the dipole-dipole configuration is shown, but also Wenner and Schlumberger configurations lead to similar results. The results showed clearly that 1m x 1m size anomalies are not visible in the inversion results, thus we tried some more models with anomalies closer to the surface. Figure 10 shows the results for two anomalies in a depth of 2 m. In the upper row of figure 10 the two anomalies are hardly visible, but one can suspect already that there might be anomalies in the subsurface. The lower row shows the inversion result, when adapting the scale of the resistivity to the data range. Now the two anomalies are clearly visible. This scenario - hardly visible in the model scale, but clearly visible for adapted scale - was defined as detection limit. Thus we can conclude that 1m x 1m sized anomalies could possibly be seen in a depth of about 2 m, but not below.

The next step was to find the size of the anomalies needed to be seen in 5 m depth. Therefore we

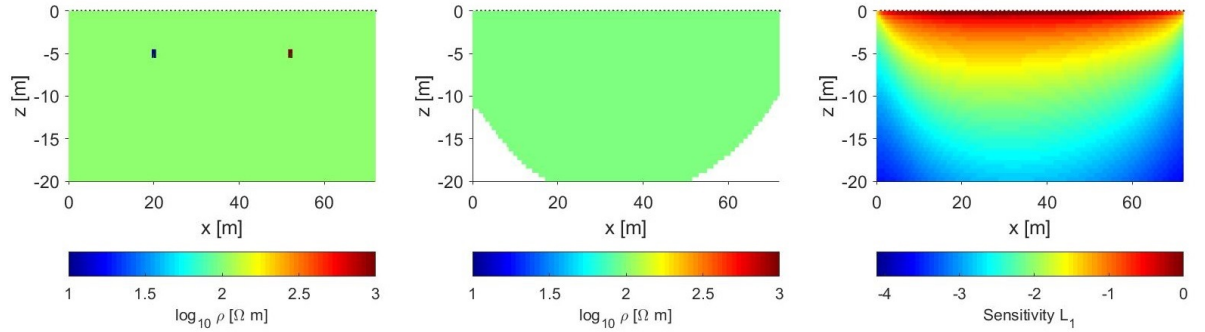


Figure 9: Model with two anomalies (one with a high and one with a low resistivity) each of 1m x 1m size placed in a depth of 5 m. The forward modelling was done with a dipole-dipole-configuration. The left graph shows the model, the middle graph the resistivity and the right graph the sensitivity after inversion. Note that the x/z axes are not on the same scale.

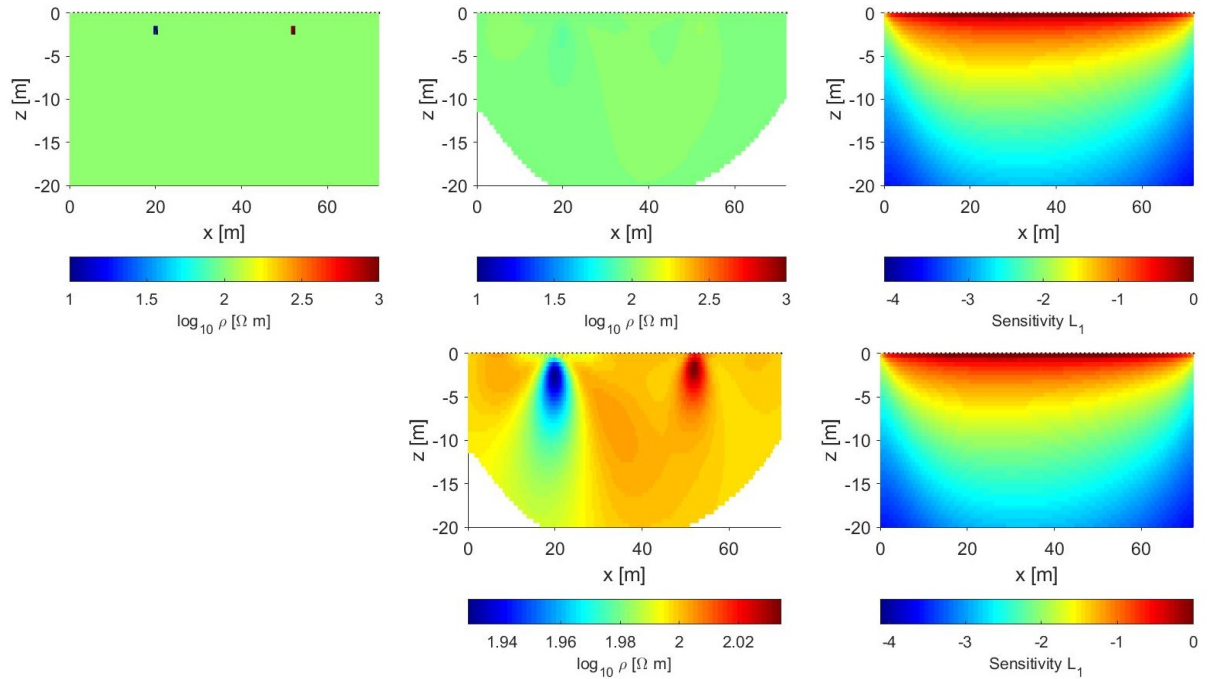


Figure 10: Like figure 9, but for a depth of the anomalies of 2 m. Upper row: equal scale for model and resistivity, Lower row: adapted scale for the resistivity.

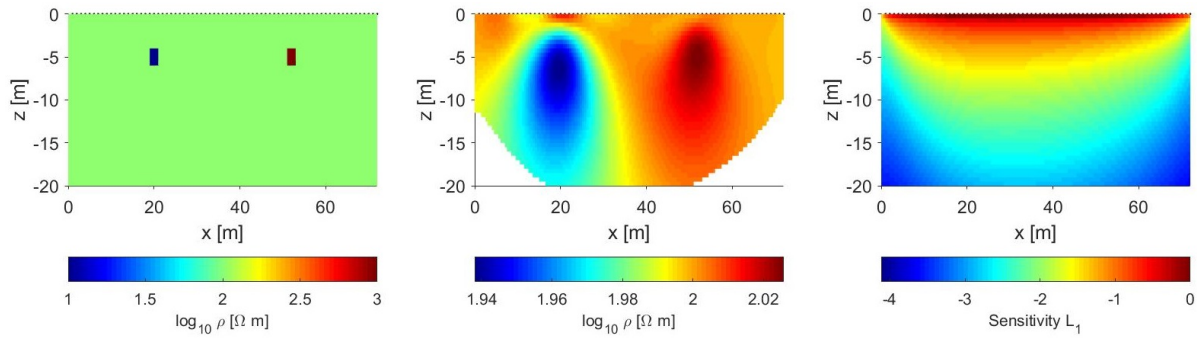


Figure 11: Like figure 9, but for a depth of the anomalies of 5 m and a size of 2m x 2m again with an adapted scale for the resistivity.

increase the size of the anomalies in 1 m steps. It turned out that for the dipol-dipol configuration the anomalies are already visible for a size of 2m x 2m (see figure 11). For the Wenner and the Schlumberger configuration the anomalies with 2m x 2m size were not visible. Thus, we increased the size again to 3m x 3m. From this size on all configurations were able to reproduce the two anomalies. For an anomaly size of 5m x 5m all three configurations show a clear result without needing an adaption of the colour scale. Therefore, figure 12 shows these results to compare the three configurations, all of them reproduce the two anomalies well. Nevertheless, the dipole-dipole configuration leads to the clearest result. In a last step we tested, if the two anomalies with 5m x 5m could also be seen in an depth of 10 m. Here it turned out that only the dipole-dipole configuration was able to just reproduce the two anomalies. From all the results shown so far it can already be concluded that the dipole-dipole configuration is the best choice for the present problem, because it achieves a better resolution and a greater depth than the other two configurations. Therefore, the dipole-dipole configuration was already chosen at this point and all further tests were only carried out for the dipole-dipole configuration.

3.2.2 Detection limits

The next step was to find the maximal reachable depth in dependence of the anomaly size, wherein the depth was decreased in 5 m steps. This results in a maximum size of the anomalies of 10m x 10m, otherwise one would come into the range of the next depth step. This study was carried out up to a depth of 20 m, as the caves in the test areas reach this maximum depth. For the region closer to the surface (down to 15 m) the results from chapter 3.2.1 were used extended by models with anomalies in a depth of 15 m. For the deeper areas, some more models were calculated using a distance of 2 m between the electrodes, because from the sensitivity plots in figures 9-12 (last column) one can already conclude that the depth limit for 1 m distance between the electrodes will be between 15 m and 20 m. In fact, the model calculations have also shown that anomalies in 20 m depth can no longer be determined with the 1 m electrode spacing configuration. The model calculations with 2 m electrode spacing showed, that here anomalies in a depth of 20 m would also be detectable. The found depth and size limits are summarized in figure 13. In the plot, one can clearly see a linear relationship between the depth and the size of the anomalies necessary for a detection, which is apparently independent of the used electrode

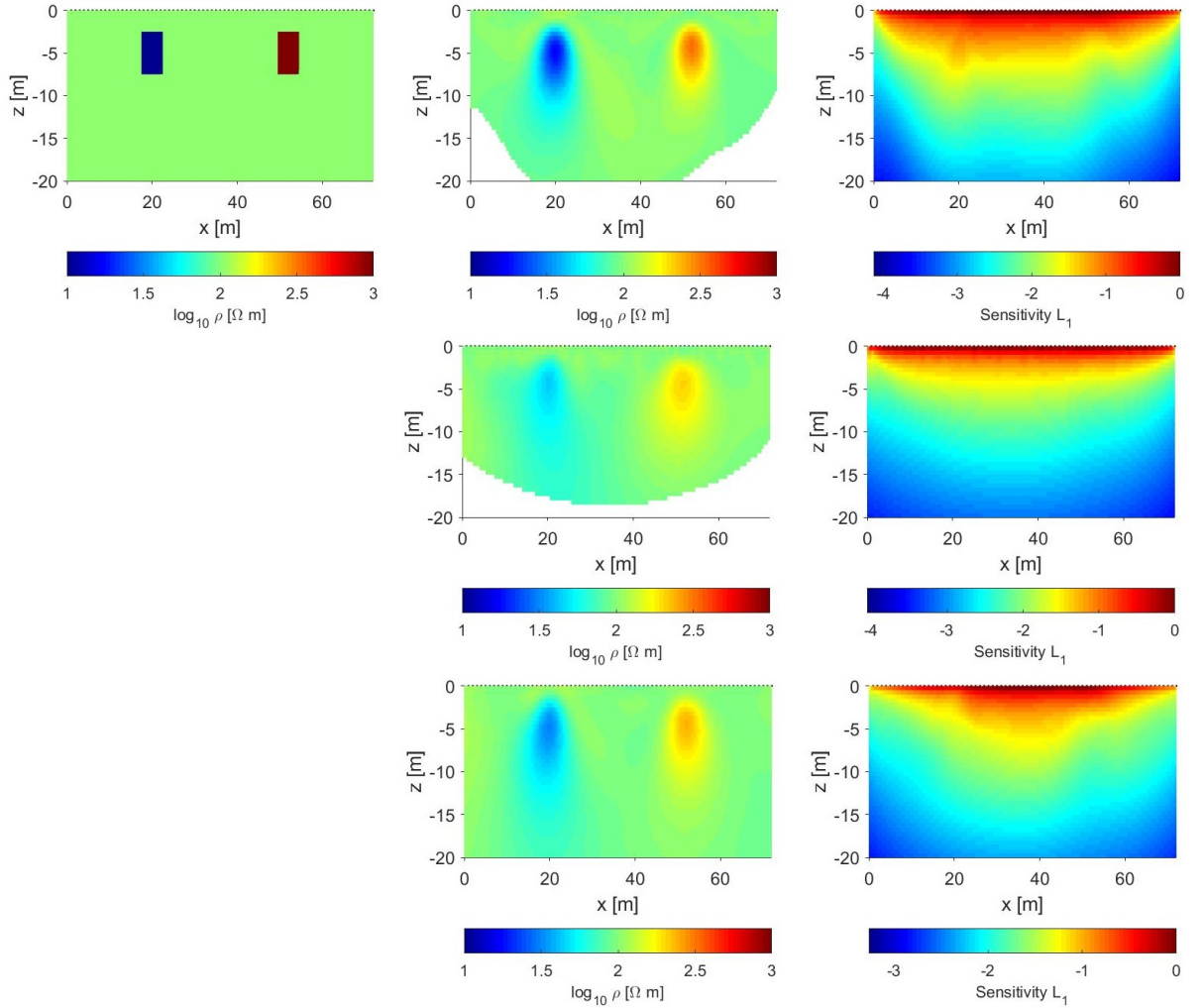


Figure 12: Like figure 9, but for an anomalies size of 5m x 5m. Upper row: dipole-dipole configuration, middle row: Wenner configuration, lower row: Schlumberger configuration.

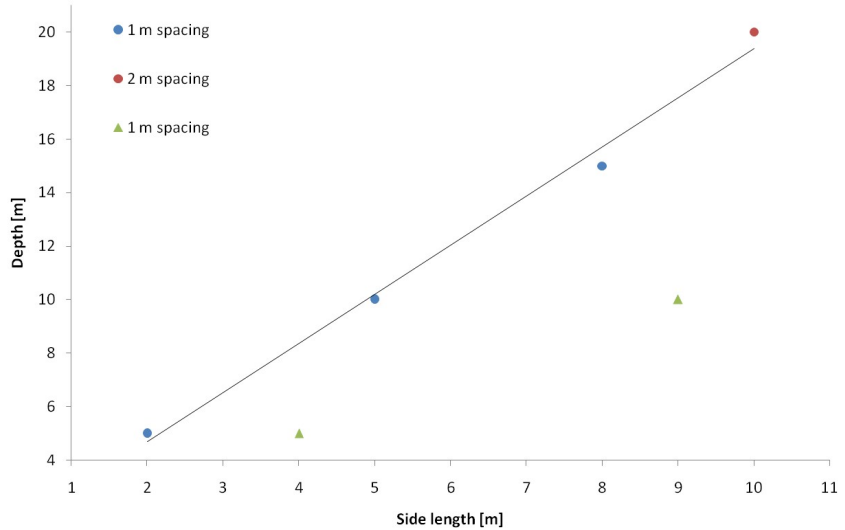


Figure 13: The graph shows the found correlation between the anomalies depth and it's size. Blue dots give the results for an electrode spacing of 1 m and red dots of 2 m. The black line shows a linear fit through all data.

spacing. The parameters of the linear fit are:

$$\text{depth} = 1.836 \cdot \text{side length} + 1.020 \quad (17)$$

The investigations have shown that some deeper anomalies must reach a considerable size to be detected. We note that in all previous models, the effect of measurement errors, which occur in real measurements, were neglected. The previously calculated error-free models therefore always converged very well with values of the RMS (Root Mean Square) between 0.99 and 1.04. In order to check the validity of the sizes to depth dependence also for noisy data, the 4 models used for figure 13 were again inverted with a data error of 5%. Already the inversion of the first model showed that models with noisy data require even larger anomalies in order to be detectable. Figure 13 shows the results for the two models with near-surface anomalies (green triangles). Again, the RMS values were close to one after the last iteration. Already at a depth of 15 m, the anomalies would need side lengths of more than 10 m to be detectable. The cavities in the study area, however, have dimensions of several meters only with a few exceptions. Hence the two deeper models were not inverted. However, the previous tests have been carried out only with fictitious anomalies, which do not reflect the true nature of cavities in rock. Therefore, a more realistic model of cavities in rock, specifically regarding the expected resistivity, has been created and investigated. As background limestone with a mean resistivity of 1000 Ωm and for the two anomalies one filled with clay with a resistivity of 10 Ωm and one filled with air with a resistivity of $10^9 \Omega\text{m}$ was chosen.

Again, these models have been inverted for the four depths to size ratios shown in figure 13, again assuming a data error of 5%. For these models, however, the ratio of depth to size of the anomalies was consistent with those of the error-free models (figure 13, blue and red points). Therefore it can be concluded that this much larger contrast in resistivity has a positive effect on the detectability of cavities (air, or water/clay filled) and thus it can be assumed that at least the close to surface areas of the cave in the study area will be detectable. In the following section we checked in a last test, if the geometry of a more complex cave would be resolvable and if 1 m or 2 m spacing between the electrode would be the better choice.

3.2.3 Proof of concept

The results from chapter 3.2.2 could not clearly determine whether 1 m or 2 m spacing between the electrodes is required to resolved the cavity well. Additionally up to now only square anomalies were used, hence a more realistic cave model was created including a 1.5 m deep soil layer with 100 Ωm , a limestone background with 1000 Ωm and a more complex cave with a resistivity of $10^9 \Omega\text{m}$. The forward modelling was performed once with 1 m and once with 2 m electrode spacing and by neglecting or considering a 5% data error. The images resulting after inversion are shown for 1 m spacing in figure 14 and for 2 m spacing in figure 15.

All inversion results show the soil layer, the limestone and an anomaly in the area of the cave, where in all cases the geometry of the cave is no longer recognizable. This result also agrees very well with the results of later actual measurements above known cave parts. Although the position of the cave could always be determined quite accurately, its geometry was not determined (see section 5.2). This is probably due to the inclusion of a soil layer and data errors. Earlier tests

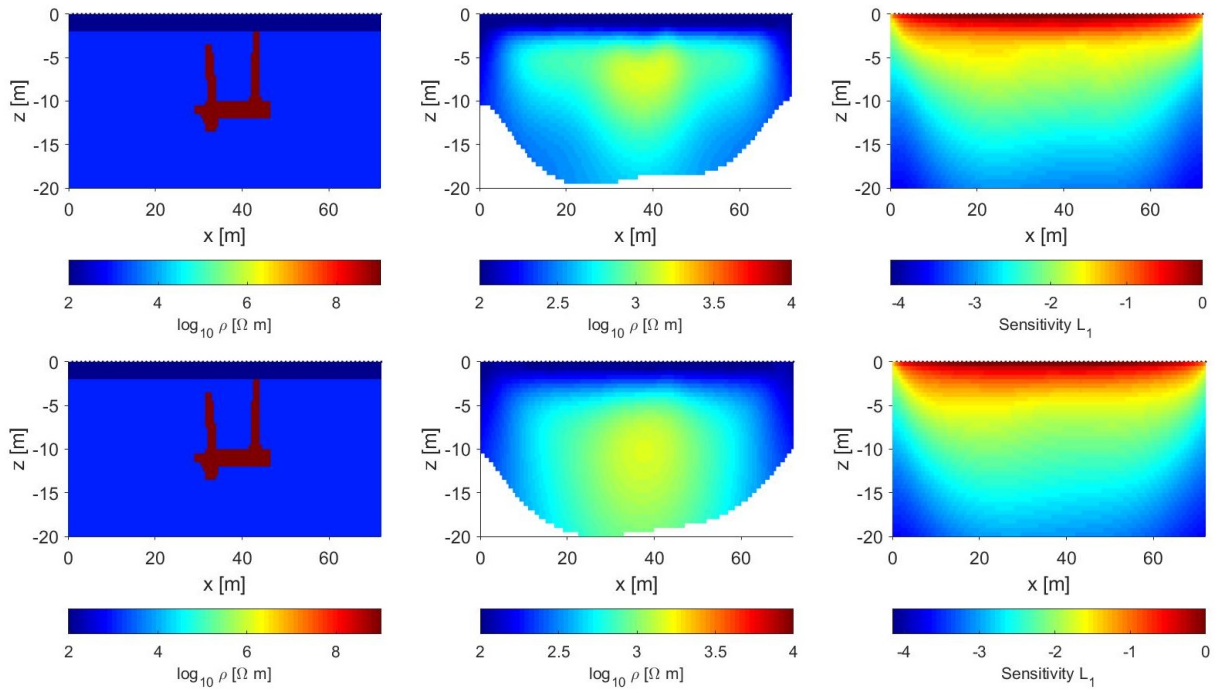


Figure 14: Results for a more realistic cave model using a configuration with 1 m distance between the electrodes. In the first column the models are plotted. The second and the third column gives the inversion results (resistivity and sensitivity). Upper row: without data error, lower row: with data error.

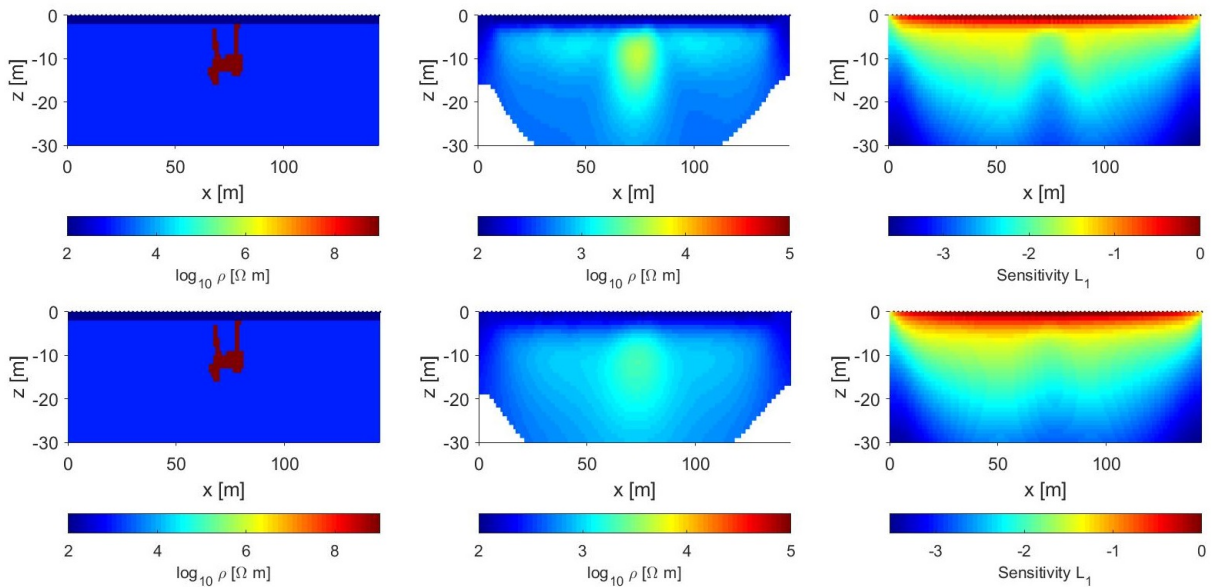


Figure 15: Like figure 14 but using a configuration with 2 m distance between the electrodes.

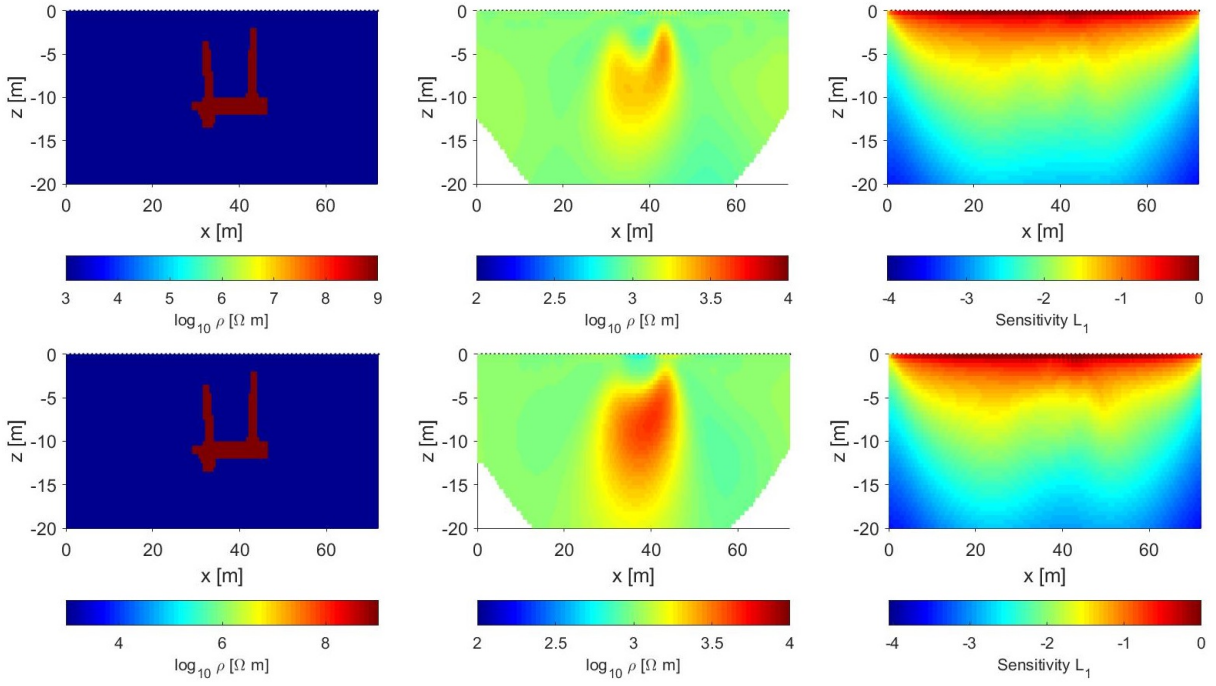


Figure 16: Like figure 14 but without soil layer. First row without and second row with data errors.

without soil layer and data errors have shown a better resolution here (figure 16, first row). In figure 16 (second row) the result for a model without soil layer, but with data errors is shown. Although the resolution is somewhat better here than in the model with soil layer and data errors (figure 14), it is already much worse than in the model without soil layer and data errors (figure 16, first row). Thus, one can conclude that both the presence of a soil layer as well as data errors, which always exist if dealing with measurements, lead to a degradation of the resolution, which makes it impossible to detect the detailed geometry of underground cavities. In all inversion results, it is also noticeable that the resistivity values after inversion are significantly lower than those of the models. This was not the case for the clearly identifiable anomalies of the theoretical models in section 3.2.1 (see figure 12). Therefore one can assume that this may also be due to the poorer resolution of the complicated geometry of the realistic cave models, nevertheless the results showed that a distance between the electrodes of 1 m is sufficient to reach the needed depth of about 15 m. Since the position of the cave is reproduced here more precisely, an electrode distance of 1 m was chosen for the measurements above the two investigated caves.

4 Case studies

In this work, ERT, EM and GPR measurements were carried out in two nearby areas. Details on the measuring sites, tasks and objectives as well as on the results are summarized in the following article "Detection of two caves near Lunz am See (Lower Austria) using geophysical methods". More details about all performed and available measurements as well as results not shown in the paper are summarized in the following. More detailed information on the used methods can be found in section 2.

4.1 Die Höhle: Anwendung geophysikalischer Methoden zur Detektion zweier Höhlen nahe Lunz am See (NÖ)

Anwendung geophysikalischer Methoden

zur Detektion zweier Höhlen nahe

Lunz am See (NÖ)

ZUSAMMENFASSUNG

Die bildgebenden geophysikalischen Methoden Geoelektrik (Electrical Resistivity Tomography, ERT) und Georadar (Ground Penetrating Radar, GPR) wurden verwendet, um oberflächennahe Hohlräume zu detektieren. Das Untersuchungsgebiet liegt südwestlich von Lunz am See in den Nördlichen Kalkvoralpen und umfasst zwei Höhlen, den Forststraßeneinbruch und die Stiegengraben-Wasserhöhle. Der Forststraßeneinbruch (1823/64) wurde im Dezember 2016 aufgrund eines in einer Forststraße eingebrochenen Lochs gemeldet. Ziel dieser geophysikalischen Untersuchung war es, die Lage weiterer oberflächennaher Hohlräume zu bestimmen, um einsturzgefährdete Stellen zu erkennen. Die auf eine Länge von 1 km vermessene Stiegengraben-Wasserhöhle (1823/25) wurde in den 1970er Jahren beim Bau einer Forststraße mit großen Blöcken und später mit großen Mengen an feinkörnigem Material zugeschüttet. Hier besteht die Befürchtung, dass der Wasserdruck durch das Verstopfen der episodisch aktiven Quellhöhle das unverfestigte Material mobilisiert, was zu einer Mure führen und die Häuser im Tal darunter gefährden könnte. Ziel der geophysikalischen Untersuchung war hier, die exakte Lage des ehemaligen Höhleneingangs zu identifizieren, um eine Öffnung mittels Bagger zu ermöglichen.

Die Ergebnisse zeigen, dass sich sowohl ERT als auch GPR Messungen gut eignen, um oberflächennahe Hohlräume bis in eine Tiefe von etwa 10 m in Kalkstein zu detektieren. Bei Hohlräumen in etwas größeren Tiefen (10 bis 30 m), wie dies beim Forststraßeneinbruch der Fall ist, zeigen vor allem die ERT-Bilder deutliche Kontraste in den physikalischen Eigenschaften des Untergrunds, welche mit der Lage der bekannten Höhle sehr gut übereinstimmen. Weitere oberflä-

chennahe Hohlräume konnten im Bereich des Forststraßeneinbruchs nicht gefunden werden. Mit Hilfe der geophysikalischen Messungen konnte der verschüttete Eingang oberhalb der Stiegengraben-Wasserhöhle lokalisiert werden. Unsere Studie zeigt, dass eine Kombination von ERT und GPR im Vergleich zu den Einzelauswertungen eine verbesserte Interpretation der geophysikalischen Modelle zur Abgrenzung von Karsthohlräumen erlaubt.

ABSTRACT

Detection of two caves near Lunz am See (Lower Austria) using geophysical methods

Geophysical imaging using electrical resistivity tomography (ERT) and ground penetrating radar (GPR) was conducted in order to detect near-surface cavities. The study area is located southwest of Lunz am See in the Northern Calcareous pre-Alps and comprises two caves, Forststraßeneinbruch and Stiegengraben-Wasserhöhle. The former was reported because a hole had opened in a forest road in December 2016. The aim of the geophysical investigation was to delineate the possible location of further near-surface caves that could potentially collapse. Stiegengraben-Wasserhöhle is a 1 km-long cave which was filled with gravel during the construction of a forest road in the 1970s and more recently with lots of fine-grained sediment. It is possible that the water pressure inside the cave could rise due to the plugging of the episodic spring mobilising the unconsolidated material, which could result in a debris flow, endangering houses in the valley below. The aim of the geophysical investigation was to exactly locate the cave entrance in order to reopen it using an excavator.

Barbara Funk

barbara.funk@tuwien.ac.at

Adrian Flores-Orozco

flores@tuwien.ac.at

Theresa Maierhofer

theresa.maierhofer@tuwien.ac.at

Forschungsgruppe Geophysik,
Department für Geodäsie und
Geoinformation, TU-Wien,
Karlsplatz 13, 1040 Wien

Lukas Plan

Karst- und Höhlen-Arbeitsgruppe,
Naturhistorisches Museum,
Museumsplatz 1/10, 1070 Wien,
lukas.plan@nhm-wien.ac.at

Eingelangt: 27.3.2018

Angenommen: 15.6.2018

The results show that both ERT and GPR measurements are well suited for detecting near-surface cavities (depth < 10 m) in limestone. For cavities at a slightly greater depth (10 to 30 m), such as Forststraßeneinbruch, the ERT images show clear contrasts in the physical properties of the subsurface, which agree very well with the location of the known cave. Further near-surface cavities could not be found in

the area of Forststraßeneinbruch. The buried entrance above Stiegengraben-Wasserhöhle could be successfully located using the geophysical measurements.

Our study demonstrates that the combined application of ERT and GPR permits an improved interpretation of geo-physical models for the delineation of caves in karstic environments.

EINLEITUNG UND UNTERSUCHUNGSGEBIET

Das Untersuchungsgebiet, der Schöfttaler Wald 5 km südwestlich von Lunz am See, zeichnet sich durch eine große Höhlendichte aus, wobei die 1 km lange Stiegengraben-Wasserhöhle die ausgedehnteste ist (Abb. 1). Die meisten Höhlen und Karsterscheinungen wie Dolinen und Schwinden sind im Opponitzer Kalk entwickelt. Weiters dominiert Hauptdolomit, der aber deutlich weniger Höhlen aufweist (Abrahamczik, 1935; Bauer et al., 1988). Die Abgrenzung der Geometrie oberflächennaher Hohlräume ist sowohl für den Straßenbau als auch für sonstige Baumaßnahmen von

Bedeutung. Die beiden hier vorgestellten Fallbeispiele wurden ausgesucht, um das Potenzial geophysikalischer Methoden zur Abgrenzung von Gefahren, welche von Höhlsystemen im Karst ausgehen können, zu zeigen.

Im Dezember 2016 brach nahe einer Forststraßenkreuzung zwischen Stiegengraben und Großschöpfthal ein rund 1 m messendes Loch ein.

Die darunterliegende Höhle (Forststraßeneinbruch, 1823/64) wurde bis Juli 2018 auf 147 m Länge und 24 m Tiefe vermessen (unpublizierter Bericht im Kataster

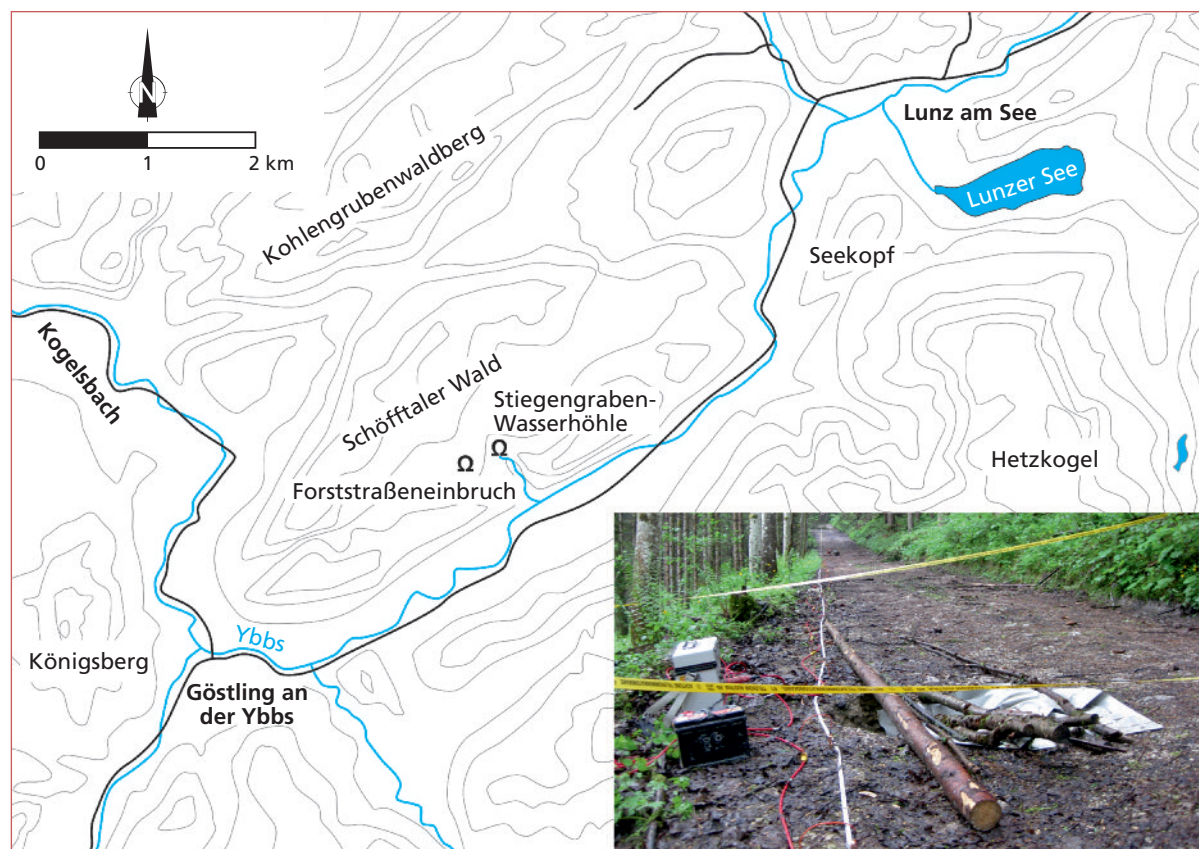


Abb. 1: Lage des Forststraßeneinbruchs und der Stiegengraben-Wasserhöhle zwischen Lunz am See und Göstling an der Ybbs. Das Foto zeigt den behelfsmäßig abgedeckten Eingang des Forststraßeneinbruchs sowie die geoelektrische Ausrüstung.
Fig. 1: Location of Forststraßeneinbruch and Stiegengraben-Wasserhöhle between Lunz am See and Göstling an der Ybbs. The photo shows the provisionally covered entrance of Forststraßeneinbruch as well as the ERT instrument.

des Landesvereins für Höhlenkunde in Wien und NÖ). Der eingebrochene Einstiegsschacht bildete sich im unverfestigten Schutt und Bodenmaterial. In knapp



Abb. 2: Unbefahrbar enger Canyon oberhalb vom tiefsten Punkt des Forststraßeneinbruchs.

Fig. 2: Impassable canyon near the deepest point of Forststraßeneinbruch.

Foto: Lukas Plan

2 m Tiefe trifft man auf einen engräumigen Canyon im anstehenden Opponitzer Kalk. Die Höhle ist meist engräumig und besteht aus phreatisch entstandenen Röhren sowie vadosen Canyons und Schächten. Weitverbreitete klebrige Feinsedimentlagen gestalten die Befahrung und Vermessung anspruchsvoll. Die Höhle verläuft weitgehend parallel zum Stiegengraben und damit an der Grenze zwischen Opponitzer Kalk und Hauptdolomit, wobei die Höhle selbst im Kalk ausgebildet ist. Ein unbefahrbar enger, aber stark bewetterter Canyon im Endbereich steht mit großer Wahrscheinlichkeit mit der Stiegengraben-Wasserhöhle (1823/25) in Verbindung (Abb. 2).

Die episodisch wasseraktive Stiegengraben-Wasserhöhle wurde 1935 von Walter Abrahamczik entdeckt und von 1967 bis 1972 auf 1002 m Länge bei +30 m Höhenunterschied dokumentiert (Süssenbeck, 1974; Hartmann & Hartmann, 1985). Anschließend wurde beim Forststraßenbau ihr Eingang mit großen Blöcken verschüttet. Trotz Außenvermessung im Jahr 1972 ist die exakte Position des Eingangs nicht mehr rekonstruierbar. Im Jahr 2016 wurden zusätzlich große Mengen feinkörnigen Aushubmaterials aus einem Retentionsbecken oberhalb des Stiegengrabens über den zugeschütteten Eingangsbereich deponiert. Da bei Starkregen nun die Gefahr besteht, dass das Wasser in der Höhle rückgestaut und das lose Material weggespült wird und die unterhalb des Stiegengrabens liegenden Häuser gefährdet, sollte der Eingang wieder aufgegraben und durch ein Betonrohr der Wasserabfluss ermöglicht werden.

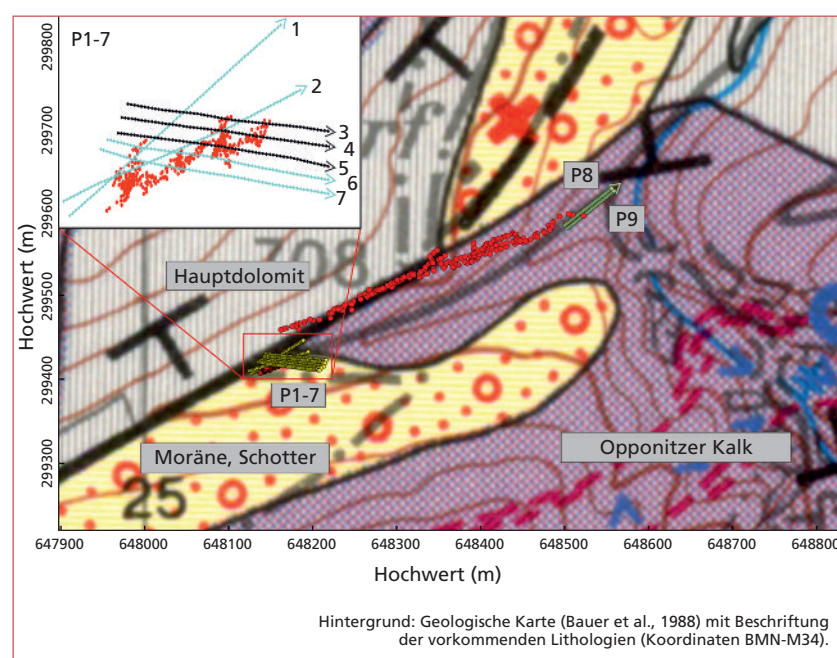


Abb. 3: Verlauf von Stiegengraben-Wasserhöhle und Forststraßeneinbruch (Polygonzugspunkte in Rot). In Gelb sind die geophysikalischen Profile (P1-P7) oberhalb des Forststraßeneinbruchs und in Grün die Profile oberhalb der Stiegengraben-Wasserhöhle (P8 und P9) gezeigt. Das Insert zeigt eine Vergrößerung des Forststraßeneinbruchs mit den sieben gemessenen Profilen (Geoelektrik-Profil in schwarz, GPR-Profil blau).
Fig. 3: Position of Stiegengraben-Wasserhöhle and Forststraßeneinbruch (red dots indicate survey points). The geophysical profiles above Forststraßeneinbruch (P1-P7) and above Stiegengraben-Wasserhöhle (P8 and P9) are shown in yellow and green, respectively. The insert provides a zoom of Forststraßeneinbruch showing the seven measured profiles (ERT profiles black, GPR profiles blue).

Die Geometrie beider Höhlen ist durch existierende Pläne und Vermessungsdaten (Polygonzug durch die Höhle) bekannt. Während beim gut verorteten und mit DistoX und PDA vermessenen Forststrasseneinbruch die Lagegenauigkeit unter 1 m liegt, besteht bei der Stiegengraben-Wasserhöhle das Problem, dass der Eingang nur auf rund 8 m genau bekannt ist. Hier ist weiters aufgrund der über 40 Jahre alten Vermessung mit Suunto und Maßband mit einer Ungenauigkeit des Polygonzugs im Endabschnitt von weiteren rund 10 m zu rechnen. Beide Höhlen verlaufen an der Grenze des Opponitzer Kalks zum Hauptdolomit (Abb. 3).

Geophysikalische Methoden bieten die Möglichkeit, zerstörungsfrei Informationen über den Untergrund zu gewinnen. Gute Erfahrungen bezüglich des Aufspürens von unterirdischen Hohlräumen gibt es speziell mit Geoelektrik und Georadar, welche besonders Änderungen der elektrischen Eigenschaften (Dielektrizität ϵ und elektrische Leitfähigkeit $\sigma = 1/\rho$) im Untergrund anzeigen. Da Luft ein elektrischer Isolator ist (hoher spezifischer elektrischer Widerstand $\rho > 10 \text{ k}\Omega\text{m}$), können lufterfüllte Hohlräume durch ihren Widerstandskontrast zum umliegenden Gestein erkannt werden. Hohlräume, die mit Wasser oder Sediment gefüllt sind (beides zeichnet sich durch gute elektrische Leitfähigkeit aus), zeigen wiederum einen sehr niedrigen Wert des spezifischen elektrischen Widerstands ($< 0,1 \text{ k}\Omega\text{m}$). Der erreichbare Kontrast ergibt sich dabei im Vergleich zum spezifischen elektrischen Widerstand des umgebenden Gesteins, welcher im Fall von Kalkstein einen großen Bereich von etwa 0,5 bis 5 $\text{k}\Omega\text{m}$ umfasst.

Beide Methoden wurden bereits erfolgreich zur Untersuchung von Hohlräumen im Karst verwendet. So

berichten Chamberlain et al. (2000) über eine erfolgreiche Detektion unbekannter Hohlräume in einer Tiefe zwischen 13 und 19 m nahe der Kitley Caves in Devon (England) mit Hilfe des Georadars und einer 100-MHz-Antenne. Von Behm et al. (2005) wurden die Güntherhöhle sowie weitere unbekannte Hohlräume mit Hilfe des Georadars und einer 40-MHz-Radar Antenne aufgefunden und visualisiert. Die Güntherhöhle weist dabei unterhalb des Profils eine Ausdehnung von etwa 2 x 10 m (B x H) auf und liegt in einer Tiefe zwischen ca. 15 und 25 m. Frid et al. (2015) nutzten Geoelektrikmessungen, um in Amazia (60 km südöstlich von Tel Aviv, Israel) großflächig eine große Anzahl künstlich gegrabener Hohlräume zu lokalisieren, da es hier immer wieder Probleme beim Siedlungsbau gab. Dreißig solcher Hohlräume wurden verortet und durch Bohrungen bestätigt. Redhaounia et al. (2016) führten ebenfalls großflächige Geoelektrikmessungen durch, um eine Karstfläche im Nordwesten von Tunesien zu charakterisieren. Auch hier konnten in den Ergebnissen mehrere Hohlräume erkannt werden. Kaufmann et al. (2015, 2017) nutzten gravimetrische, geoelektrische und Georadarmessungen oberhalb von zwei Höhlen im Südharz in Deutschland. Während die Gravimetrie und die Geoelektrik bei beiden Höhlen (Jettenhöhle im Gips/Anhydrit, Einhornhöhle im Dolomit) die bekannten Hohlräume identifizierten, erwies sich das Georadar im Dolomit als zielführend, im stark zerklüfteten Gips aber durch Querreflexionen nur eingeschränkt nutzbar. Alle drei Methoden deuteten an der Einhornhöhle auf weitere, unbekannte Fortsetzungen hin, die inzwischen auch erbohrt wurden.

METHODEN

Bei den Geoelektrikmessungen wurde die sogenannte *Electrical Resistivity Tomography (ERT)* angewandt; dabei handelt es sich um ein Gleichstromverfahren, welches auf Messungen zwischen jeweils vier Elektroden basiert. Dabei werden Metallstäbe (Elektroden) in den Boden eingeschlagen und bei jeweils zwei davon Strom (I) eingeleitet und bei zwei anderen die resultierende Spannung (U) gemessen. Multielektrodeninstrumente erlauben die Aufzeichnung aufeinanderfolgender Messungen, wobei auch hier bei jeweils zwei Elektroden Strom eingespeist wird, die Spannung aber gleichzeitig bei mehreren Elektrodenpaaren gemessen wird. Dadurch können effektiv und zeitsparend tausende Messungen durchgeführt werden, die es in Kombination mit Inversionsalgorithmen ermöglichen, die quasi-kontinuierliche Verteilung des

spezifischen elektrischen Widerstands im Untergrund darzustellen. Für die hier vorgestellten Messungen wurde ein Syscal-Gerät (Syscal Pro Switch 72, IRIS-Instrumente) mit zehn Kanälen verwendet, welches bis zu zehn Spannungswerte gleichzeitig für jede Strom-einspeisung erfassen kann. Die räumliche Auflösung hängt dabei vom Abstand zwischen den einzelnen Elektroden und die erreichbare Tiefe von der Gesamt-länge des Profils ab. Für die hier vorgestellten Messun-gen stand ein System mit 72 Elektroden zur Verfügung. Da hier vor allem oberflächennahe Hohlräume mit ei-ner hohen räumlichen Auflösung untersucht werden sollten, wurden alle Daten mit einem Elektrodenab-stand von 1 m aufgenommen, was zu einer Auflösung von etwa 0,25 m (vertikal und horizontal) und zu einer Untersuchungstiefe von ca. 15 m führt. Die Ansteue-

rung der Strom- und Spannungselektroden wurde dabei nach der Dipol-Dipol Methode durchgeführt, wobei hier acht der verfügbaren zehn Kanäle für die Spannungsmessung verwendet wurden. Um ein Modell des spezifischen elektrischen Widerstands des Untergrunds zu erhalten, werden entlang eines Profils (hier mit 72 Elektroden) für insgesamt 2068 Quadrupole mit unterschiedlichen Dipollängen ($a = 1, 2, 3, \dots, 12$ m) und Abständen zwischen Strom- und Spannungsdipolen ($n = 1, 2, 3, \dots, 50$ m) Messungen durchgeführt, um räumliche Variationen im Untergrund auflösen zu können. Die Abbildungsergebnisse von ERT-Messungen können dabei in Bezug auf den spezifischen elektrischen Widerstand (ρ , wie in der vorliegenden Studie) oder in Bezug auf die elektrische Leitfähigkeit (σ , mit $\sigma = 1/\rho$) angegeben werden.

Beim Georadar handelt es sich um ein elektromagnetisches Impulsreflexionsverfahren, bei dem Impulse von einer Dipol-Antenne ausgestrahlt und nach der Reflexion im Untergrund von einer Antenne empfangen werden. Die Reflexion der Impulse tritt dabei an Grenzschichten zwischen Materialien mit verschiedenen Dielektrizitätskonstanten auf, wobei die Amplitude der reflektierten Signale zusätzlich von der elektrischen Leitfähigkeit abhängt. Aus der Laufzeit des Impulses kann man bei bekannter Ausbreitungsgeschwindigkeit der elektromagnetischen Wellen die korrekte Tiefe verschiedener Grenzschichten bestimmen (Migration). Erreichbare Tiefe und räumliches Auflösungsvermögen hängen dabei ebenfalls von den elektrischen Eigenschaften des Untergrunds, sowie von der verwendeten Impuls-Frequenz ab. In der vorliegenden Studie wurden eine 80-MHz-Antenne (Wellenlänge 1,5 m, Medium Kalk) und eine 400-MHz-Antenne (Wellenlänge 0,3 m, Medium Kalk) verwendet. Daraus resultiert eine vertikale Auflösung ($\approx 1/4$ der

Wellenlänge) von etwa 0,375 m bzw. 0,075 m. Die horizontale Auflösung nimmt mit zunehmender Entfernung zur Antenne ab und ist durch die erste Fresnel Zone definiert. Mit der 80-MHz-Antenne erreicht man damit eine horizontale Auflösung von etwa 1,9 m in einer Tiefe von 5 m, aber nur noch von 4,7 m in einer Tiefe von 30 m. Mit der 400-MHz-Antenne erreicht man in einer Tiefe von 5 m eine horizontale Auflösung von ca. 0,9 m. Für die Untersuchung des Forststraßen-einbruchs wurde eine 80-MHz-Antenne und für die Stiegengraben-Wasserhöhle eine 400-MHz-Antenne verwendet, beide in Kombination mit einem SIR 3000 GPR Controller. Mit der 80-MHz-Antenne wurden punktuelle Messungen mit einem fixen Abstand von 1 m (jeweils oberhalb der Elektroden-Position der Geoelektrik) durchgeführt. Mit der 400-MHz-Antenne wurde kontinuierlich gemessen, wobei in einem vorgegebenen Zeitintervall eine bestimmte Anzahl von Einzelmessungen durchgeführt wird. Das Aneinanderreihen mehrerer Einzelmessungen entlang eines Profils bezeichnet man als Radargramm. In Tabelle 1 sind die Parameter der beiden Radar-Antennen zusammengefasst.

Beide Methoden (ERT und GPR) reagieren auf Veränderungen der elektrischen Eigenschaften (Dielektrizität und elektrische Leitfähigkeit) im Untergrund. Tabelle 2 zeigt Literatur-Werte (Martinez & Byrnes, 2001; Knödel et al., 2005) für die zu erwartenden Materialien im Untersuchungsgebiet.

Auf Grund des sehr großen, teilweise überlappenden Wertebereichs ist es oft nicht möglich, aus nur einer geophysikalischen Messung den Aufbau des Untergrunds eindeutig abzuleiten. Daher werden häufig mehrere geophysikalische Methoden (hier Geoelektrik und Georadar) verwendet, um Mehrdeutigkeiten im geophysikalischen Modell zu reduzieren.

Tabelle 1: Parameter der GPR-Messungen.

Table 1: Parameters of the GPR measurements.

Frequenz	Wellenlänge im Vakuum	Aufnahmedauer	Messung	Spurabstand
80 MHz	3,75 m	720 ns	punktuell	1 m
400 MHz	0,75 m	110 ns	kontinuierlich	2 cm

Tabelle 2: Dielektrizitätskonstante (ϵ) und spezifischer elektrischer Widerstand (ρ) der im Untersuchungsgebiet erwarteten Materialien.Table 2: Dielectric constant (ϵ) and resistivity (ρ) for the expected material in the study region.

Material	ϵ	ρ [k Ω m]
Kalk	4–8	0,1–7
Luft	1	$1,3 \cdot 10^{13}$ – $3,3 \cdot 10^{13}$
Sediment	4–30	0,02–9
Wasser	81	0,01–0,3

MESSUNGEN

Die Messungen wurden im Juli 2017 durchgeführt, und die Profile sind in Abbildung 3 dargestellt. Die Messkampagne oberhalb des Forststraßeneinbruchs fand am 4. und 5.7.2017 bei trockenem warmem Wetter statt. Dabei wurden insgesamt sieben Profile mit Geoelektrik gemessen. Von diesen Profilen wurden zusätzlich vier mit Georadar gemessen (Abb.3). Die fehlenden drei Profile konnten aufgrund des dichten Walds mit der Georadar-Antenne nicht begangen werden. Für die Detektion des Eingangs der Stiegengraben-Wasserhöhle wurden am 26.7.2017 bei kühltem regnerischem Wetter zwei Profile oberhalb des infrage kommenden Bereichs aufgenommen (Abb.3).

Für die Auswertung und Inversion der Geoelektrik- und Georadardaten wird die Topographie des Geländes benötigt. Oberhalb der Stiegengraben-Wasserhöhle wurden die zwei Profile an die Ränder der Forststra-

ße gelegt. Die Koordinaten und die Topographie konnten daher direkt aus dem Laserscan-basierten Höhenmodell des Landes NÖ entnommen werden. Oberhalb des Forststraßeneinbruchs war es aufgrund der dichten Vegetation nicht möglich, ausreichend genaue Koordinaten aus dem digitalen Geländefeld zu erhalten, daher wurden hier die Koordinaten der Elektrodenpositionen mit Hilfe eines Tachymeters (Leica TPS 1100) aufgenommen und anschließend über einige Passpunkte in das übergeordnete System transformiert.

Die Auswertung der geophysikalischen Messungen wurde für Georadar und Geoelektrik getrennt voneinander durchgeführt. Im Folgenden werden die Ergebnisse des Profils 1 (oberhalb des Forststraßeneinbruchs) und des Profils 8 (oberhalb der Stiegengraben-Wasserhöhle) gezeigt.

AUSWERTUNG UND ERGEBNISSE

Abbildung 4 zeigt das Ergebnis der Georadar- und Geoelektrikmessungen, welche entlang des Profils 1 durchgeführt wurden. Gezeigt sind dabei nur die ersten 35 m des Profils 1, da hier der Forststraßeneinbruch darunterliegt. Das Radargramm (Abb. 4A) zeigt das Ergebnis der Messungen mit der 80 MHz-Antenne, mit der eine Erkundungstiefe von etwa 30 m erreicht werden konnte. Deutlich sichtbar ist eine Schicht, die über die gesamte Profillänge bis in eine Tiefe von ca. 1–1,5 m reicht (1), welche der obersten Schutt- und Bodenschicht entspricht und eine hohe Reflektivität zeigt. Unterhalb dieser zeigt das Radargramm eine sehr geringe Reflektivität, was für kompaktes Festgestein (hier Kalkstein) spricht. Nur im mittleren und rechten Bildbereich fallen in einer Höhe von etwa 675 m einige Regionen starker Reflektivität im sonst wenig reflektiven Opponitzer Kalk auf (2). Trotz einer vertikalen Auflösung von etwa 1,5 m und einer horizontalen Auflösung von nur ca. 3 m (80-MHz-Antenne) konnte auch im Bereich der bekannten Höhenteile (schwarzer Umriss) eine erhöhte Reflektivität festgestellt werden. Abbildung 4B zeigt das Ergebnis der Geoelektrik, wobei hier Eindringtiefen von etwa 25 m erreicht wurden. Die oberste Sedimentschicht weist hier niedrige spezifische Widerstandswerte ($\rho < 0,3 \text{ k}\Omega\text{m}$) auf, was auf das Vorhandensein von gesättigten Materialien (Boden, Lehm, usw.) hinweist (bis zu 3 m basierend auf den in Abbildung 4 beobachteten Ergebnissen). Darunter bleibt der spezifische elektrische Widerstand in einem Bereich, der typisch für Kalkgestein ist (siehe Tab. 2, 0,1–7 $\text{k}\Omega\text{m}$). Weiters

bildet sich in einer Höhe von etwa 675 m eine Anomalie mit stark erhöhtem spezifischem elektrischem Widerstand ab, was auf einen luftgefüllten Hohlraum schließen lässt. Auch hier passt die Anomalie gut mit der Position der bekannten Höhle zusammen.

Für eine bessere Vergleichbarkeit der Ergebnisse zeigt Abbildung 4C eine Überlagerung des farbkodierten Geoelektrikergebnisses mit den Georadardaten, wobei hier generell eine sehr gute Übereinstimmung festzustellen ist. Nur im Radargramm fällt noch eine weitere Stelle erhöhter Reflektivität auf (zwischen Meter 30 und 35), die jedoch von der Geoelektrik nicht bestätigt werden kann. Daraus kann man schließen, dass sich hier kein größerer luftgefüllter Hohlraum, sondern eher verfüllte Hohlräume oder kleinräumige Störungen im Gestein befinden.

Als zweites Beispiel zeigt Abbildung 5 die Ergebnisse der Geoelektrik- und Georadarmessungen oberhalb des Eingangsbereichs der Stiegengraben-Wasserhöhle. Da der Eingang dieser Höhle nur in einer Tiefe von etwa 3–4 m erwartet wird, wurde für die Georadarmessungen eine 400-MHz-Antenne verwendet, mit welcher man eine deutlich höhere Auflösung erreichen kann. Die Eindringtiefe beträgt allerdings nur etwa 5 m. Im Radargramm ist auch hier deutlich die Grenze zwischen Schutt bzw. Boden und dem darunterliegenden Festgestein zu erkennen (1). Darunter kann man zwischen Meter 25 und 35 in einer Tiefe von 3–4 m deutlich einen Bereich stark erhöhter Reflektivität abgrenzen (gestrichelte Linie in Abb. 5), bei dem es sich mit hoher Wahrscheinlichkeit um die Eingangs-

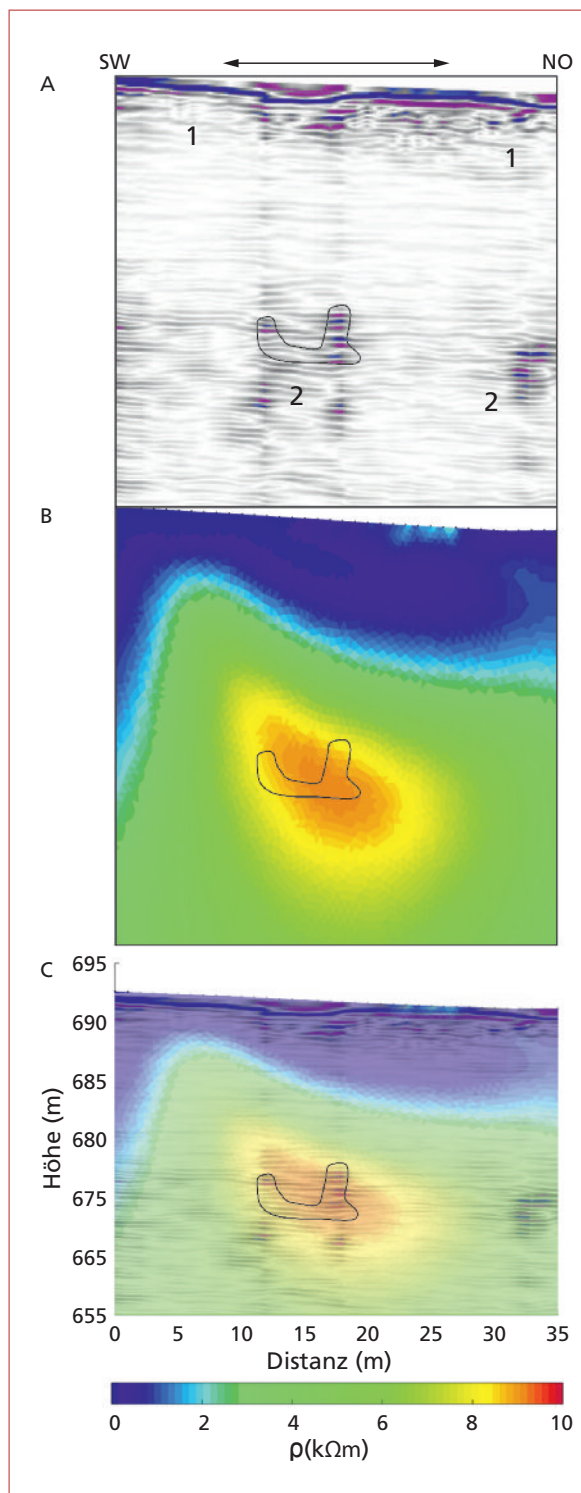
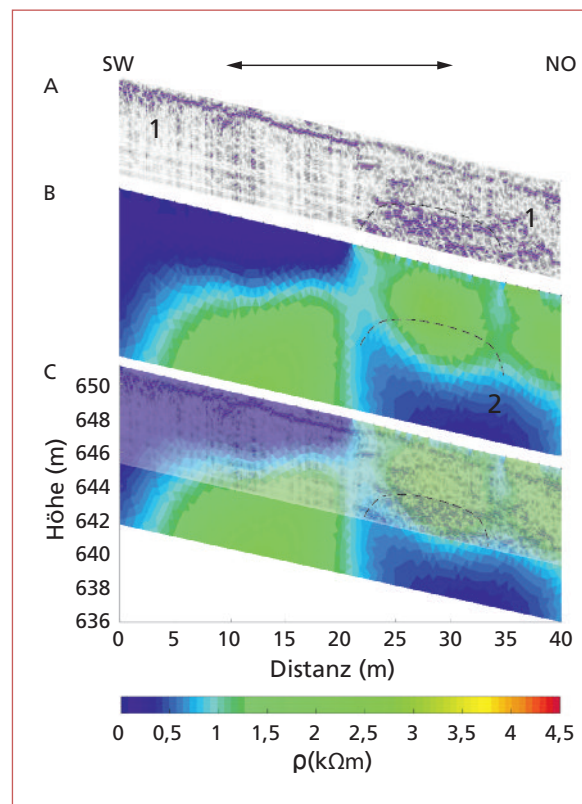


Abb. 4 (li.): Ergebnisse der Georadar und Geoelektrik Messungen des Profils 1 oberhalb des Forststraßeneinbruchs. Gezeigt sind nur die ersten 35 m, da hier die bekannte Höhle darunterliegt.

- (A) Radargramm der Punktmessungen mit der 80-MHz-Antenne.
- (B) Ergebnis der Geoelektrik Messungen. Der Farbcode des Geoelektrik Ergebnisses zeigt den spezifischen elektrischen Widerstand, wobei hohe Werte (rot)



auf einen hohen Widerstand und damit auf Hohlräume hinweisen.

- (C) Hier sind beide Ergebnisse übereinandergelegt. Der schwarze Umriss markiert die Position der bekannten Höhle.

Fig. 4 (left): Results of the GPR and ERT measurements of profile 1 above Forststraßeneinbruch. Only the first 35 m are shown, since the known parts of the cave are located below.

- (A) Radargramm von Punktmessungen mit der 80 MHz Antenne.
- (B) ERT, farblich nach Widerstandskoeffizienten kodiert, wobei hohe Werte (rot) hohe Widerstände und somit Hohlräume anzeigen.
- (C) Überlagerung beider Ergebnisse. Der schwarze Umriss markiert die Position der bekannten Höhle.

Abb. 5 (re.): Ergebnisse der Georadar und Geoelektrik Messungen des Profil 8 oberhalb der Stiegengraben-Wasserhöhle.

- (A) Radargramm der kontinuierlichen Messungen mit der 400-MHz-Antenne.
 - (B) Ergebnis der Geoelektrik Messungen. Der Farbcode des Geoelektrik Ergebnisses zeigt den spezifischen elektrischen Widerstand.
 - (C) Beide Ergebnisse übereinandergelegt. Die gestrichelte Linie markiert die vermutete Position der Eingangshalle der Stiegengraben-Wasserhöhle.
- Fig. 5 (right): Results of the GPR and ERT measurements of profile 8 above Stiegengraben-Wasserhöhle.*
- (A) Radargramm von kontinuierlichen Messungen mit der 400 MHz Antenne.
 - (B) ERT, farblich nach Widerstandskoeffizienten kodiert.
 - (C) Überlagerung beider Ergebnisse. Die gestrichelte Linie markiert die vermutete Position der Eingangshalle der Stiegengraben-Wasserhöhle.

halle der Stiegengraben-Wasserhöhle handelt. Die Geoelektrik zeigt im selben Bereich einerseits für Kalkstein typische und andererseits am unteren Rand der Region sehr niedrige spezifische elektrische Widerstandswerte. Es konnten hier daher nicht die für luftefüllte Hohlräume erwarteten Werte festgestellt werden. Dies könnte darauf hindeuten, dass die Eingangshalle unterhalb des Profils 8 wenige bis gar keine luftgefüllten Bereiche aufweist, d.h. bereits weitgehend mit Sediment verfüllt ist. Da durch die Stiegengraben-Wasserhöhle zeitweise ein kleiner Bach fließt, der bei Starkregen viel Wasser führen kann, und ihr Eingang

bereits in den 1970er Jahren verschüttet wurde, scheint eine Ansammlung von Sediment in der Halle hinter dem verschütteten Eingang wahrscheinlich zu sein. Ebenfalls denkbar wäre, dass sich durch den verschütteten Eingang das Wasser staut und so ein permanenter See entstanden ist. Solch eine Wasseransammlung würde den Strom besonders gut leiten, und der darüber liegende luftgefüllte Raum wäre dadurch unsichtbar. Beide Erklärungen würden die niedrigen spezifischen elektrischen Widerstände im Geoelektrik-Ergebnis, sowie die sehr hohe Reflektivität, welche im Radargramm beobachtet wurde, erklären.

ZUSAMMENFASSUNG

Das Ergebnis der Messungen oberhalb des Forststraßeneinbruchs zeigt sowohl in der Geoelektrik als auch im Georadar deutlich die Position der bekannten Höhle. Während man im Radargramm auch die genaue Form und Größe der Höhle recht gut erkennen kann, erreicht die Geoelektrik hier nicht die dafür nötige Auflösung. Mit der 80-MHz-Antenne konnte zwar eine Tiefe von knapp 30 m erreicht werden, allerdings bei einer Auflösung von nur 1,9–4,7 m, was die oft kleinräumigen Passagen des Forststraßeneinbruchs unsichtbar erscheinen lässt. In den Radargrammen war daher die Position des Forststraßeneinbruchs nicht immer so gut zu erkennen wie in Abbildung 5. Die Geoelektrik konnte die Position, nicht aber die Form oder Größe der luftgefüllten Hohlräume im Festgestein für alle Profile gut wiedergeben. Die erreichte Tiefe lag dabei zwischen 15 und 25 m bei einer Auflösung von ca. 0,25 m und war damit ausreichend genau, um den Forststraßeneinbruch zu detektieren. Das zweite Messgebiet lag oberhalb der Stiegengraben-Wasserhöhle, deren Eingang in den 1970er Jahren verschüttet wurde und mit Hilfe der durchgeföhrten

geophysikalischen Messungen wiedergefunden werden sollte. Die laut Plan bekannten Abmessungen der Eingangshalle der Stiegengraben-Wasserhöhle betragen 12 x 2 m in einer Tiefe von nur 3-4 m, was eine Detektion mit Hilfe geophysikalischer Methoden leicht möglich machen sollte. Tatsächlich konnte die Eingangshalle am Radargramm erkannt werden. Die Geoelektrik zeigt allerdings ein überraschendes Ergebnis, was schließlich zu der Vermutung führte, dass sich in der Eingangshalle inzwischen größere Mengen Wasser befinden oder diese zumindest teilweise mit Sediment verfüllt ist.

Zusammenfassend kann man jedenfalls sagen, dass sowohl mit Georadar als auch mit Geoelektrik auch kleinräumige oberflächennahe Hohlräume, welche potentiell gefährlich wären, sehr gut zu erkennen sind, wobei die Kombination der Methoden von Vorteil ist. Da an der Grenzen zwischen Opponitzer Kalk und Hauptdolomit mit einem hohen Verkarstungsgrad zu rechnen ist, wäre es von Interesse, auch größere Gebiete nach möglichen darunterliegenden Hohlräumen abzusuchen, was mit Hilfe geophysikalischer Methoden möglich ist.

DANK

Dank geht an Michael Behm, Werner Chwatal, Anibal David Marquina Cisneros und Antonia Golab für die Hilfe bei der Aufnahme bzw. Auswertung der Daten, sowie an das Institut für Geodäsie und Geo-

information der TU Wien für die Bereitstellung der Instrumente.

Georg Kaufmann und ein anonymer Gutachter haben wertvolle Hinweise gegeben.

LITERATUR

- Abrahamczik, W. (1936): Karsterscheinungen in der Umgebung von Lunz am See, mit besonderer Berücksichtigung der Höhlen. – Unveröff. Diss. Univ. Wien.
Bauer, F.K., Ruttner, A. & Schnabel, W. (1988): Geologische

- Karte der Republik Österreich – Blatt 71, Ybbsitz.
– Wien (Geologische Bundesanstalt).
Behm, M., Plan, L. & Roch, K.H. (2005): Erfolgreicher Versuch einer Höhlendetektion mit Georadar (GPR). – Die Höhle, 56: 20-23.

- Chamberlain, A.T., Sellers, W., Proctor, Ch. & Coard, R. (2000): Cave detection in limestone using Ground Penetrating Radar. – *Journal of Archaeological Science*, 27: 957-964.
- Frid, V., Averbach, A., Frid, M., Dudkinski, D. & Liskevich, G. (2015): Statistical analysis of resistivity anomalies caused by underground caves. – *Pure and Applied Geophysics*, 174: 997-1012.
- Hartmann, H. & Hartmann, W. (1985): Die Höhlen Niederösterreichs, Band 3. – Die Höhle, Beiheft 30.
- Kaufmann, G., Nielbock, R. & Romanov, D. (2015): The Unicorn Cave, Southern Harz Mountains, Germany: From known passages to unknown extensions with the help of geophysical surveys. – *Journal of Applied Geophysics*, 123: 123-140.
- Kaufmann, G. & Romanov, D. (2017): The Jettencave, Southern Harz Mountains, Germany: Geophysical observations and a structural model of a shallow cave in gypsum/anhydrite-bearing rocks. – *Geomorphology*, 298: 20-30.
- Knödel, K., Krümmel, H. & Lange, G. (2005): Handbuch zur Erkundung des Untergrundes von Deponien und Altlasten. – Band 3, Geophysik, Berlin (Springer).
- Martinez, A. & Byrnes, A.P. (2001): Modelling Dielectric-constant values of geological materials: An aid to Ground-Penetrating Radar data collection and interpretation. – *Current Research in Earth Science*, Bulletin 247: 1-16.
- Redhaounia, B., Ilondo, B.O., Gabtni, H. & Sami, K. (2016): Electrical Resistivity Tomography (ERT) applied to karst carbonate aquifers: Case study from Amdoun, northwestern Tunisia. – *Pure and Applied Geophysics*, 173: 1289-1303.
- Süssenbeck, H. (1974): Die Erforschung der Stiegengraben-Wasserhöhle (1823/25) im Schöpfertaler Wald bei Lunz/See. – *Höhlenkundl. Mitt. Wien*, 30: 221-231.

4.2 Measurements

A detailed description of all measurements (including date, site, measurement set-up, ...) can be found in the paper in section 4.1. A short summary of all performed measurements is given here for the Forststraßeneinbruch and the Stiegengraben-Wasserhöhle. A detailed description of all used methods can be found in section 2.

- **Forststraßeneinbruch**

Above the Forststraßeneinbruch, the following measurements were carried out:

- **ERT, IP:** ERT and IP measurements were performed along all seven profiles (see paper for details) using a Syscal device (Syscal Pro Switch 72, IRIS Instruments). The distance between the electrodes was always 1 m, resulting in a profile length of 71 m, a resolution of about 0.25 m and a reachable depth of about 15 m. For all recordings, a dipole-dipole configuration with skip levels from 0-11 was used. A more detailed explanation of this choice is summarized in section 3.
- **GPR:** For all profiles that are accessible with the GPR antennas (see paper), measurements were taken with an 80 MHz (point measurements) and an 200 MHz (continuous measurements) antenna (not shown in the paper).
- **CMD:** CMD measurements using a CMD-MiniExplorer from Gf Instruments were carried out along all seven profiles above the Forststraßeneinbruch.
- **Coordinates:** As already described in the paper, the coordinates of the electrodes of all profiles were recorded, using a tachymeter (Leica TPS 1100). Since several stations were required to record all profiles, some control points were additionally marked and measured from each station. A detailed description of the following evaluation steps can be found in 4.3.1.

In addition to the geophysical and geodetic data collected during the campaign, the coordinates of the cave survey of the Forststraßeneinbruch were also available. In section 5.1 we give a description of the methods, the methods and the outcome of cave surveys and how they can be used to build models of the subsurface.

- **Stiegengraben-Wasserhöhle**

A smaller campaign with only two profiles was carried out above the Stiegengraben-Wasserhöhle. It is mostly presented in the paper, thus we refer to the paper for details.

4.3 Evaluation and Results

This work focuses mainly on the applicability of electrical methods (ERT/IP) to cavity detection, as well as on the combination of electrical methods with data from cave surveys. Thus, we will present results of all ERT/IP measurements above Forststraßeneinbruch, for which also cave survey data exist. One example (profile 1) can also be found in the paper. Since GPR- and CMD-measurements were also carried out in the test areas, these are also shown exemplary and are compared with the results from ERT/IP measurements. A precise knowledge of the position and orientation of the profiles is of importance for a later comparison of the cave survey with the results obtained for the different profiles. Thus, we present all necessary steps and the final

outcome in the following. Above Stiegengraben Wasserhöhle only a few measurements were carried out, which are all presented in the paper. We therefore do not repeat them here.

4.3.1 Profile coordinates

The positions of every tenth electrode were recorded in the form of distance, azimuth and inclination with a tachymeter (Leica 1100) in free placement. Thus, in a first step distance and angles were transformed to X-,Y-,Z-coordinates. Since three locations were required for the recordings of all profiles, in a second step all measurements were transformed into the local coordinate system of station 1. For this purpose, four control points distributed in the measuring area were recorded from all stations. With the help of these control points, the X- and Y-coordinates recorded from station 2 and 3 were transformed to the coordinate system of station 1 using a 2D Helmert-transformation (Navratil, 2006) with four unknowns (2 translations (a, b), one rotation (α) and a scale factor (m)). The transformation can then be represented as follows, where x and y are the original coordinates and X and Y are the transformed coordinates:

$$\begin{pmatrix} X \\ Y \end{pmatrix} = \begin{pmatrix} a \\ b \end{pmatrix} + m \begin{pmatrix} \cos\alpha & -\sin\alpha \\ \sin\alpha & \cos\alpha \end{pmatrix} \begin{pmatrix} x \\ y \end{pmatrix} \quad (18)$$

For convenience, the scale and rotation angle can be combined into two new variables:

$$c = m \cdot \cos\alpha, \quad d = m \cdot \sin\alpha \quad (19)$$

Thus, the equations of motion of the Helmert transformation are as follows:

$$\begin{aligned} X_i + v_{x_i} &= a + x_i c - y_i d \\ Y_i + v_{y_i} &= b + y_i c + x_i d \end{aligned} \quad (20)$$

The coefficient matrix (A) then becomes:

$$A = \begin{pmatrix} 1 & 0 & x_1 & -y_1 \\ 0 & 1 & y_1 & x_1 \\ 1 & 0 & x_2 & -y_2 \\ 0 & 1 & y_2 & x_2 \\ \vdots & \vdots & \ddots & \ddots \\ \vdots & \vdots & \ddots & \ddots \end{pmatrix} \quad (21)$$

and the observation vector (l) can be calculated according to equation 20, where approximated values for the transformation parameter have to be used. The calculation of the addition to the transformation parameters (atp) can be done according to the following formulas:

$$atp = (A^T A)^{-1} A^T l \quad (22)$$

Table 3: Gaps between the original and the transformed control points for station 2 and 3

Station 2	Δy [mm]	Δx [mm]	Station 3	Δy [mm]	Δx [mm]
Point 1	-0.1	-4.0	Point 1	-11.5	-16.5
Point 2	0.2	1.2	Point 2	1.6	16.1
Point 3	0.4	1.0	Point 3	2.1	-9.5
Point 4	-0.5	1.8	Point 4	7.8	10.0

The transformation parameters then equals:

$$\begin{pmatrix} a \\ b \\ c \\ d \end{pmatrix} = \begin{pmatrix} a \\ b \\ c \\ d \end{pmatrix} + \begin{pmatrix} atp1 \\ atp2 \\ atp3 \\ atp4 \end{pmatrix} \quad (23)$$

Using these parameters, the transformation can be calculated. To give the parameters for the scale and the rotation, they have to be calculated from the parameters c and d:

$$m = \sqrt{c^2 + d^2}, \quad \tan \alpha = \frac{d}{c} \quad (24)$$

One can obtain an estimate of the accuracy of the transformation by using the differences in the coordinates between the control points in the original and in the transformed coordinate system. A Helmert transformation has now been calculated for all points taken from station 2 and 3. Table 3 gives the gaps between the original and the transformed control points for station 2 and 3. As can be seen, all gaps are below 2 cm, which is sufficient for the evaluation of the geophysical measurements. Figure 17 shows the results of the transformation, with the different coloured dots corresponding to the measurements from the three different stations. The heights belonging to the respective measurements were calculated trigonometrically and are added to the heights of the control points taken from station 1. The resulting 3D points of all measured electrode positions were now used to interpolate the coordinates for all intermediate electrode positions. Since the terrain does not show any significant altitude fluctuations, a linear interpolation was used. The resulting complete coordinate set of all electrode positions of the seven profiles can now be used for the further evaluation.

To allow a display of the profiles on a map, the coordinates were transformed to the BMN M34 coordinate system, using a few control points and another Helmert transformation. The result is shown in Figure 3 of the paper (section 4.1). The positions of the control points are only inaccurately known, resulting in differences of about some meters between the control points in the two coordinate systems. Therefore, the local coordinate system was retained for the further evaluation (section 5.1).

4.3.2 ERT/IP

In the following section, the results of all seven measured ERT/IP profiles are shown, as well as the necessary evaluation steps explained by using a sample profile (profile 6). The following steps are performed for the data analysis, the filtering of outliers and the creation of the ERT/IP

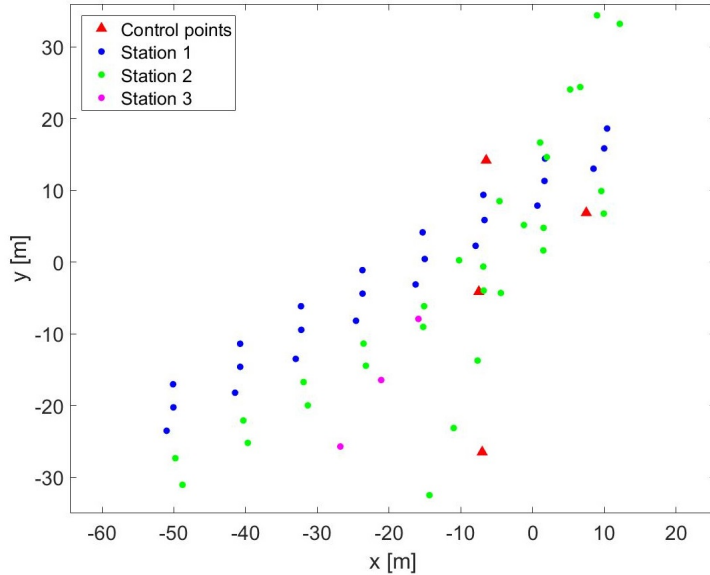


Figure 17: Positions of all measured points after the coordinate transformation, plotted in the local coordinate system of station 1. Given are the four control points (red triangles) and the coordinates of all electrodes measured from station 1 (blue), from station 2 (green) and from station 3 (magenta).

images:

- **Raw data:** All measurements were performed with a Syscal Pro Switch 72 from IRIS Instruments. The data can be downloaded from the instrument using the Prosys program and are saved to a text file, in which the electrode positions, the apparent chargeability (m), the voltage (V) and the used current (I) is given. Using voltage and current one can calculate the apparent resistivity (U/I). For a first check a pseudosection (figure 18) is plotted using the unfiltered measurements. Such pseudosections can be used to get a first estimate of the data quality. In particular, the occurrence of many outliers, as well as the presence of defective electrodes would be particularly noticeable. This is not the case in the shown example and in all other profiles, thus we can conclude a fairly good data quality. Nevertheless, there are some points that do not match the values of the surrounding points and which therefore could be outliers. Thus, in a next step, the data are filtered.
- **Processing:** For the filtering of the data, the use of histograms, which represent the distribution of the recorded data, is suitable. Figure 19 shows in the first line (left: apparent resistivity, right: apparent chargeability) the histograms of the raw data, which still contain all erroneous measurements and outliers. Since neither the apparent resistivity nor the apparent chargeability can have values below zero, in a first step all negative and therefore certainly erroneous measured values are removed (figure 19, second line). All measurements have been performed only once, thus the use of statistical methods for the identification of outliers is not applicable. Therefore, an appropriate cut at the high end was set as well (figure 19, third line). This resulting data set was then used for the inversion.

• **Inversion:**

The program CRTomo (Kemna et al., 2000) was used for the inversion of the data. It

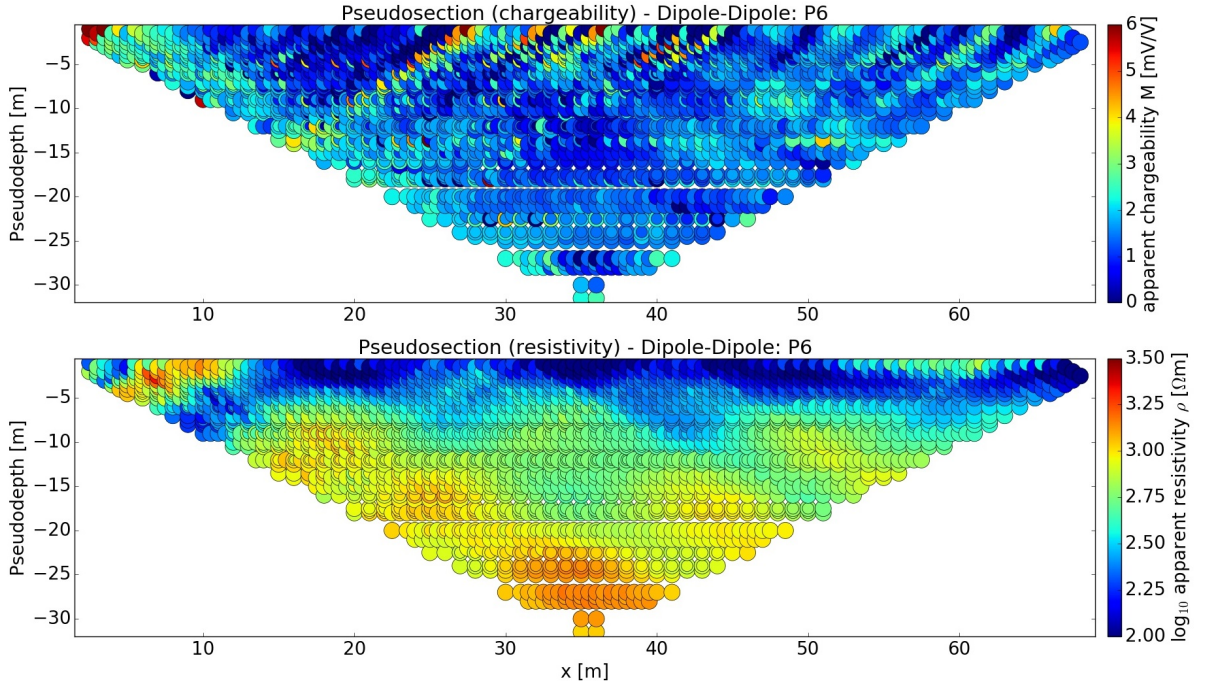


Figure 18: Pseudosection using the unfiltered measurements of profile 6.

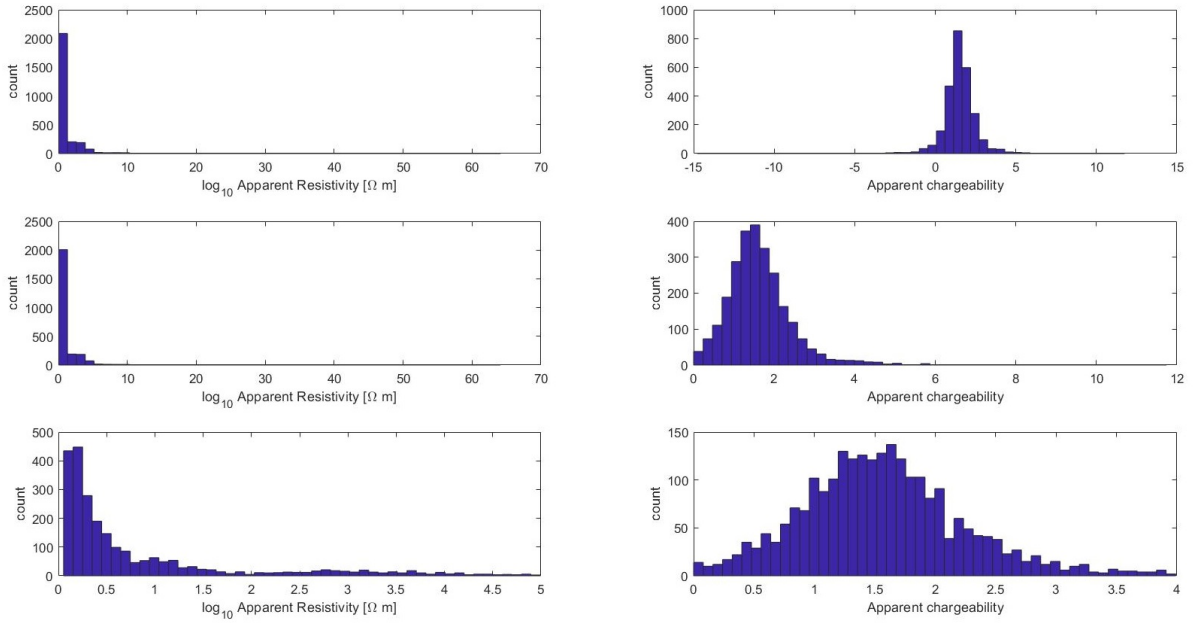


Figure 19: Histograms of the apparent resistivity (left column) and the apparent chargeability (right column) for the raw data (first row), the data, when all negative values are filtered out (second row) and the data after filtering of outliers (third row).

requires in addition to the measured data, values for the random errors of apparent resistivity and apparent chargeability. The exact distribution and dispersion of these random errors are not known, thus they must be estimated. The inversion algorithm in CRTomo uses a linear relationship between the measured values (R) and their errors (s_R):

$$s_R = a + bR, \quad (25)$$

where a is the absolute error at low resistance values and b is a relative error (in percent) for higher resistance values. The values for a and b could be estimated using two measurements (normal and reciprocal, where the current and potential electrodes are changed, LaBrecque (1996)). However, since the measurements for all the profiles presented here were only performed once, the best values for a and b had to be determined by testing different combinations. The phase errors used in CRTomo can be given according to the following relationship (Flores Orozco et al., 2012):

$$s_\varphi = aR^b, \quad (26)$$

or as a constant value (Slater, 2006). As for the resistivity the error values had to be determined by testing therefore a constant value for the phase error was taken. The best results for all profiles were achieved with the following error values:

Resistance errors: $a = 5\%$, $b = 0.01$

Phase errors: 0.5

The filtered measurements and the determined errors were then used to calculate inversions of all seven investigated profiles. Figure 20 and 23 show the results, where the left column shows the resistivity and the right column the phase. All values with a sensitivity <-3 have been removed from the images (see section 3 for details), as no meaningful result can be expected here (Weigand et al., 2017). Despite removing the values with too low sensitivity, penetration depths of at least 20 - 25 m were reached for all profiles. Thus, the penetration depth was sufficient to reach all the underlying known cave parts. For the resistivity images (figures 20 and 23, left column) the colour code was chosen as follows:

- **Blue:** Shades of blue correspond to resistivity values up to about 500 Ωm , which represents a conductive material such as soil or clay.
- **Green:** Shades of green represents less conductive media up to a resistivity of about 6000 Ωm . In the investigated region this corresponds most likely to the bedrock, build of limestone.
- **Red:** Shades of red correspond to even less conductive materials with a resistivity greater than about 6000 Ωm , and therefore may be interpreted as air-filled voids in the study area.

The images of the phase (figures 20 and 23, right column) reflect the storage capacity of the subsurface via the colour code, the bandwidth ranging from no storage capacity (dark blue) to very good storage capacity (dark red). With the materials one can assume that dry limestone

or gravel, as it lies on the forest roads, has a poor storage capacity. Good storage capacity, in contrast, can be expected from wet soil or clay that often occurs in caves. A summary of all visible features and their possible interpretation in the seven profiles is given below:

- Profile 1 (P1):** In the resistivity image of P1 (figure 20, left column, first row), one can clearly see the boundary between the soil layer (dark blue) and the bedrock (green), with the soil layer missing from about the middle of the profile. In this region P1 runs directly on a forest road, which was built in the bedrock. Therefore, one can assume that the soil layer is actually missing and only some dry gravel lied on the bedrock, which would lead to a similar resistivity. At the beginning of the profile, the soil layer reaches depths of just under 2 and up to about 7 m. Apart from that an anomaly with a very high resistivity is noticeable. It is located at the beginning of the profile between meters 10 and 30, at a height between about 670 and 680 m. From this high resistivity values one can conclude the presence of a cavity. The image of the phase (figure 20, right column, first row) shows mostly very low values and thus a very low chargeability of the subsurface materials. However, there is also an anomaly with significantly higher values. This is also at the beginning of the profile between meters 0 and 10 at a height between about 680 and 690 m. There are no peculiarities in the resistivity image here, so a possible explanation could be the existence of narrow cracks or fissures with clay or wet soil, which could significantly increase the chargeability but not necessarily lead to increased resistivity values.

To better estimate the exact depth of the resistivity anomaly, the inversion of the data was repeated for different skip-levels (skip 0-3, for an explanation see section 2). Therefore, the measurements corresponding to one specific skip level were extracted and inverted separately. Figure 21 shows the ERT images for all four inverted skip-levels. The ERT image for skip-level 0 shows a much lower resistivity up to the middle of the picture. Thus, one can conclude that the soil layer at the beginning of the profile reaches down relatively deep. From skip-level 1 on, the boundary between the soil layer and the bedrock can be seen, which lies approximately in a depth of 2 to 4 m. At skip-level 3 one can see the first signs of the resistivity anomaly, which indicates that the causative cavity is below a height of about 680 m. The later comparison with the data of the cave survey (section 5.2) confirms this assumption.

- Profile 2 (P2):** The resistivity image of P2 (figure 20, left column, second row) also clearly shows the boundary between the soil layer (dark blue) and the bedrock (green). At the beginning of the profile, the soil layer has a depth of about 3 m, in the middle only about 1.5 m, and towards the end it reaches again a depth of about 3 m. This figure also shows an anomaly with a remarkable high resistivity, which is located between meters 15 and 50 at a height between about 670 and 685 m. Again, it could be concluded that there is a large cavity. However, the image of the phase (figure 20, right column, second row) also shows an anomaly in the same area with significantly increased chargeability, which does not support a large cavity. Eventually, the existence of several, small air or clay filled voids could explain these results.

For a better estimate of the depth of the resistivity anomaly, the inversion of the data was

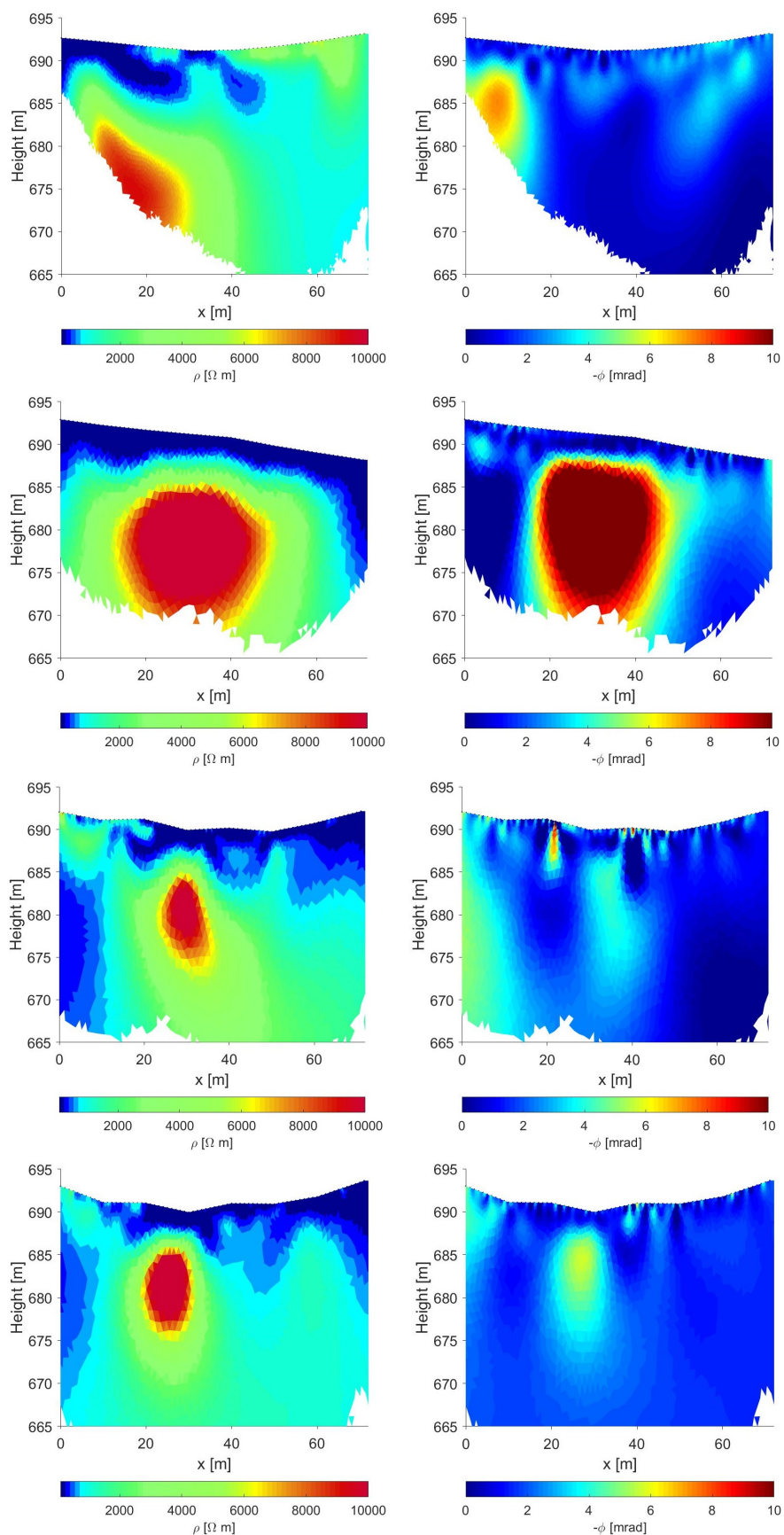


Figure 20: ERT (left) and IP (right) images from the measurements above Forststraßeneinbruch. From top to bottom: Profile 1, 2, 3 and 4.

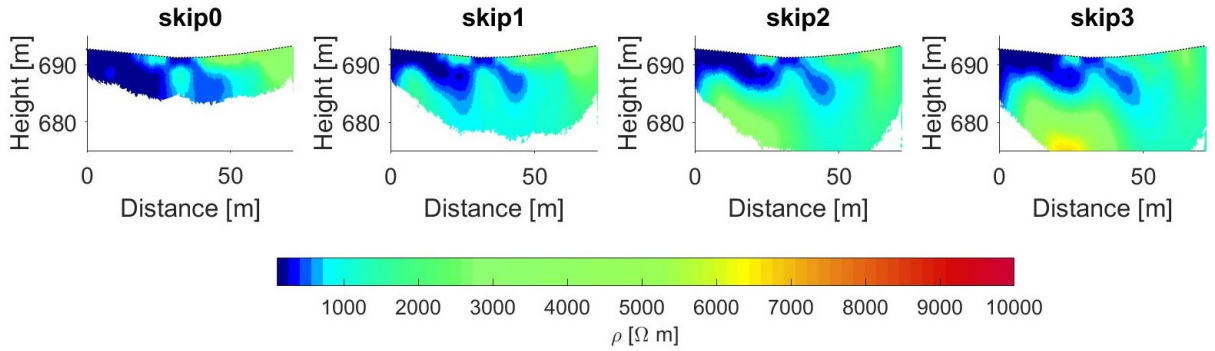


Figure 21: ERT image of profile 1 inverted for different skip-levels, from left to right: skip 0, skip 1, skip 2, skip 3.

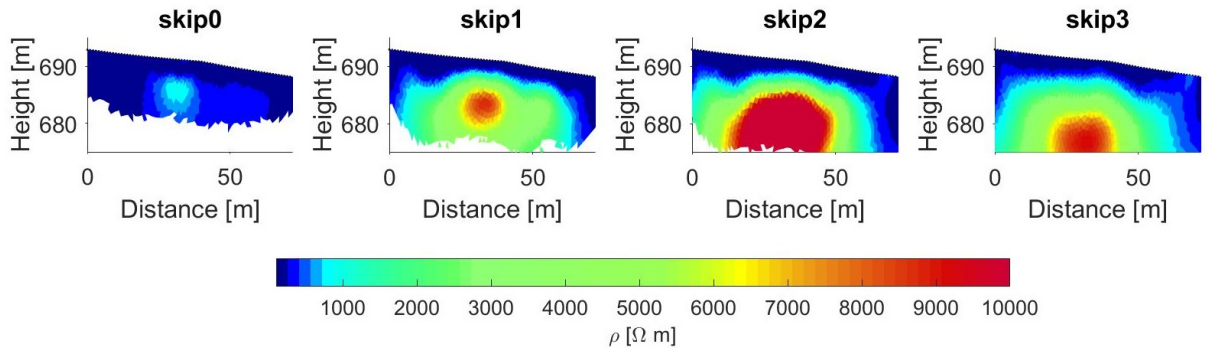


Figure 22: Like figure 21, but for profile 2.

again repeated for different skip-levels (skip 0-3). Figure 22 shows the ERT images for all four inverted skip-levels. Already the ERT image of skip level 0 and more clearly at skip level 1 indicates an anomaly at a height of approximately 685 m. At skip level 2, the anomaly becomes very large, indicating the existence of more cavities at greater depths. Also, the fact that at skip level 3 the near-surface anomaly is no longer recognizable, but a lower one (below 680 m), is indicative of the existence of two nearly superimposed anomalies.

3. **Profile 3 (P3):** In the resistivity image (figure 20, left column, third row), the boundary between the bedrock and the soil is also clearly visible. At the beginning of the profile, the soil layer is only a few centimetres wide, which seems realistic, since the profiles P3-P7 are reaching the wall of a former quarry. Thus, the approach of the bedrock to the surface is likely. Towards the end of the profile the soil layer becomes much deeper, reaching depths of up to 10 m. Additionally, P3 shows two anomalies: The first at the very beginning of the profile (meters 0 - 10) with a significantly lower resistivity than the surrounding rock. This anomaly begins at a height of about 685 m and reaches down to the resolution limit. A second anomaly, this time with significantly increased resistivity, can be found between meters 25 and 35 at a height between 675 and 685 m. In the image of the phase (figure 20, right column, third row) an anomaly at the beginning of the profile is also visible, which agrees with the one in the resistivity plot. Here one can assume that it contains a material that has both a good conductivity and a high chargeability, such as clay or wet soil. At the

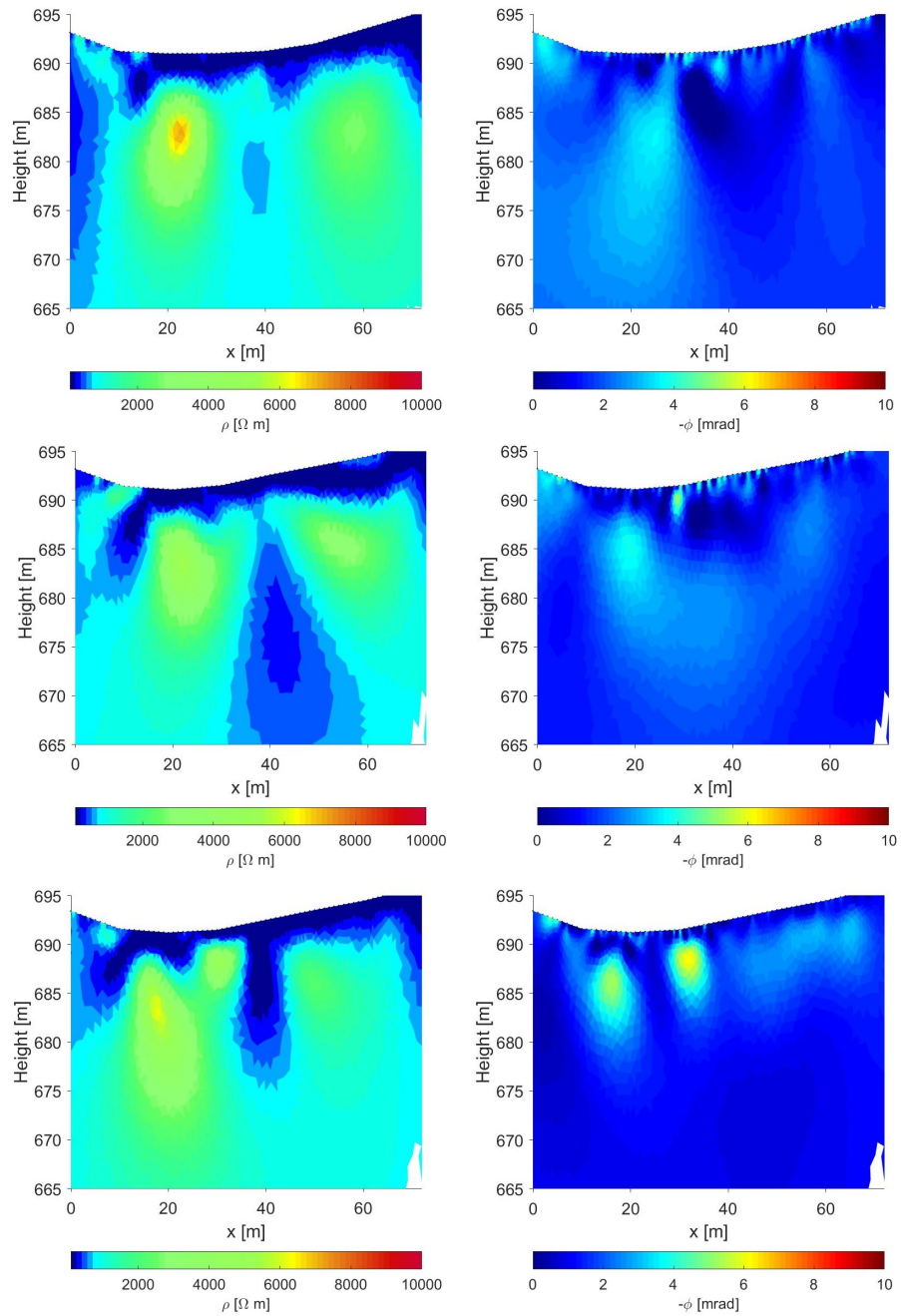


Figure 23: ERT and IP images from the measurements above Forststrasseinbruch. From top to bottom: Profile 5, 6 and 7.

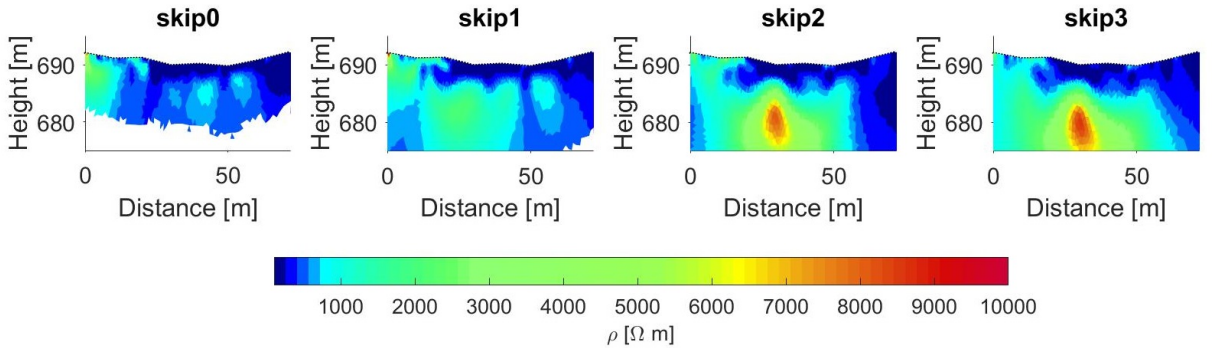


Figure 24: Like figure 21, but for profile 3.

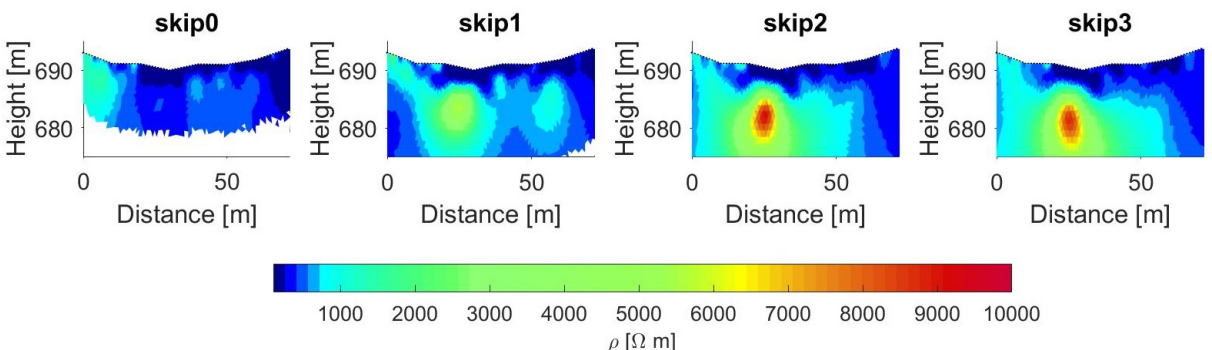


Figure 25: Like figure 21, but for profile 4.

edge of the second resistivity anomaly, an area (between meters 30 and 40 at a height of 675 - 685 m) with an increased chargeability is also visible in the phase image. These could be walls covered with clay, or narrow, clay-filled cracks in the area of the cavity. The phase image shows an additional near-surface anomaly with a very high chargeability between meters 20 and 25. This could also be a crack, filled with clay or wet earth.

Like for the previous profiles, the inversion of the data was repeated for different skip-levels (skip 0-3) to better estimate the depth of the anomaly. Figure 24 shows the ERT images for all four inverted skip-levels. In the ERT images of skip level 0 and clearer at skip level 1, one can see the boundary between the soil layer and the bedrock. From skip level 2 on, the anomaly becomes increasingly apparent, indicating that the anomaly is located at about 680 m.

4. **Profile 4 (P4):** The resistivity (figure 20, left column, fourth row) and phase (figure 20, right column, fourth row) images of P4 are quite similar to the images of P3. In the resistivity plot one can again recognize the two anomalies (low resistivity between meters 0 and 10, and high resistivity between meters 20 and 30). Here, however, the well-conducting anomaly hardly forms in the phase image, but the anomaly with high resistance seems much clearer.

Again the inversion of the data was repeated for different skip-levels (skip 0-3) to better estimate the depth of the anomaly. Figure 25 shows the ERT images for all four inverted skip-levels. Also the analysis of the ERT images at different skip levels shows clearly a similarity to the images of profile 3. Again the anomaly is clearly visible from skip level 2

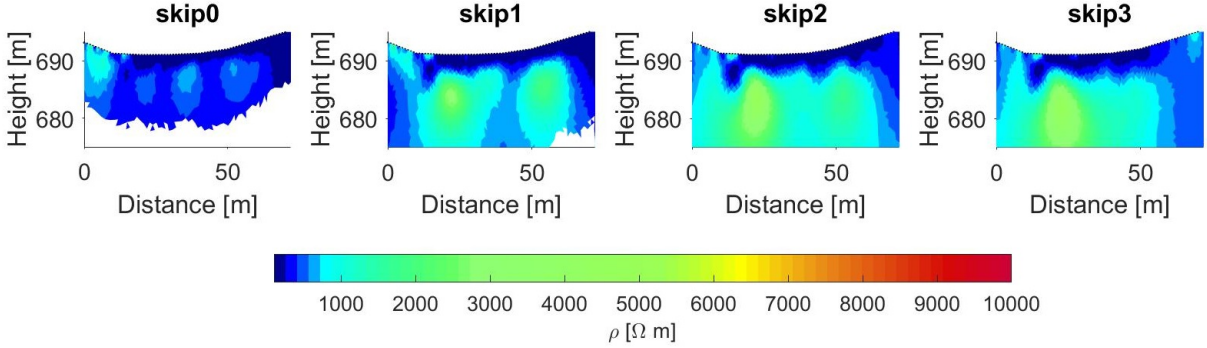


Figure 26: Like figure 21, but for profile 5.

on. So, the analysis of the skip levels suggests that the anomaly visible in the neighbouring profiles 3 and 4 is a larger cavity, which is visible in the data of both profiles. Nevertheless, the later comparison between the cave survey and the ERT images in combination with a modelling will show that this is probably not the case (see section 5.2).

5. **Profile 5 (P5):** The resistivity image (figure 23, left column, first row) of P5 looks similar to those of P3 and P4, where the anomaly with high resistivity around meter 25 is still visible, but smaller and less clear than in profiles 3 and 4. An additional conductive anomaly appears in the resistivity image between meters 35 and 40 at altitudes between 675 and 682 m. This could be an area where the bedrock is interrupted by gaps filled with sand or soil. The phase image (figure 23, right column, first row) of P5 generally shows a very low chargeability. Just in the area of the high resistivity anomaly a slight increase in chargeability can also be detected in the phase image.

To better estimate the depth of the resistivity anomaly, the inversion of the data was again repeated for different skip-levels (skip 0-3). Figure 26 shows the ERT images for all four inverted skip-levels. At skip level 0 one can just see the border between the soil layer and the bedrock. At skip level 1 the conductive anomaly between meters 35 and 40 is clearly visible. Since at skip levels 2 and 3 the conductive anomaly disappears again, it is likely located relatively close to the surface. The anomaly with a high resistivity is not clearly visible in any of the skip levels, which indicates that the causing cavity is quite small and therefore visible just in the image using all the skip levels.

6. **Profile 6 (P6):** The resistivity image (figure 23, left column, second row) of P6 still looks similar to that of the neighbouring profile P5, with the behaviour of the two conductive anomalies changing significantly. While the anomaly at the beginning of the profile has almost completely disappeared, the second conductive anomaly at meter 40 is very clear and almost reaches the surface. An anomaly with high resistivity is not visible in P6. Also the phase picture (figure 23, right column, second row) looks very similar to the one of P5 and thus shows a very low chargeability. As with P5, there is a slight increase in chargeability at about meter 20, with no anomaly at the same point in the resistivity plot. Again the inversion of the data was repeated for different skip-levels to check whether any depth information can be obtained. Figure 27 shows the ERT images for all four inverted skip-levels. Also the inversions of the different skip levels look very similar to those of

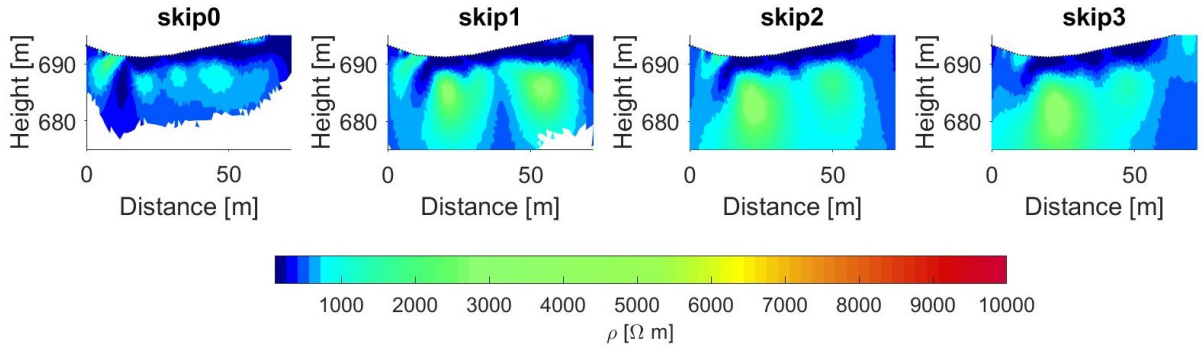


Figure 27: Like figure 21, but for profile 6.

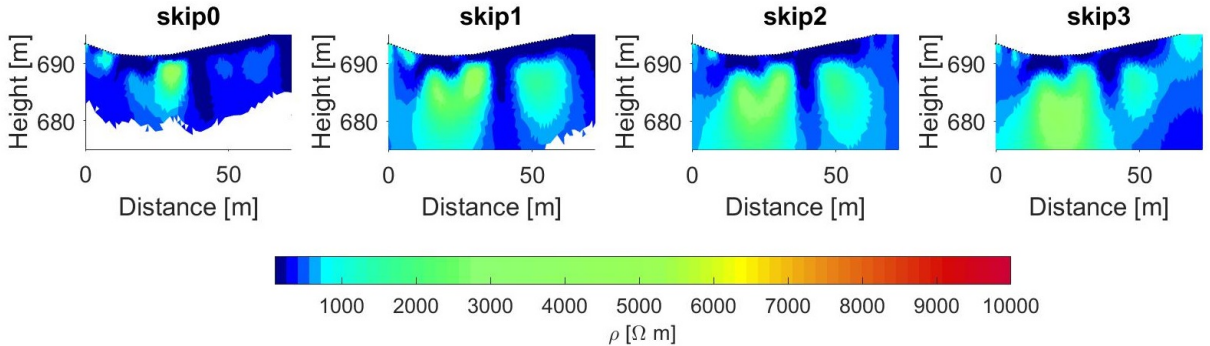


Figure 28: Like figure 21, but for profile 7.

profile 5. Again, the conductive anomaly is only visible in skip-level 1, which indicates that it does not reach very low altitudes. An anomaly with high resistivity is also not recognizable in the inversions of the individual skip levels.

7. Profile 7 (P7): The resistivity image (figure 23, left column, third row) of P7 is also quite similar to that of the neighbouring profile P6, especially the boundary between bedrock and soil shows a very similar behaviour. The conductive anomaly at meter 40 shrinks here compared to P6 and is not that deep anymore, but clearly reaches the surface. Also in P7 no clear anomalies with high resistivity values are recognizable, whereby there is an increase of resistivity before meter 20 at a height of just 685 m. In contrast to P6, the phase image (figure 23, right column, third row) shows again two anomalies with a significantly increased chargeability. A first between meters 15 and 20 at a height of about 685 m and a second between meters 30 and 35 at a height of about 688 m.

Finally also for profile 7 the inversion of the data was repeated for different skip-levels to obtain further depth information. Figure 28 shows the ERT images for all four inverted skip-levels. In contrast to profiles 5 and 6, the conductive anomaly remains visible in all skip levels, suggesting that there may be a crack filled with sediment that reaches further down. As in profiles 5 and 6, no anomaly with high resistivity is recognizable. Also the anomaly which can be suspected in figure 23 (left column, third row) between meter 15 and 20 can not be seen in the inversions of the individual skip-levels.

In order to improve the interpretation of the resulting images, in a next step the positions of the anomalies are compared with the positions of the known cave parts (see section 5.2). In addition,

the cave survey is used to create electrical models of the subsurface (see section 5), which can be inverted and also compared to the actual measurements. So it is possible to separate all anomalies caused by the known cave from those that are not caused by known parts of the cave.

4.3.3 CMD

Along all seven profiles above the Forststräßeneinbruch, measurements were taken with a CMD-MiniExplorer from Gf Instruments. This instrument provides simultaneous measurements of the conductivity (σ) at three different depths, namely 0.5, 1.0, and 1.8 m. The conductivity can be easily converted into resistivity ($\rho = 1/\sigma$) and compared with the results of the ERT measurements. Therefore, the resistivity values for these three depths were extracted from the ERT results and displayed together with the CMD results (figures 29-35). In general, the resistivity values from the CMD measurements (red dots) are lower (always below 500 Ωm) and show a more uniform trend than the values taken from ERT inversion (blue dots). To represent both values in a plot, the resistivity values were restricted to a range of 0-500 Ωm . As a result, some of the resistivity values from ERT inversion are missing, as they are above 500 Ωm in these areas. Since both the CMD and the ERT results tend to show low resistivity values in most cases, one can conclude that the soil layer, with a few exceptions, reaches a depth of at least 1.8 m. A detailed description of the results of each profile is given below:

- 1. Profile 1:** Figure 29 (first row) shows the resistivity values obtained by CMD for a depth of 0.5, 1.0 and 1.8 m. Up to meter 20 the resistivity values are quite similar for all three investigated depths and are almost constant. From meter 20 on the resistivity values in all three depths start rising, where the resistivity close to the surface (at 0.5 m) is the highest. Here, profile 1 runs on a forest road with loose gravel on the bedrock, which could explain the high resistivity close to the surface.

Figure 29 (second to fourth row) show the comparison of resistivity values from CMD and ERT measurement. Profile 1 shows the largest difference between this two measurements. While the ERT resistivity reaches values of up to 5000 Ωm from the middle of the profile on (see also figure 20, first row) and therefore does not appear in figure 29, the CMD resistivity values are always below 500 Ωm . Nevertheless, the CMD resistivity values in profile 1 show the strongest increase of all profiles and reach the highest values of almost 500 Ωm . The near-surface CMD measurements (figure 29, second and third row) show a strong scattering from about the middle of the profile. Again the gravel on the forest road could explain the poor coupling and thus the very high resistivity values of the ERT measurement, as well as the relatively high resistivity values and the strong scattering of the CMD measurement. A closer look at these strong differences is made in section 5.2 by modelling.

- 2. Profile 2:** For profile 2 the resistivity values measured with CMD (figure 30, first row) show a quite similar behaviour as in profile 1. The resistivity values in a depth of 1.0 and 1.8 m behave again almost the same and the surface-near section (at 0.5 m) shows again higher resistivity values along the whole profile, probably caused by loose, dry material in the uppermost soil layer.

The comparison of the resistivity values from CMD and ERT measurements for profile 2

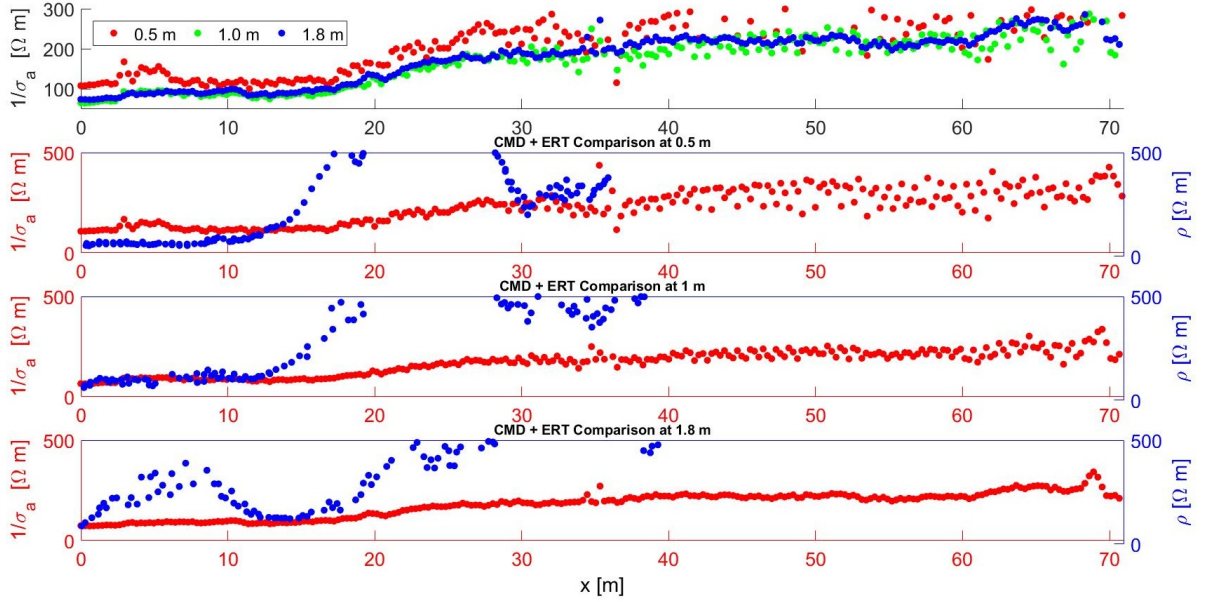


Figure 29: First row: Resistivity values measured with CMD in a depth of 0.5 (red dots), 1.0 (green dots), and 1.8 m (blue dots). Second-third row: Comparison between resistivity values obtained by CMD (red dots) respectively ERT (blue dots) for profile 1. First row for a depth of 0.5 m; second row for 1.0 m and third row for 1.8 m.

is shown in figure 30 (second to fourth row). For the two near-surface sections (figure 30, second and third row) a very good agreement can be found. The comparison at a depth of 1.8 m (figure 30, fourth row) still shows a fairly good agreement, but in the range between meters 20 and 60 the resistivity values from the ERT measurement are already well above those of the CMD measurement. This could indicate that the boundary to the bedrock is just below this depth (see also figure 20, second line). Due to the smoothing of the ERT inversion, the ERT resistivity values increase a bit, while the CMD measurement still shows the resistivity values of the soil layer.

3. Profile 3: Figure 31 (first row) shows the resistivity values measured with CMD at a depth of 0.5, 1.0 and 1.8 m. At the beginning of the profile (up to approximately meter 25), the near-surface resistivity values are again slightly higher than those of the deeper sections. Profile 3 starts at the base of a former quarry, so there may be some loose rubble there, which could explain the increased resistivity values near the surface. After that, the cuts in all three depths show a very similar behaviour.

Figure 31 (second to fourth row) shows the comparison of the resistivity values measured by CMD and ERT for profile 3. The loose boulders at the base of the cliff could be again the reason for a poor coupling and therefore the high ERT resistivity values at the beginning of the profile. From meter 25 onwards, the near-surface sections (figure 31, second and third row) show a quite good match between the CMD and ERT resistivity values. In the comparison in 1.8 m depth (figure 31, fourth row) the ERT resistivity values are increased again compared to the CMD resistivity values. Similar to profile 2, this could be traced back to the near boundary to the bedrock (see Figure 20, third row).

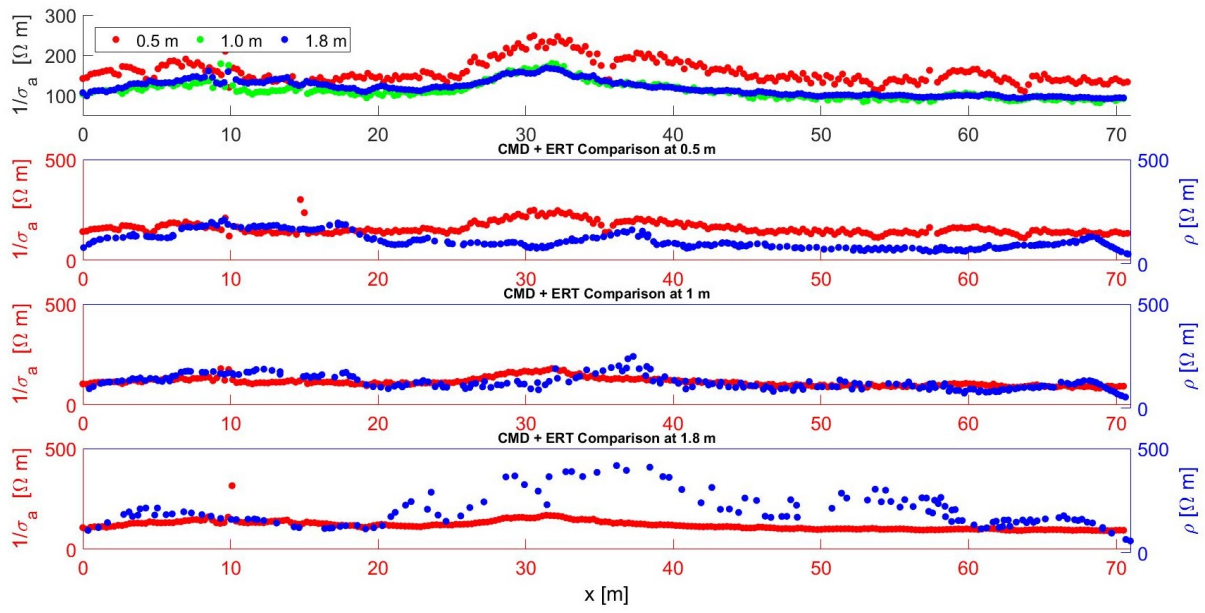


Figure 30: Like figure 29, but for profile 2.

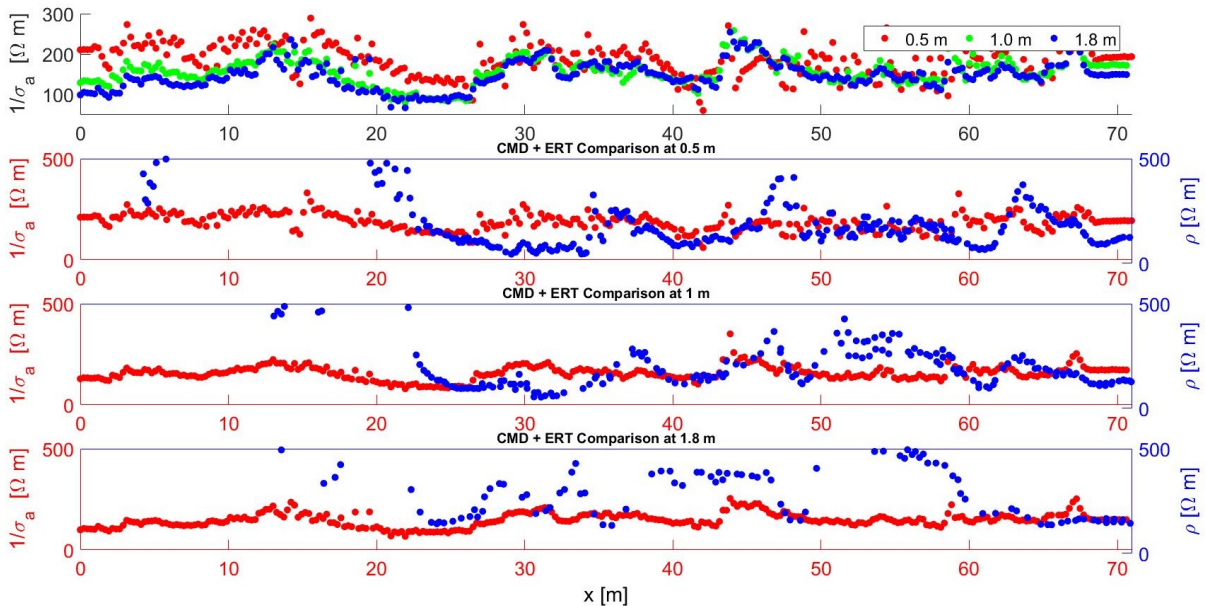


Figure 31: Like figure 29, but for profile 3.

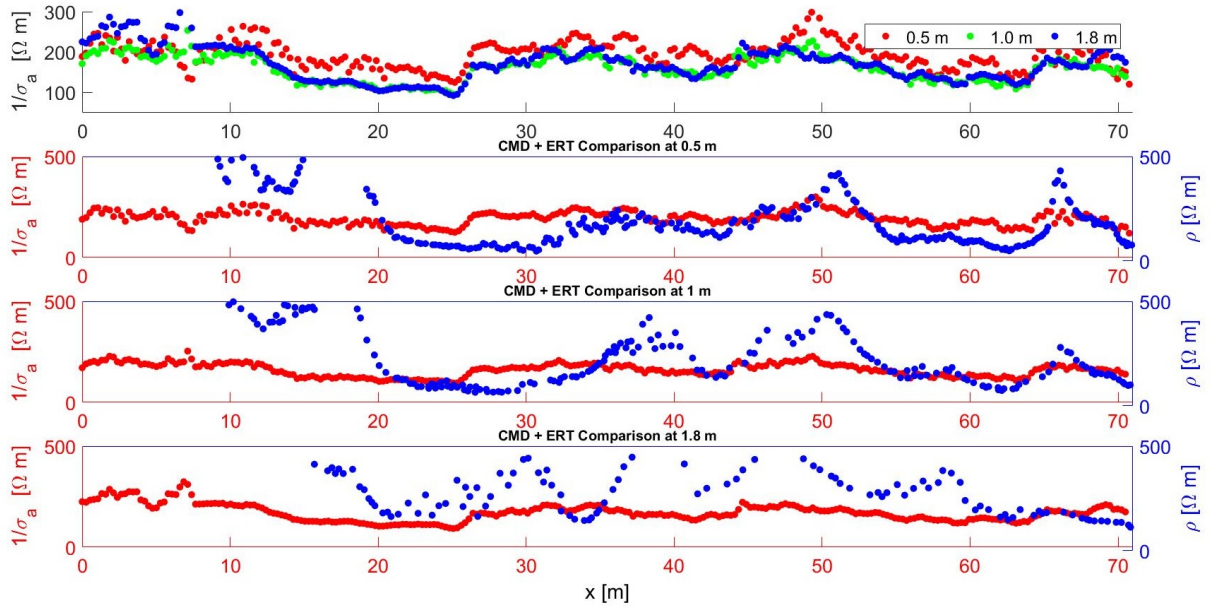


Figure 32: Like figure 29, but for profile 4.

4. **Profile 4:** Figure 32 (first row) shows the resistivity values obtained with the CMD measurement for depths of 0.5, 1.0 and 1.8 m. Also profile 4 starts at the base of the former quarry, however, shows no increased near-surface resistivity at the beginning of the profile. At the beginning of the profile, however, the cut at 1.8 m depth shows an increased resistivity. At meter 10 the two deeper cuts (1.0 and 1.8 m) behave very similar, while the near-surface cut (0.5 m) shows a slightly increased resistivity.
 The second to fourth row of figure 32 show the comparison between the resistivity values determined by means of CMD and ERT. The very high ERT resistivity values at the beginning of the profile can again be explained with poor coupling by loose boulders at the bottom of the rock face. At the near-surface cut (0.5 m), the resistivity values measured with CMD and ERT are similar. In the 1.0 m depth cut, there are larger variations in ERT resistivity, which are still in the same range as the resistivity values of the CMD measurement. Only at a depth of 1.8 m the ERT resistivity values are significantly increased again, but this could also be due to the nearby border to the bedrock (see figure 20, fourth row).
5. **Profile 5:** The CMD measurements in the three depths (figure 33, first row) as well as the comparison between the resistivity values determined with CMD and ERT (figure 33, second to fourth row) behave very similar to the neighbouring profile 4. Since the two profiles were only about 3 m apart from each other, it can be assumed that they reproduce the same underground structures.
6. **Profile 6:** In figure 34 (first row) the CMD resistivity values for depths of 0.5, 1.0 and 1.8 m are shown. The first 10 meters of the profile show high resistivity values in all three sections. Profile 6 starts with a large pile of loose stones, which is already covered with some sediment, but may still explain the increased resistivity values. From meter 10 on, the two deeper cuts (at 1.0 and 1.8 m depth) again show a very similar behaviour and

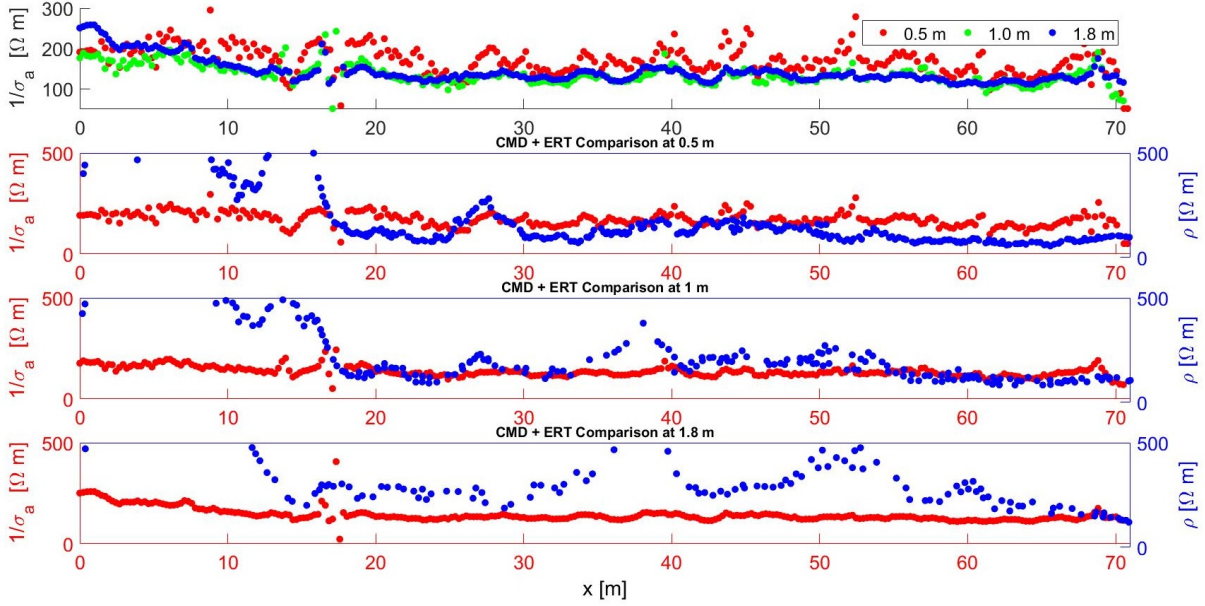


Figure 33: Like figure 29, but for profile 5.

always remain in a resistivity value range typical for soil. As with most other profiles, the near-surface cut (at 0.5 m) shows a slight increase in resistivity values.

Figure 34 (second to fourth row) show the comparison between the resistivity values determined with CMD and with ERT. At the beginning of the profile, the ERT resistivity values show an even larger increase than the CMD resistivity values. The near-surface section (0.5 m) then shows a fairly good agreement between the resistivity values determined with CMD and ERT. The section at 1.0 m depth also shows quite good agreement, apart from a few fluctuations in the ERT resistivity values. At the deepest cut in 1.8 m, the ERT resistivity values are clearly increased again, which, however, could also be because of the near border to the bedrock (see figure 23, second row). From meter 50 on, the two resistivity values are in good agreement again, which also matches well with the here downwelling bedrock.

7. **Profile 7:** Like at the profiles 4 and 5 the CMD measurements (figure 35, first row), as well as the comparison between resistivity values determined with CMD and ERT (figure 35, second to fourth row) show a quite similar behaviour for the two neighbouring profiles 6 and 7. Since the two profiles are again only 3 m apart and also run along the two edges of the same forest road, one can assume that they exhibit the same underground structures. This is also evident from the great similarity between the two ERT images (figure 23, second and third row).

4.3.4 GPR

Above the Forststräßeneinbruch measurements were made with a 200 MHz ($\lambda = 0.6$ m, medium limestone) and an 80 MHz ($\lambda = 1.5$ m, medium limestone) antenna. This results in a vertical resolution ($\approx \lambda/2$) of about 0.3 m and 0.75 m, respectively. The horizontal resolution decreases with increasing distance to the antenna and is defined by the first Fresnel zone. With the 80

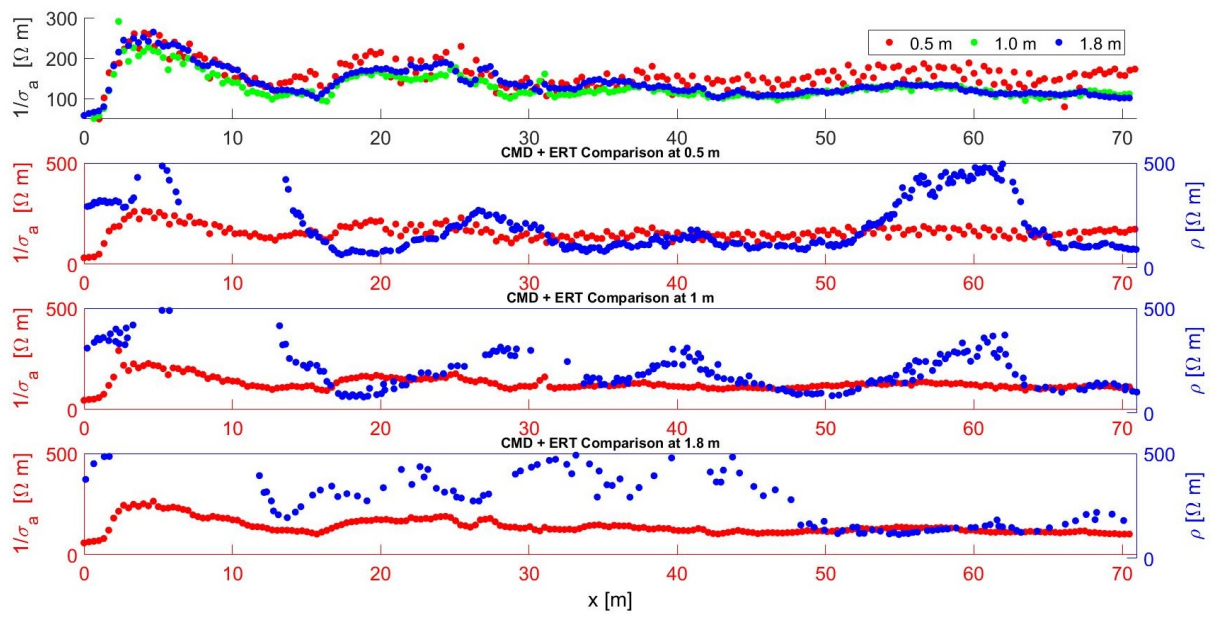


Figure 34: Like figure 29, but for profile 6.

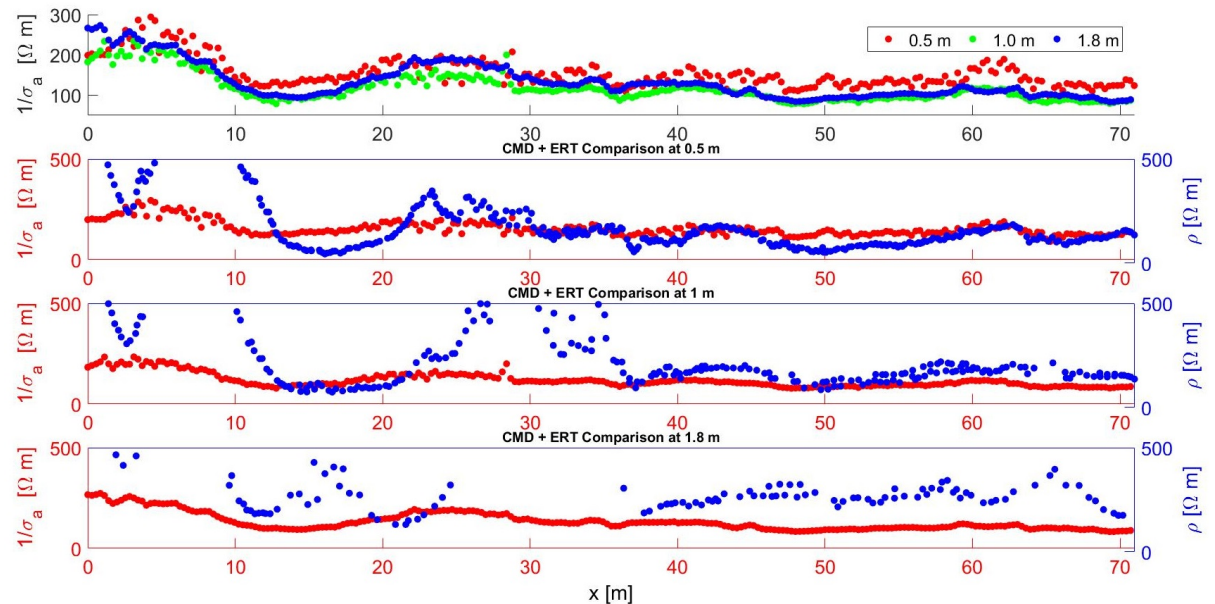


Figure 35: Like figure 29, but for profile 7.

MHz antenna one can achieve a horizontal resolution of about 3.9 m at a depth of 5 m, but only of 7.8 m in a depth of 20 m. The 200 MHz antenna achieves a horizontal resolution of approximately 2.5 m at a depth of 5 m and a resolution of 3.5 m at a depth of 10 m.

The quite narrow corridors of the Forststraßeneinbruch are located at depths between about 3 m and 20 m. So it was already suspected that a detection by GPR will be possible only in a few cases, since the 200 MHz antenna may indeed have the necessary resolution, but can hardly reach most cavities due to the maximum penetration depth of about 10 m. The 80 MHz antenna achieves the necessary depth, but with an increasingly poor resolution, which also means that only a few larger rooms could be recognizable.

In fact, the evaluation showed that the cavities of the Forststraßeneinbruch can not be seen on any of the radargrams of the 200 MHz antenna. On the radargrams of the 80 MHz antenna only one cavity could be detected at profile 1. Profile 1 runs over a shaft with a diameter of about 3 m and a depth of 15 m, which is one of the largest spaces in the Forststraßeneinbruch and only has an covering of about 8 m. Profile 1, which was already shown in the paper, thus remains the only profile in which a cavity could be detected in the radargrams. Thus no further results of the GPR measurements are shown here.

5 How to build electrical models from real data in speleology

In the following the data taken during a cave survey are explained, how they are displayed and which additional information is available (section 5.1). In a next step, electrical models are created from the survey data and are compared with the images of the ERT measurements (section 5.2).

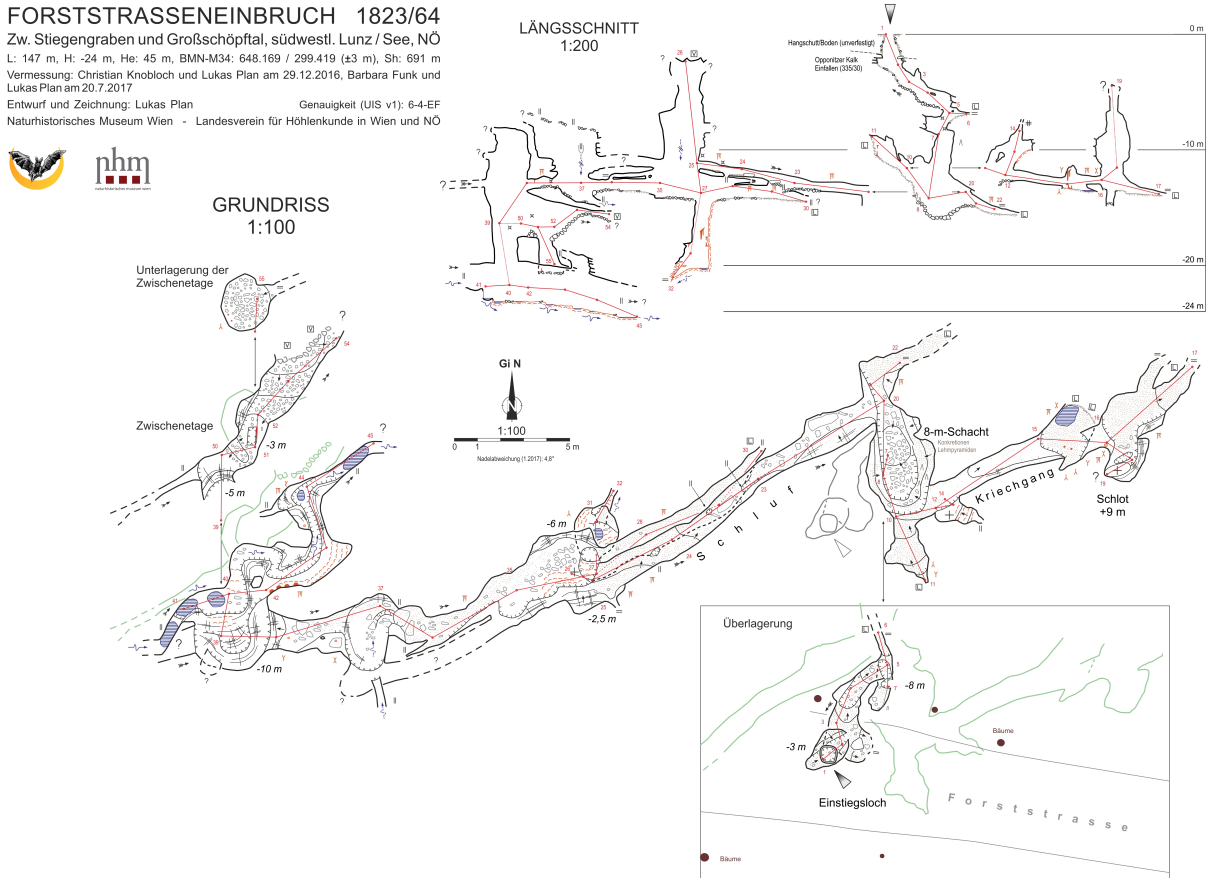


Figure 36: Plan of the Forststrasseneinbruch.

5.1 Cave survey

The Forststrasseneinbruch was first reported because of a hole that opened in a forest road in December 2016. The survey was started in December 2016 and was completed for now in July 2017. For surveying, a traverse is laid through the cave by using a distance meter (Leica DistoX), which also provides a compass and an inclinometer. The data is transferred directly to a PDA, on which additional information, such as the extent of the rooms or the composition of the ground is drawn. In order to better determine the room dimensions, splay shots are often added to the traverse. Thus, the traverse and all the splay shots in the form length, azimuth, angle of inclination, as well as the cave plan (see figure 36) were available. To display the traverse and the splay shots, first length and angle were converted into x-, y-, z-coordinates. This results in points that reflect the shape, size and depth of the cave in a local coordinate system with the origin at the cave entrance. All the existing points are shown in Figure 37 in a 3D representation. This database was then used as the basis for creating electrical models. Since

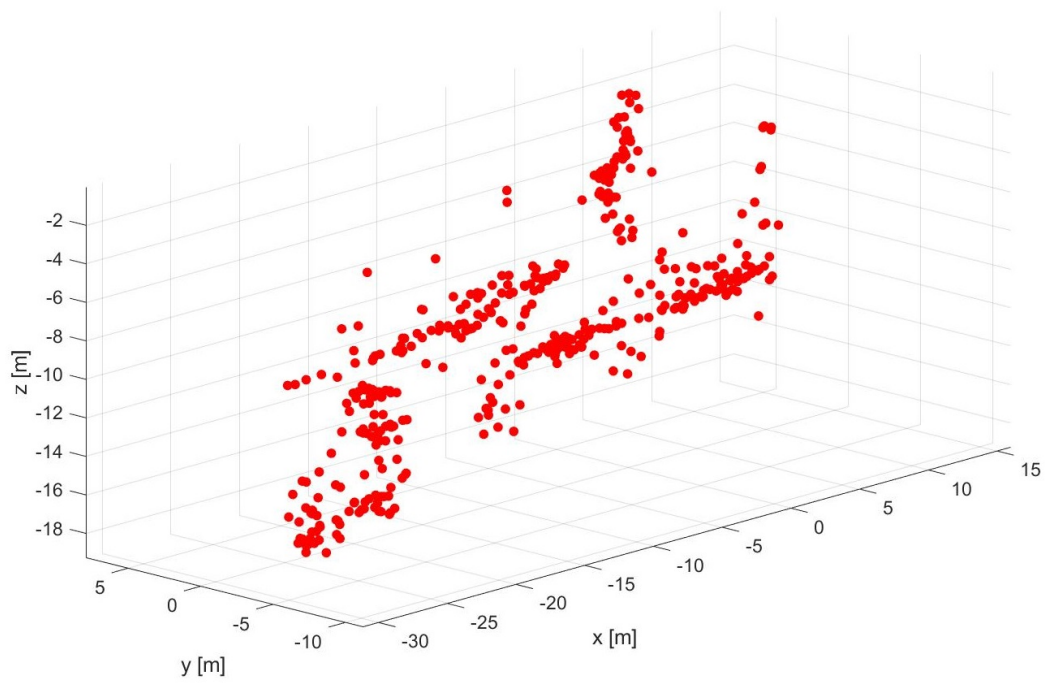


Figure 37: Survey (traverse and splay shots) of the Forststraßeneinbruch (red points).

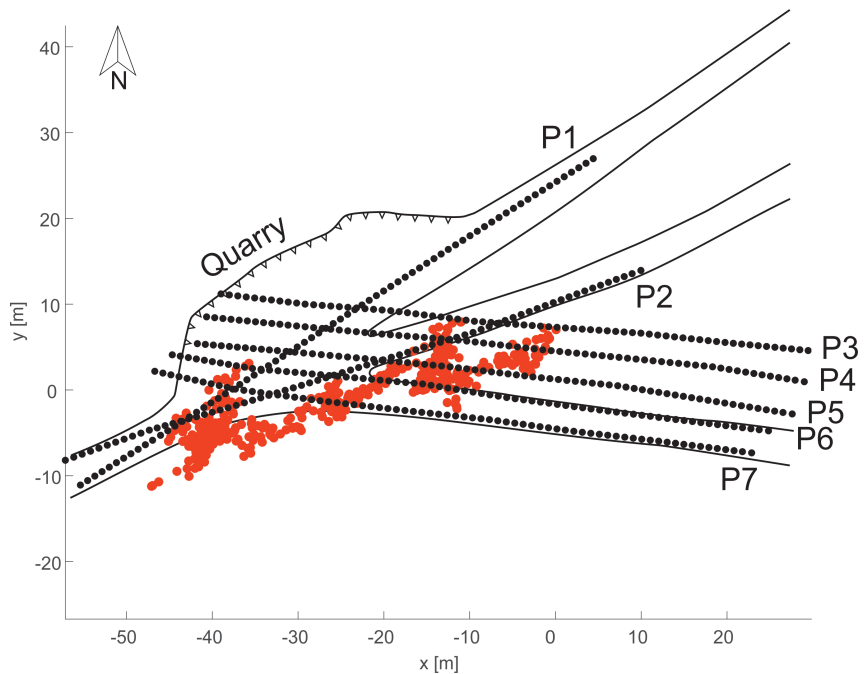


Figure 38: 2D representation of the coordinates from the cave survey (red dots) and the profile coordinates (black dots) in a common local north-facing coordinate system. Also shown are the three forest roads and the quarry in the study area.

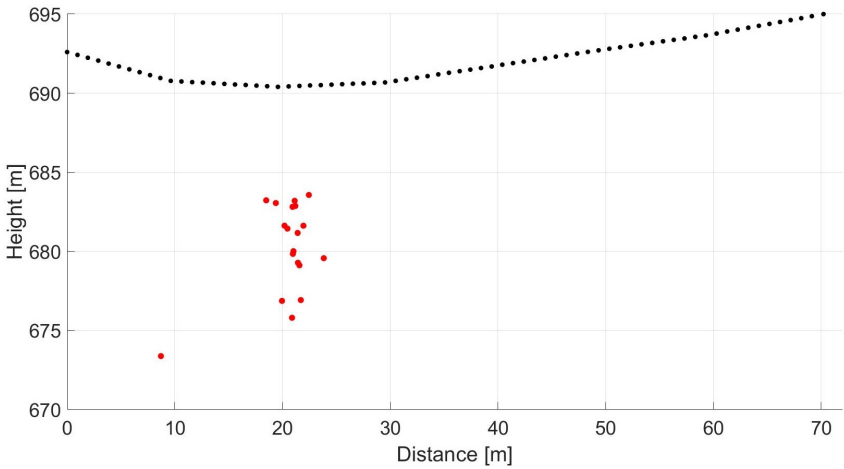


Figure 39: Vertical section below profile 7. Shown are the cave survey points below profile 7 (red dots) and the electrode positions along profile 7 (black dots) in a distance versus height representation.

the results of the model calculations should be compared with the results of the measurements, it was necessary to bring the coordinates of profiles 1-7 and the coordinates of the cave survey into the same coordinate system. Based on the survey method, the cave survey is already in a north-facing local coordinate system, but the survey of the seven profiles are in a randomly stored local coordinate system. Therefore, the profile coordinates were rotated by the rotation angle determined in section 4.3.1. Since the angle is inaccurate, the profiles were additionally aligned to the forest roads digitized from the laser scan. Thereafter, the two coordinate systems were matched according to the known position and height of the profiles relative to the cave entrance. Figure 38 shows the result, which has now been used for further evaluation. In order to create models of the subsurface, vertical sections were calculated for all seven profiles and thus the position and the depth of the underlying cave parts were determined. The determined x and y coordinates were finally converted at distances to the first electrode, since the ERT/IP images are only 2D in the form of distance versus height. Figure 39 shows the vertical section below profile 7 as an example. With the help of these sections and the additional information on the extent of the cave chambers known from the cave plan (figure 36), models of the underground for all seven profiles could now be created and compared with the results of the measurements.

5.2 Comparison

As explained in the previous section, models of the subsurface were created below all seven profiles. In each case the same electrode configurations and grid files as for the actual measurements were used. In addition, the models were also superimposed with a data error of 5%, comparable to the error in the actual measurements. The forward modelling was performed with the program CRMod and the inversion with the program CRTomo. In the following, the creation of the models and the comparison with the respective measurements for all profiles are shown.

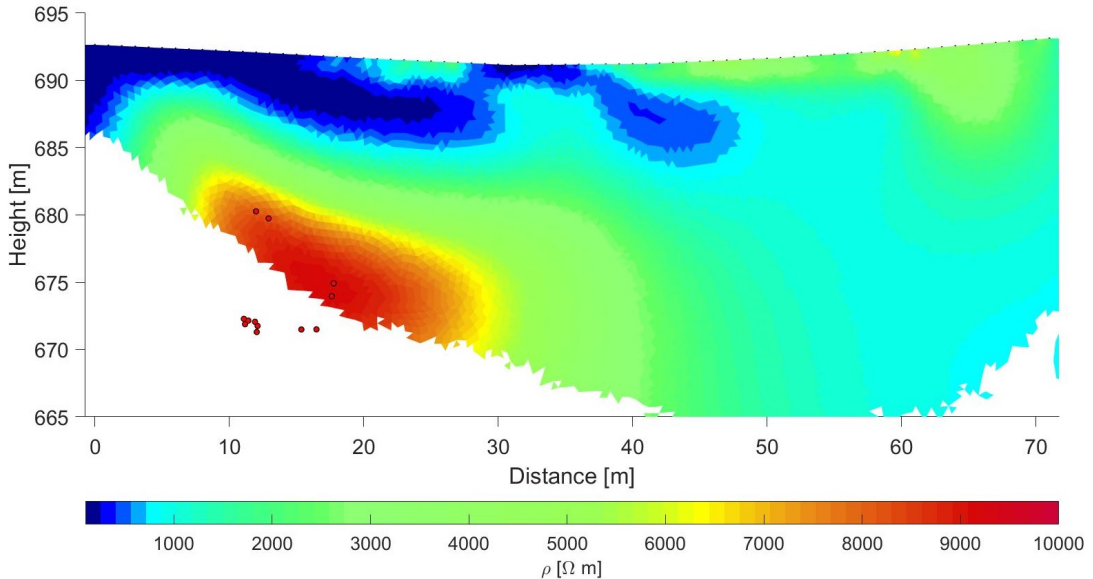


Figure 40: ERT image from profile 1 overlaid with the coordinates taken from the cave survey (red dots).

5.2.1 Profile 1

In a first step, the coordinates of the cave survey were placed over the ERT image to compare the position of the cave with the position of the resistivity anomalies (see figure 40). For profile 1, the well-known position of the cave chambers coincides very well with the position of the resistivity anomaly. Therefore, in a next step a model of the subsurface below profile 1 was created, as described in section 5.1. For this purpose, an air-filled cavity ($\rho = 10^9 \Omega\text{m}$) was assumed within a radius of two meter around the points of the cave survey (figure 40, red dots). The result was compared with the cave plan and, if necessary, the size of the cavities were adjusted. For a first simple model just these cavities and the surrounding limestone with a resistivity of 1000 Ωm was used. Figure 41 shows the model of the subsurface created from the cave survey and cave plan (upper row, left) and the obtained ERT image after inversion (upper row, right). Already this simple model leads to a qualitatively similar result as seen in the ERT image of the measurements, just the soil layer at the beginning of the profile is missing. Even the suspected soil layer is already partially reproduced by this very simple model, which could indicate that there is just a narrow soil layer in the beginning of profile 1. As in section 3.2.3, it is also noticeable that the resistivity values of the cavity after inversion are significantly lower than in the model and are also significantly lower than in the ERT image obtained from the measurements, while the resistivity values of the bedrock are well reproduced. The cave exploration shows a small chute at the bottom of the shaft below profile 1, thus another model has been created by taking this into account. It was assumed that the resistivity at the bottom of the shaft was significantly reduced by water ($\rho = 100 \Omega\text{m}$). The model and the inversion result are shown in figure 41 (bottom row). Comparing the two inversions, they lead to very similar images, but the model including a chute already shows higher resistivity values, even though still significantly lower, than the inversion result of the real measurements. Nevertheless, thin water and clay layers at the boundary between cavities and bedrock, which are difficult to realize in theoretical models,

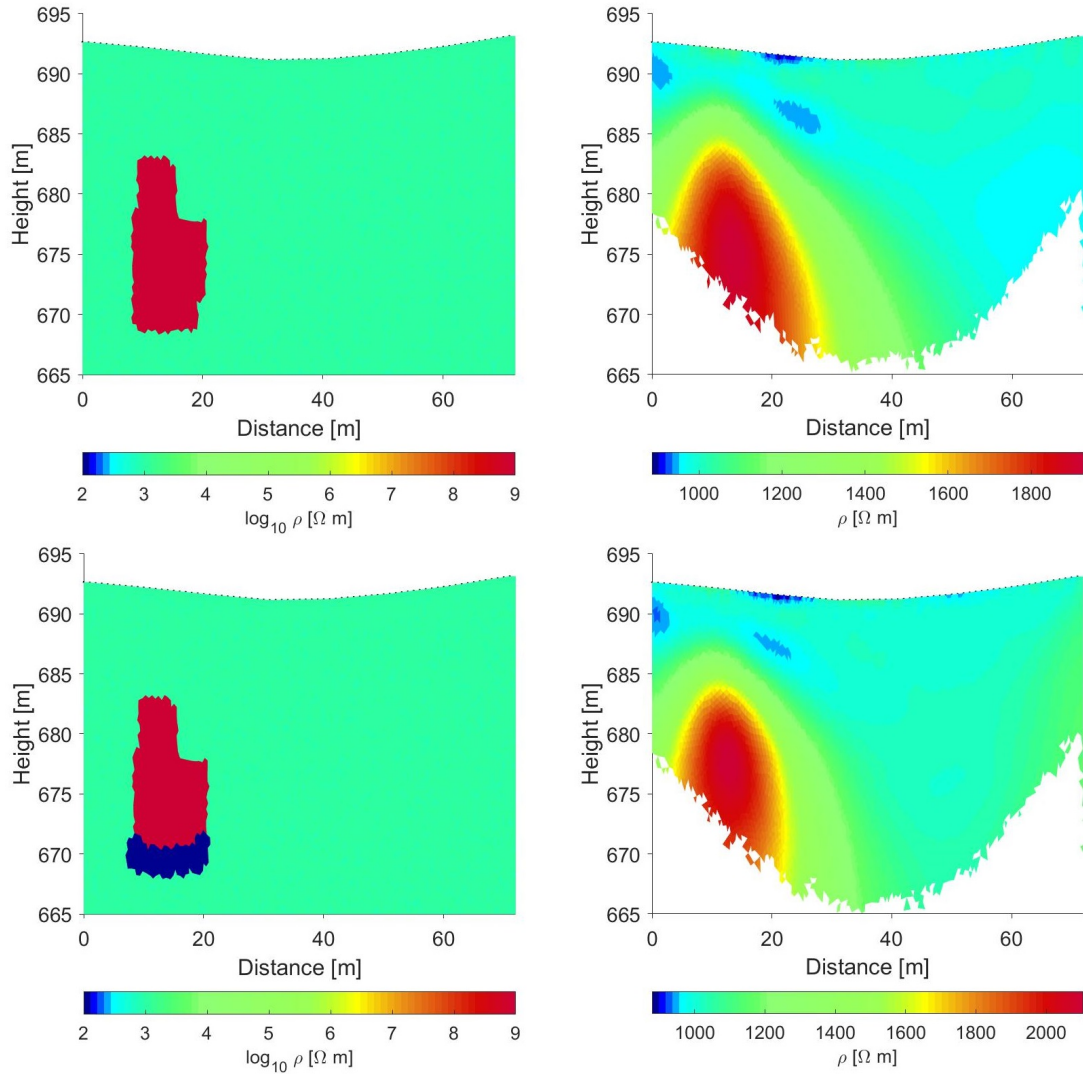


Figure 41: Left: electrical models of the subsurface obtained by using the cave survey points below profile 1 (figure 40, red dots), right: ERT images after inversion. Note that the distance and height axes are not on the same scale.

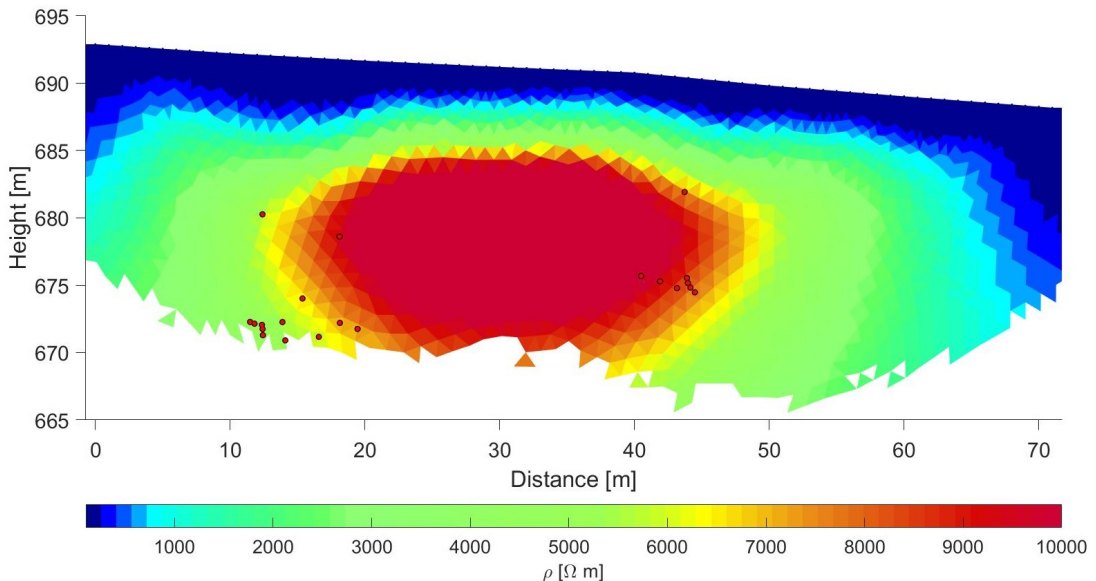


Figure 42: Like figure 40, but for profile 2.

could explain why all real measurements show a significantly higher resistivity contrast than the models.

5.2.2 Profile 2

As for profile 1 the coordinates of the cave survey were placed over the ERT image to compare the position of the cave with the position of the resistivity anomalies (see figure 42). In contrast to profile 1, the known positions of the cave chambers seem not to fit well with the ERT image. Especially in the area in the middle of the profile (between meters 25 and 40) are no cavities according to the cave survey, but the ERT image shows a continuously high resistivity. To investigate possible reasons for this strong deviation, a model of the known cavities was created, using limestone ($\rho = 1000 \Omega\text{m}$) as background, the air-filled cavities ($\rho = 10^9 \Omega\text{m}$) and a soil layer ($\rho = 100 \Omega\text{m}$). Figure 43 shows the model (left) and the ERT image after inversion (right). Although there are similarities, the known caves can not fully explain the ERT image. In particular, the very low resistivity contrast and the significantly lower depth of the anomaly indicate that the known cavities alone are not sufficient to explain the inversion result of profile 2. Therefore, additional models were calculated, which assume the existence of another cavity at meter 30 (figure 43, lower row). The inversion result shows that even a large cavity can not completely explain the ERT image of profile 2, since it still does not reach the same depth. In addition, it is unlikely that another cavity of this size is located below profile 2. Therefore, it seems also possible that problems appear during the measurements or the inversion of the data.

5.2.3 Profile 3

In a first step the coordinates of the cave survey were placed over the ERT image to compare the position of the cave with the position of the resistivity anomalies (see figure 44). Similar to profile 2, the known positions of the cave chambers seem not to fit well with the ERT image. The cave plan (figure 36) shows that profile 3 is located over two quite deep and narrow passages of the

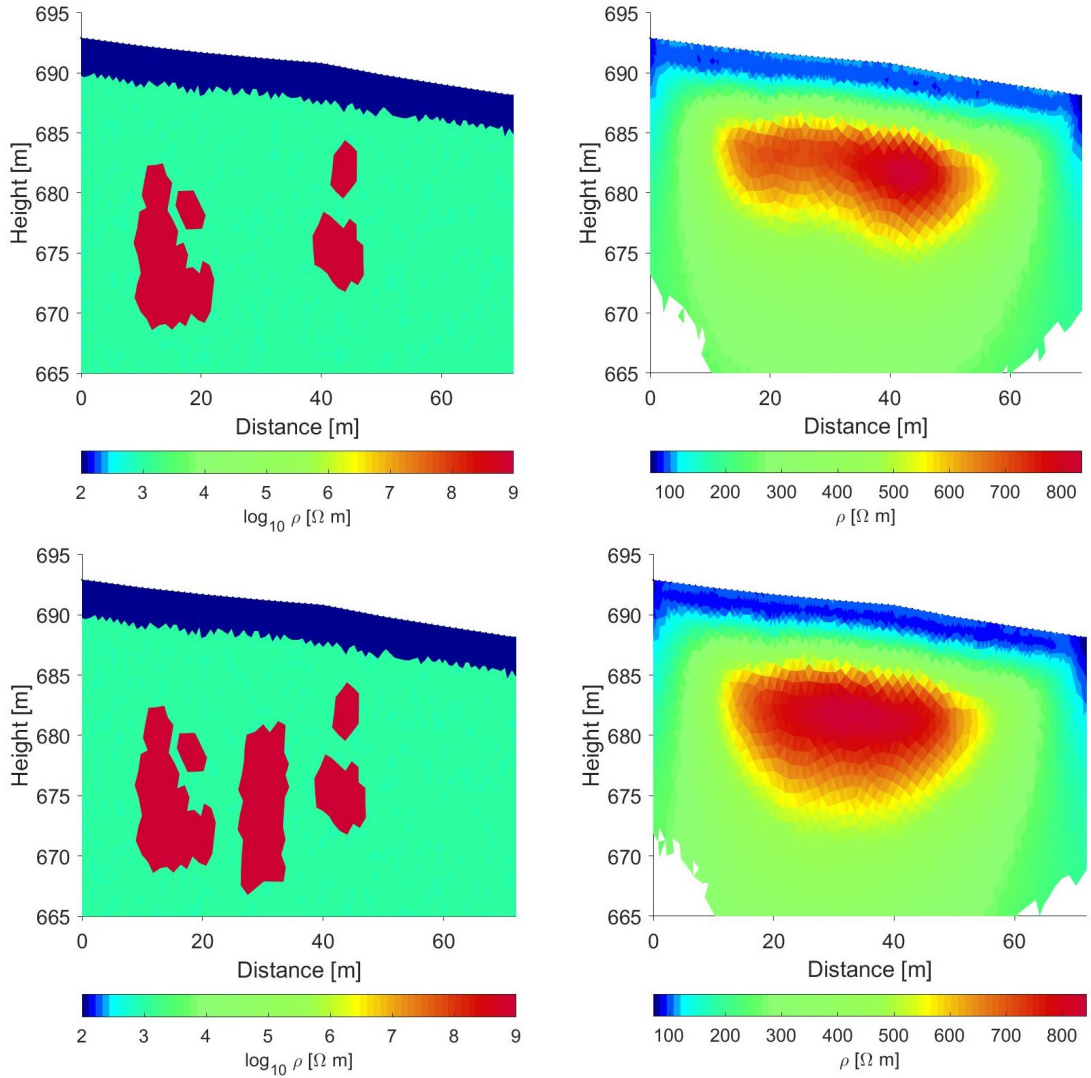


Figure 43: Left: electrical models of the subsurface obtained by using the cave survey points below profile 2 (upper row) and by assuming an additional cavity (lower row), right: ERT images after inversion.

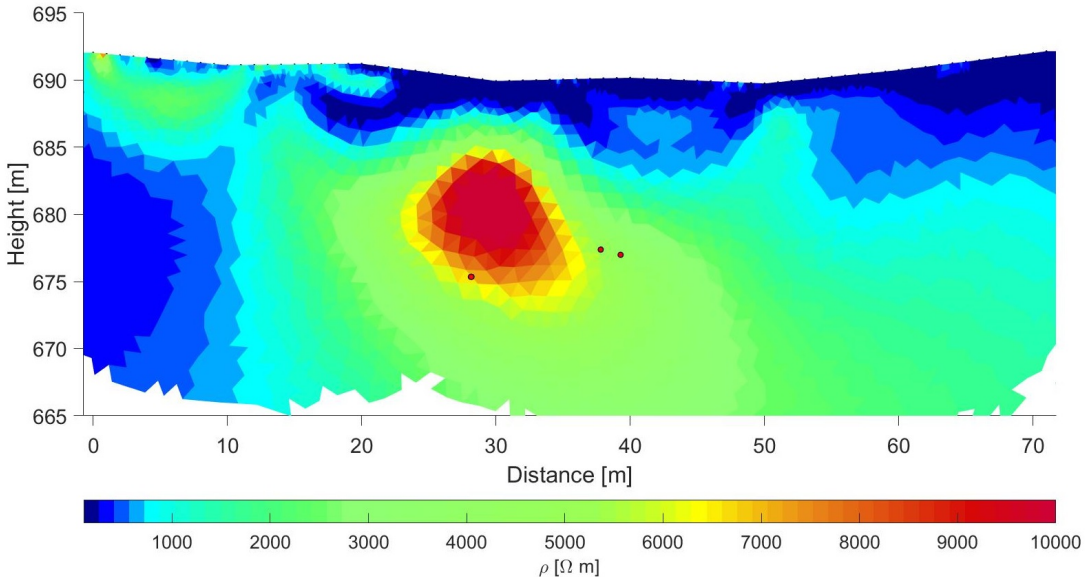


Figure 44: Like figure 40, but for profile 3.

known cave. Therefore, it seems unlikely that the very clearly visible anomaly in the ERT image is produced just by these two narrow passages. To investigate the effect of the known cave parts, a model based on the known cave parts, the surrounding bedrock and a soil layer was created. Figure 45 (upper row) shows the model (left) and the ERT image after inversion (right). As expected, the anomaly visible in the ERT image of the measurements could not be reproduced using just a model of the known cave parts. For the ERT images, inverted for different skip levels, it has been shown that the causative anomaly must be at a height of about 680 m (see figure 24), which is above the known cave parts. Therefore, in a next step, a model including an additional air-filled cavity with a diameter of 2 m was created at this height. Figure 45 (second row) shows the model (left) and the ERT image (right) after inversion. By including another unknown cavity, the ERT image from the measurements could be reasonably reproduced. As a result, it seems likely that there could be a relatively large cavity between a height of 680 and 685 m at about meter 30 of profile 3. This cavity is probably about 5 m below the surface and should therefore not represent a serious danger for the overlying forest road.

5.2.4 Profile 4

Also for profile 4 the coordinates of the cave survey were placed over the ERT image to compare the position of the cave with the position of the resistivity anomalies (see figure 46). Whereas the cave chambers around meter 25 coincide quite well with the resistivity anomaly, the cave rooms around meter 35 are not visible in the ERT image. In a next step, a model of the subsurface below profile 4 was created to investigate the influence of the known cave parts. Figure 47 shows the model (left) of the underground based on the cave survey and cave map below profile 4, again assuming an air-filled cavity in limestone and a soil layer. Even this quite simple model leads to a similar ERT image, as resulting in the inversion of the measured data. In profile 4, therefore, the ERT image can be reproduced with the known cavities. Thus, the assumption that profiles 3 and 4 show the same cavity is probably wrong, since no further void is needed to explain the

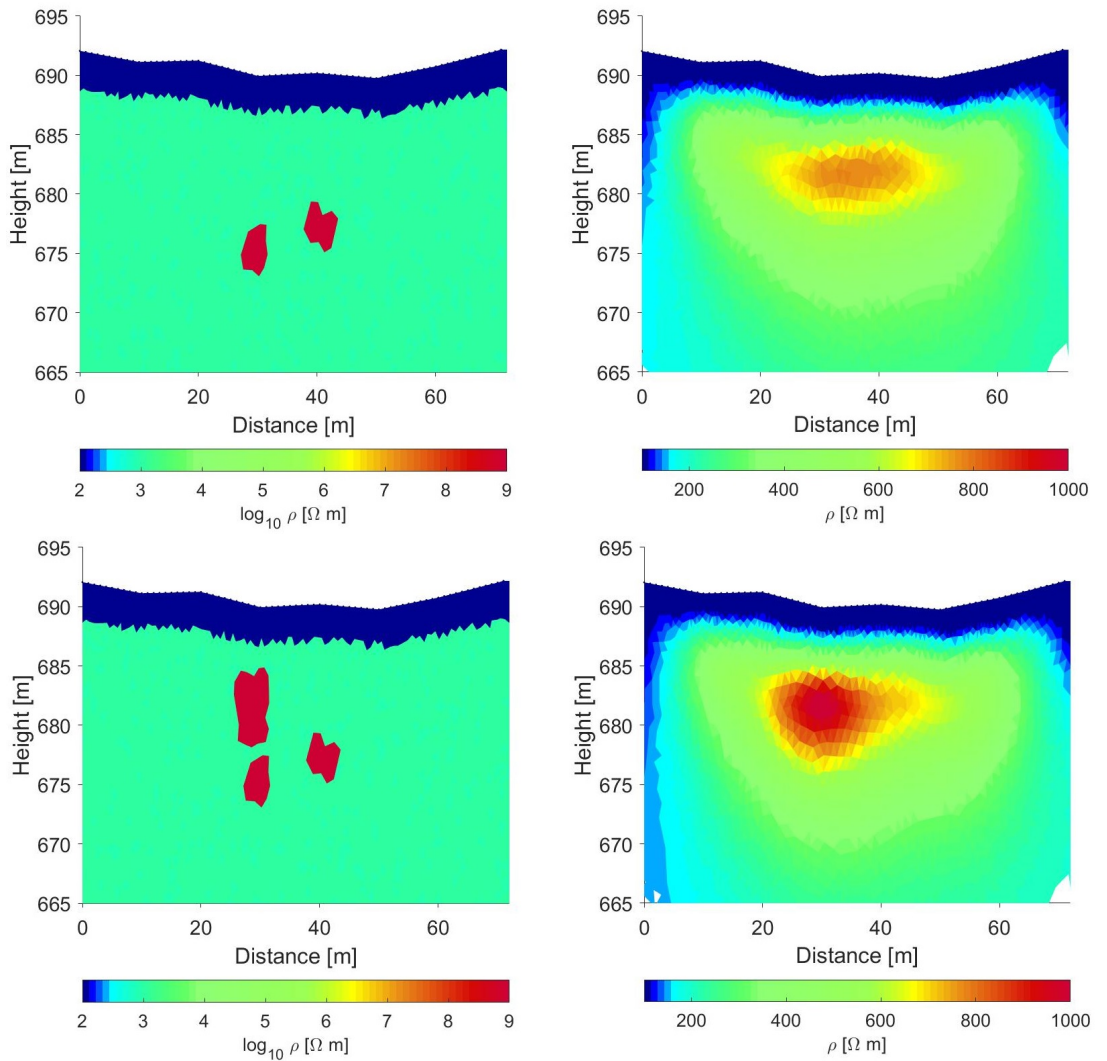


Figure 45: Left: electrical models of the subsurface, right: ERT images after inversion. First row: model obtained by using the cave survey points below profile 3 (figure 44, red dots). Second row: like first row, but by assuming an additional cavity.

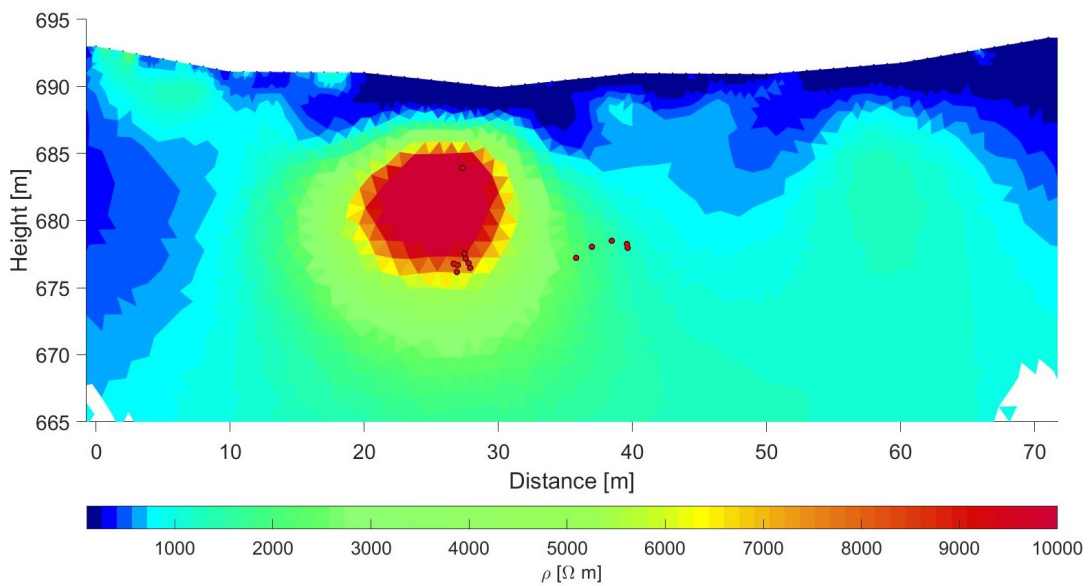


Figure 46: Like figure 40, but for profile 4.

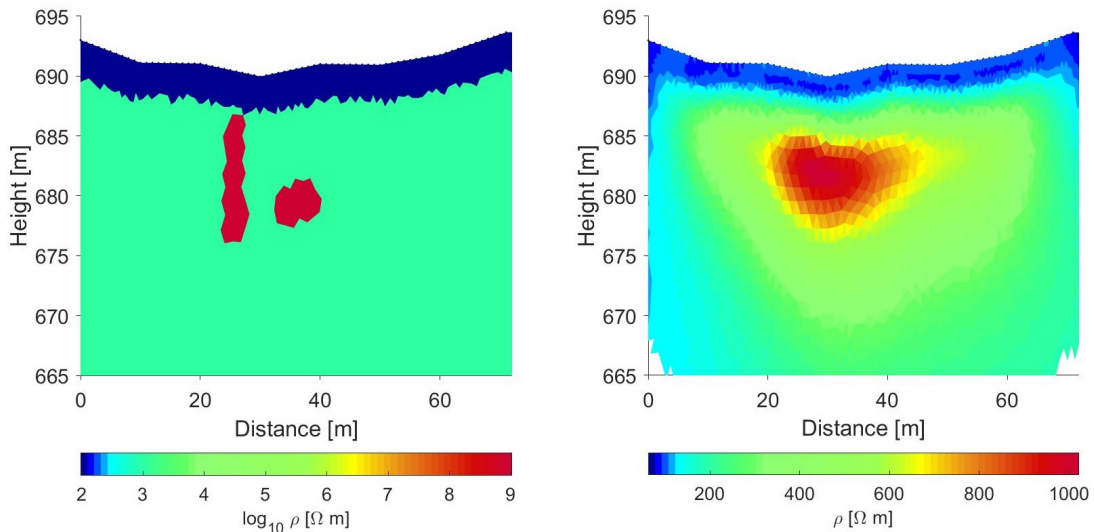


Figure 47: Electrical model of the subsurface below profile 4 (left) and ERT image after inversion (right).

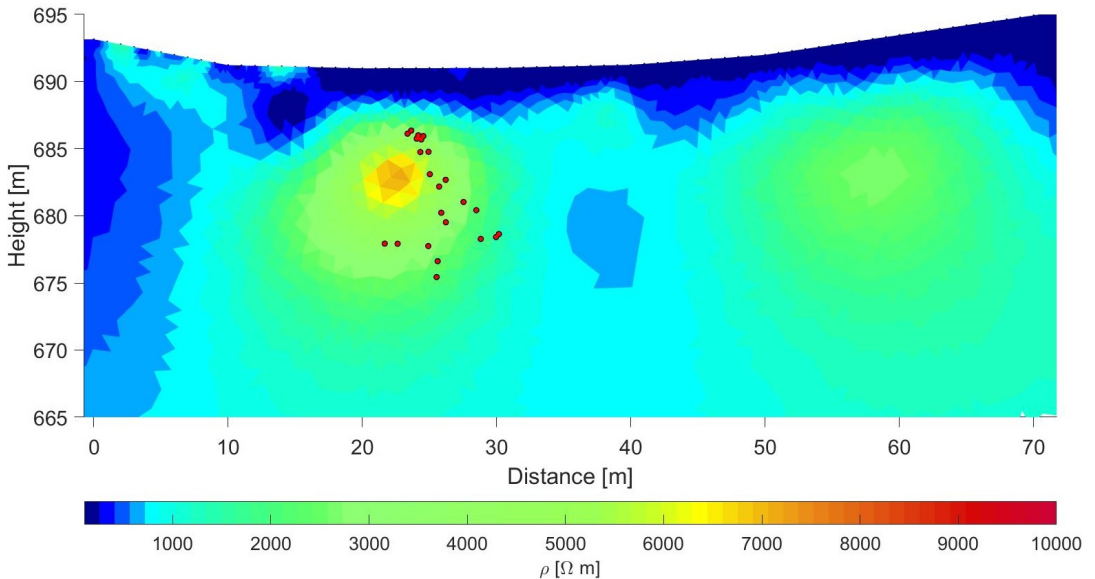


Figure 48: Like figure 40, but for profile 5.

ERT image of profile 4. Below profile 3, there could actually be another, yet unknown cave room.

5.2.5 Profile 5

In a first step, again the coordinates of the cave survey were placed over the ERT image to compare the position of the cave with the position of the resistivity anomalies (see figure 48). For profile 5, the ERT image seems not to fit well with the cave survey data. However, in comparison with the cave plan, the areas below profile 5 are mostly narrow passages. In addition, the cave walls in this region are covered with clay and sediment, which could also increase the conductivity. Again, a simple model (limestone, air and soil layer) was created to compare the ERT image of the known caverns with the ERT image of the measurements. Figure 49 shows the model (left) and the ERT image after inversion (right). The ERT image after inversion of the model is quite similar to the image after inversion of the measured data. Therefore, it can be assumed that the relatively narrow and rapidly deepening corridors under profile 5 appear only partially in the ERT images. In any case, the modelling fits quite well with the ERT image of the actual measurements. Thus, the high resistivity anomaly seen in figure 48 can be explained by the known cavities.

5.2.6 Profile 6

Again the coordinates of the cave survey were placed over the ERT image. Since the inversion of the data for profile 6 (figure 23, left column, second row) does not show any anomalies with high resistivity, it was interesting to find out if there are any known cavities below profile 6. Figure 50 shows the overlay of the ERT image and the known cave chambers for profile 6. Based on the figure one can conclude that there are some cavities below profile 6, but they are very small-scale cave parts. In addition, since most of the cave rooms are located quite deep, this could explain the lack of a prominent anomaly with high resistivity. To check this assumption, a model of the subsurface (limestone, cave parts and soil layer) was created here as well. Figure

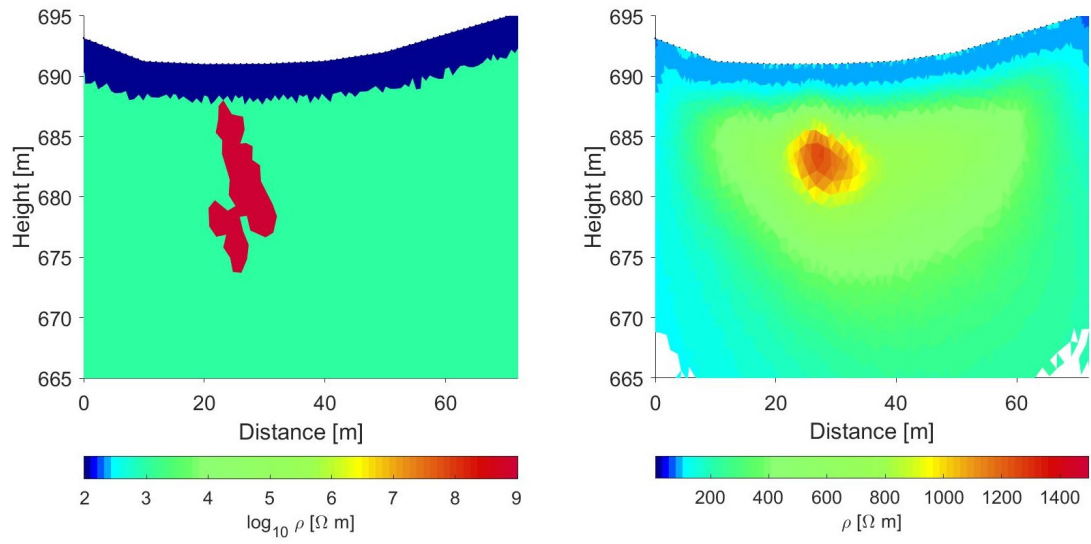


Figure 49: Electrical model of the subsurface below profile 5 (left) and ERT image after inversion (right).

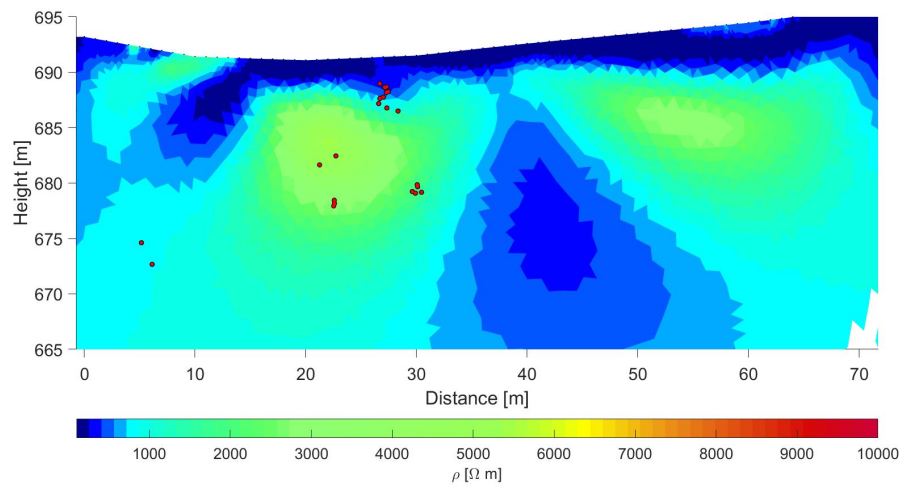


Figure 50: Like figure 40, but for profile 6.

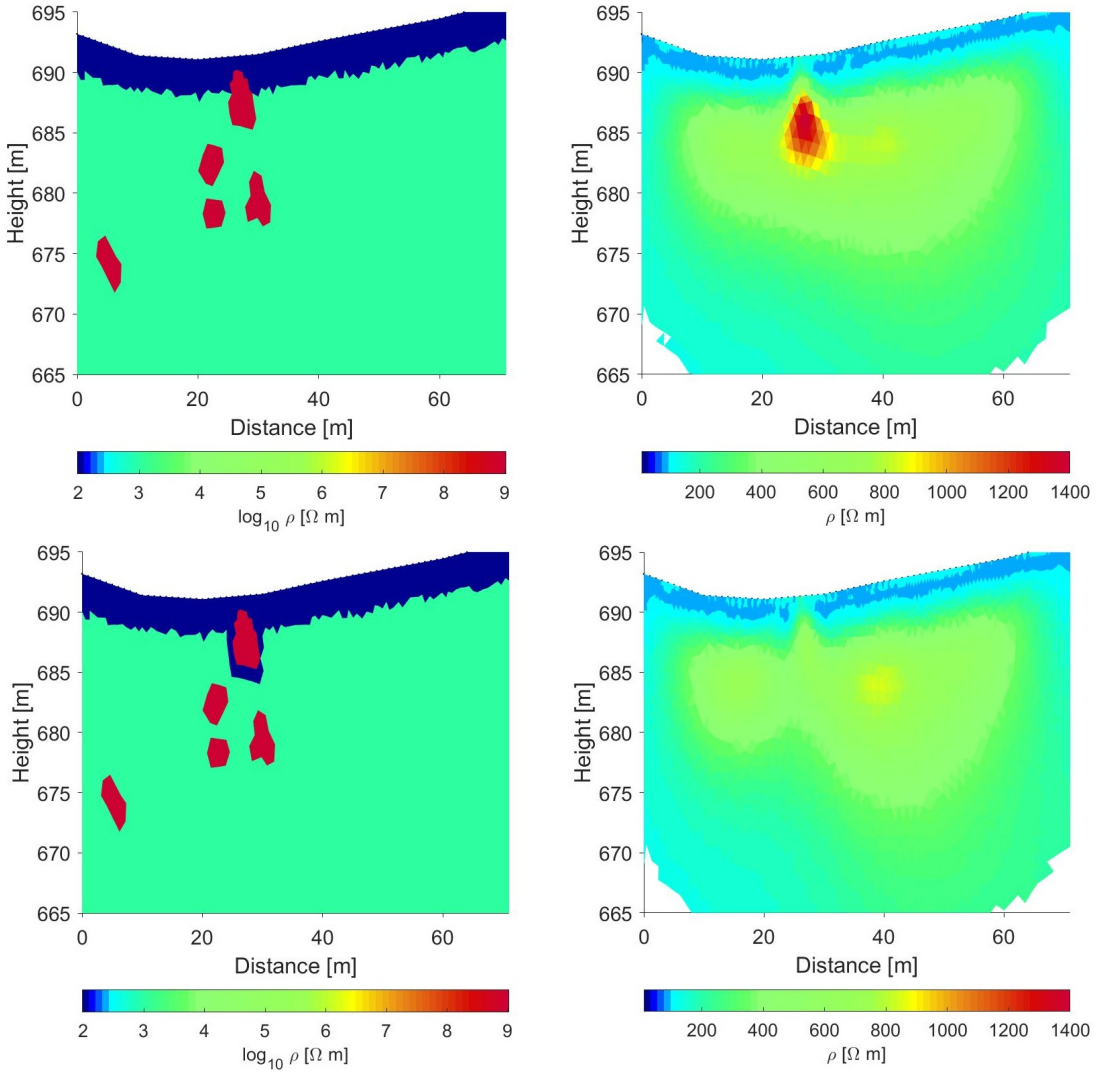


Figure 51: Electrical model of the subsurface below profile 6 (left) and ERT image after inversion (right). Upper row without and lower row with a conductive layer on the cave walls of the surface-near cave parts.

51 (upper row) shows the model (left) and the ERT image after inversion (right). As expected, all deeper parts of the cave are not visible in the ERT image, but the cavity close to the surface can be clearly seen. However, as it is known from the cave plan and the cave exploration, the walls of this near-surface cave part are completely covered with sediment and clay, leading to a significant increase in conductivity. Therefore, a second model was created to take this into account. Figure 51 (lower row) shows the model (left) and the ERT image after the inversion (right). Actually none of the cavities are visible any more. Thus, it was shown that the cavities below profile 6 are probably too small and mostly too deep to be resolved.

5.2.7 Profile 7

Like for profile 6, the inversion of the data for profile 7 (figure 23, left column, third row) shows no anomalies with significantly increased resistivity. Only between meters 15 and 20 at a height of about 685 m a slight increase in resistivity can be detected. To check if there are any known

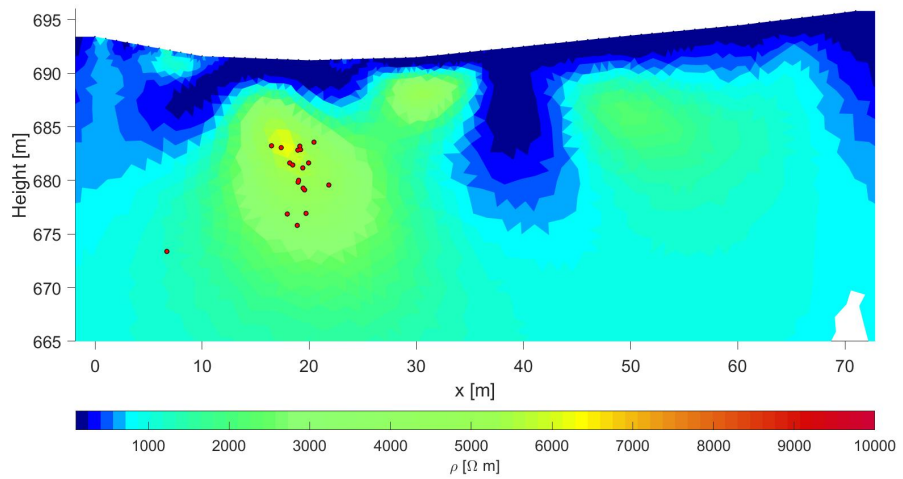


Figure 52: Like figure 40, but for profile 7.

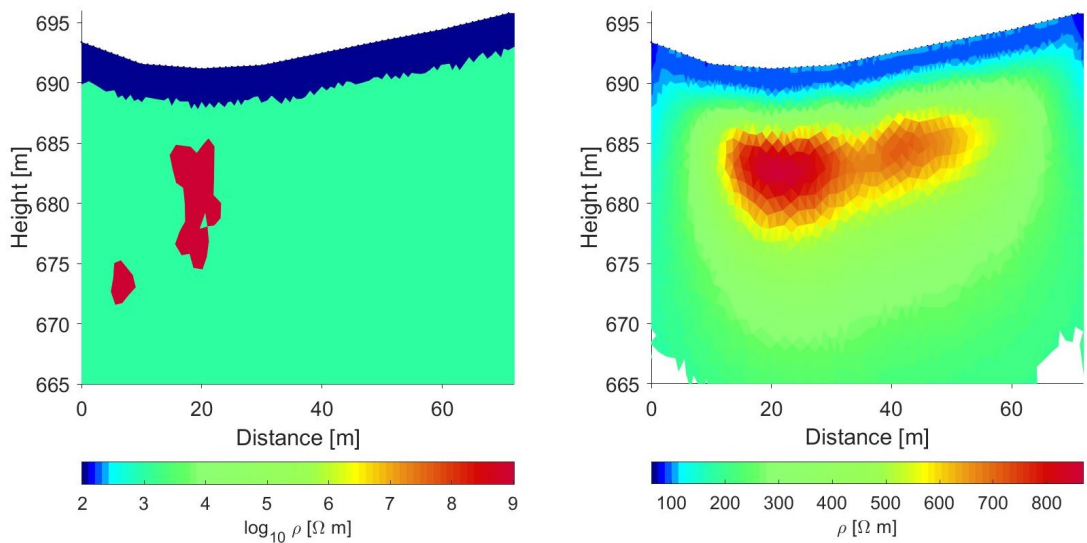


Figure 53: Electrical model of the subsurface below profile 7 (left) and ERT image after inversion (right).

cave parts below profile 7, the coordinates of the cave survey were placed over the ERT image. Figure 52 shows the comparison for profile 7. The overlay shows that there are known parts of the Forststraßeneinbruch below profile 7. Whereas the small cavity between meters 5 and 10 is probably too small and too deep to be resolved, it is surprising that the cavity between meters 15 and 20, which is significantly larger and closer to the surface, is not clearly displayed in the ERT image. To check the appearance of the known cavities in the ERT image, a model of the subsurface, consisting of limestone, cavities and the soil layer, was created and inverted. Figure 53 shows the model (left) and the ERT image after inversion (right). The result of the modelling shows that the small, deep cavity does actually not show up, but also the larger, near-surface cavity is hardly resolved. Although there is a noticeable increase in resistivity at meter 20, it covers almost the entire profile and only reaches very low values in absolute terms. Probably, this poor resolution could be due to the soil layer, where most of the current already flows near the surface in this well-conductive layer. Thus, a cavity in anyway poorly conductive limestone is barely resolvable.

6 Summary and outlook

In the present work, the possibilities to detect karst systems (in particular cavities filled with water or air) by means of electrical methods (ERT, IP) were investigated by combining models and measurements. In the theoretical modelling part, a linear relationship was found between the size of a cavity and the maximum depth at which this cavity is detectable. Moreover, it was also shown that the resolution of a more complicated geometry is not possible. In the theoretical part it was shown that the existence of a well-conducting near-surface layer (e.g. soil layer) significantly increases the just detectable size of a cavity. One can assume that large parts of the current directly flows into the well-conducting, near-surface layer. Thus, a cavity in the already poorly conductive limestone can no longer be recognized. Problems like this also became apparent later in the real measurements and their modelling.

The second part of this thesis deals with geophysical surveys above two known caves (Stiegen-graben Wasserhöhle and Forststraßeneinbruch), where the buried entrance of Stiegengraben Wasserhöhle could be recognized on the radargramms and ERT-images of the geophysical measurements. A more detailed description of the measurements and results can be found in the paper presented in section 4.1. The second survey area was above the Forststraßeneinbruch, where measurements using GPR, CMD and ERT/IP were obtained. With one exception, it was not possible to detect the known rooms of the Forststraßeneinbruch on the GPR measurements, since the cavities are too deep and/or too narrow to be resolvable by GPR. A much better result was obtained with the ERT measurements, where almost all underlying cavities are recognizable. In order to determine whether the high resistivity anomalies that are visible in the ERT images are actually caused by the known cavities, further modelling was carried out.

For this purpose, the coordinates of the profiles and those of the cave survey were transformed to the same coordinate system and superimposed. Afterwards sections through the cave survey below the profiles were calculated to accurately determine the position of the known cave rooms. The modelling of the known cave parts resulted in a quite good match or reproducibility of the measurements for the profiles 1 and 4 to 7. However, for two profiles (P2 and P3) there are clear deviations between the measurements and the modelling results. In these two profiles the known cavities are not sufficient to explain the occurring anomalies with high resistivity. Figure 54 shows the contour of the Forststraßeneinbruch, the positions of all seven profiles, and the areas where additional voids might be expected. More geophysical measurements and a continuation of the cave survey are essential to conclude if there are indeed additional larger cavities or if the anomalies are caused by other effects.

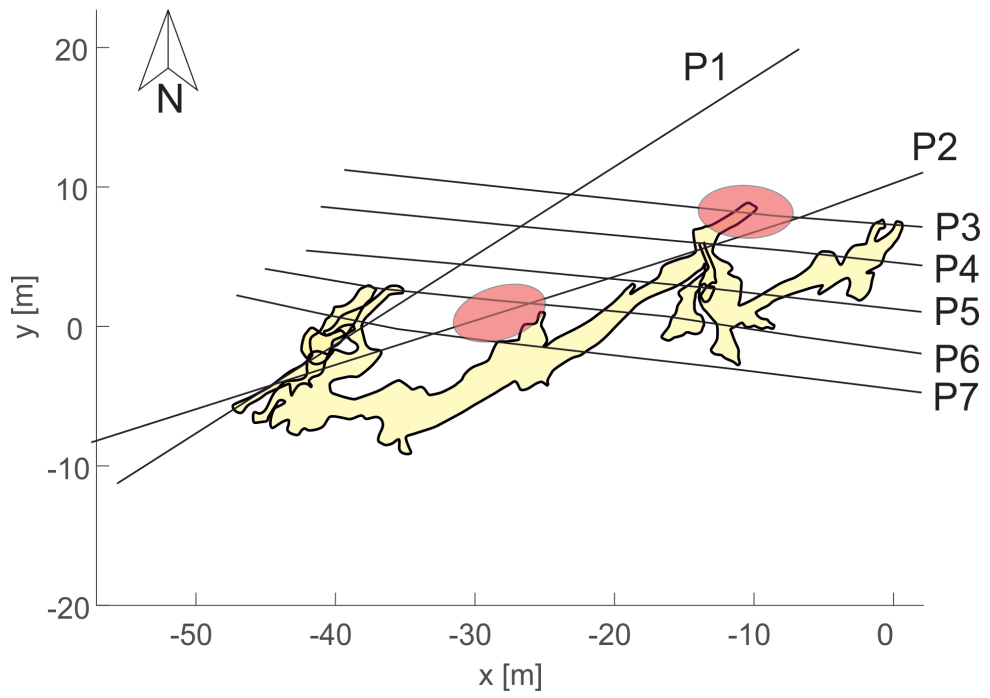


Figure 54: Contour of the Forststraßeneinbruch with the positions of all seven profiles. The red ellipses indicate the areas in which additional voids might be present.

7 Acknowledgement

At this point, I would like to thank everyone who supported me in writing the master thesis. Especially I would like to thank my supervisor Adrian Flores-Orozco for assistance and support during the whole process.

I also would like to thank all the members of the Geophysics Research Group, who were always ready to help me with various issues. Special thanks goes to Michael Behm, Werner Chwatal, Antonia Golab, Theresa Maierhofer and Anibal David Marquina Cisneros, for their help with the recording and evaluation of the geophysical data, as well as to Lukas Plan for the help in geological and speleological topics and for providing the data of the cave survey and the cave plan.

Special thanks also goes to Martin for his support during the entire study and for proofreading the master thesis.

References

- Archie, G.E., 1942: The electrical resistivity log as an aid in determining some reservoir characteristics. *Transactions of the AIME*, 146(1), 54–62.
- Binley, A., Kemna, A., 2005: DC resistivity and induced polarization methods. *Hydrogeophysics* (ed. Y. Rubin and S. Hubbard), Netherlands: Springer, 129–156.
- Butler, D.K., 2005: Near-surface geophysics. Society of Exploration Geophysicists.
- Carrière, S.D., Chalikakis, K., Sénéchal, G., Danquigny, C., Emblanch, C., 2013: Combining electrical resistivity tomography and ground penetrating radar to study geological structuring of karst unsaturated zone. *Journal of Applied Geophysics*, 94, 31–41.
- Carrière, S.D., Chalikakis, K., Danquigny, C., Clement, R., Emblanch, C., 2015: Feasibility and limits of electrical resistivity tomography to monitor water infiltration through karst medium during a rainy event. *Hydrogeological and Environmental Investigations in Karst Systems* (pp. 45–55). Springer, Berlin, Heidelberg.
- Chalikakis, K., Plagnes, V., Guerin, R., Valois, R., Bosch, F.P., 2011: Contribution of geophysical methods to karst-system exploration: an overview. *Hydrogeology Journal*, 19, no. 6, 1169.
- Deceuster, J., Chambers, J.E., Goderniaux, P., Kuras, O., Wilkinson, P.B., Kaufmann, O., 2013: Management of Sinkhole Risks Using Long Term ERT Monitoring-A Laboratory Experiment. *Near Surface Geoscience 2013-19th EAGE European Meeting of Environmental and Engineering Geophysics*.
- Delle Rose, M., Leucci, G., 2010: Towards an integrated approach for characterization of sinkhole hazards in urban environments: the unstable coastal site of Casalabate, Lecce, Italy. *Journal of Geophysics and Engineering*, 7(2), 143.
- Everett, M.E., 2013: Near-surface applied geophysics. Cambridge University Press.
- Fairchild, I.J., Baker, A., 2012: Speleothem Science: From Process to Past Environments. Chichester (Wiley Blackwell).
- Flores Orozco, A., Kemna, A., Zimmermann, E., 2012: Data error quantification in spectral induced polarization imaging. *Geophysics*, 77, E227–E237.
- Friedel, S., 2003: Resolution, stability and efficiency of resistivity tomography estimated from a generalized inverse approach. *Geophysics Journal International*, 153, 305–316.
- Funk, B., Flores Orozco, A., Maierhofer, T., Plan, L., 2018: Detection of two caves near Lunz am See (Lower Austria) using geophysical methods. *Die Höhle*, 69, 109–117.
- Gómez-Ortiz, D., Martín-Crespo, T., 2012: Assessing the risk of subsidence of a sinkhole collapse using ground penetrating radar and electrical resistivity tomography. *Engineering Geology*, 149, 1–12.
- Keller, G.V., Frischknecht, F.C., 1966: Electrical methods in geophysical prospecting. Oxford : Pergamon Press.

Kemna, A., 2000: Tomographic inversion of complex resistivity — Theory and application. Ph.D. thesis, Ruhr University of Bochum.

Kemna, A., Binley, A., Cassiani, G., Niederleithinger, E., Revil, A., Slater, L., Williams, K.H., Flores Orozco, A., Haegel, F.H., Hoerdt, A., Kruschwitz, S., 2012: An overview of the spectral induced polarization method for near-surface applications. *Near Surface Geophysics*. 10(6), 453-468.

Knödel, K., Krummel, H., Lange, G., 2005: Handbuch zur Erkundung des Untergrundes von Deponien und Altlasten. – Band 3, Geophysik, Berlin (Springer).

LaBrecque, D. J., M. Miletto, W. Daily, A. Ramirez, and E. Owen, 1996: The effects of noise on Occam's inversion of resistivity tomography data. *Geophysics*, 61, 538–548.

Leucci, G., De Giorgi, L., 2005: Integrated geophysical surveys to assess the structural conditions of a karstic cave of archaeological importance. *Natural Hazards and Earth System Science*, 5, no. 1, 17-22.

Marshall, D.J., 1959: Induced Polarization, a Study of its Causes. *Geophysics*, 24, 4, 790.

Martel, R., Castellazzi, P., Gloaguen, E., Trépanier, L., Garfias, J., 2018: ERT, GPR, InSAR, and tracer tests to characterize karst aquifer systems under urban areas: The case of Quebec City. *Geomorphology*, 310, 45-56.

Martinez, A. & Byrnes, A.P., 2001: Modelling Dielectric constant values of geological materials: An aid to Ground-Penetrating Radar data collection and interpretation. *Current Research in Earth Science, Bulletin* 247, 1-16.

Martínez-Moreno, F.J., Galindo-Zaldívar, J., Pedrera, A., Teixido, T., Ruano, P., Peña, J.A., ... & Martín-Rosales, W., 2014: Integrated geophysical methods for studying the karst system of Gruta de las Maravillas (Aracena, Southwest Spain). *Journal of Applied Geophysics*, 107, 149-162.

Maurer, H., 2007: Elektromagnetische Verfahren in der Ingenieurgeophysik (Höhere Geophysik C1): Einführung, Geoelektrik und diffusive Verfahren. Institut für Geophysik, ETH-Hönggerberg, HPP O7, CH-8093 Zürich.

Maxwell, J.C., 1864: A Dynamical Theory of the Electromagnetic Field. In: Royal Society Transactions, 155, 1865, S. 459–512.

Meyerhoff, S.B., Maxwell, R.M., Revil, A., Martin, J.B., Karaoulis, M., Graham, W.D., 2014: Characterization of groundwater and surface water mixing in a semiconfined karst aquifer using time-lapse electrical resistivity tomography. *Water Resour. Res.*, 50, 2566-2585, doi:10.1002/2013WR013991.

Navratil, G., 2006: Ausgleichungsrechnung II

Niggli, P., 1948: Gesteine und Minerallagerstätten. Birkhäuser Basel, ISBN 978-3-0348-7171-6.

- Oldenburg, D.W., Li, Y., 1999: Estimating depth of investigation in DC resistivity and IP surveys. *Geophysics*, 64, 403-416.
- Reynolds, J. M. (2011). An Introduction to Applied and Environmental Geophysics, Wiley.
- Robert, T., Caterina, D., Deceuster, J., Kaufmann, O., Nguyen, F., 2012: A salt tracer test monitored with surface ERT to detect preferential flow and transport paths in fractured/karstified limestones, *Geophysics*, 77, 55-67.
- Slater, L., Lesmes, D.P., 2002: Electrical-hydraulic relationships observed for unconsolidated sediments. *Water Resources Research*, 38, 10, CiteID 1213.
- Slater, L., Ntarlagiannis, D., Wishart, D., 2006: On the relationship between induced polarization and surface area in metal-sand and claysand mixtures. *Geophysics*, 71, 2, A1-A5.
- Slater, L., Binley, A., 2006: Synthetic and field-based electrical imaging of a zerovalent iron barrier: Implications for monitoring long-term barrier performance. *Geophysics*, 71, 5, B129-B137
- Spötl, C., Plan, L. & Christian, E. (Ed.), 2016: Höhlen und Karst in Österreich. Linz (OÖ-Landesmuseum).
- Stern, O., 1924: The theory of the electrolytic double-layer. *Zeit. Elektrochem.* Band 30, 508–516.
- Telford, W., Geldart, L., Sheriff, R., 1990: Electrical Properties of Rocks and Minerals. In Applied Geophysics (pp. 283-292). Cambridge: Cambridge University Press.
- Van Hoorde, M., Hermans, T., Dumont, G., Nguyen, F., 2017: 3D Electrical Resistivity Tomography of Karstified Formations Using Cross-line Measurements. *Engineering Geology*, 220, 123-132.
- Watlet, A., Kaufmann, O., Triantafyllou, A., Poulain, A., Chambers, J.E., Meldrum, P.I., Wilkinson P.B., et al., 2018: Imaging groundwater infiltration dynamics in the karst vadose zone with long-term ERT monitoring. *Hydrology and Earth System Sciences*, 22, no. 2, 1563-1592.
- Weigand, M., Flores Orozco, A., Kemna, A., 2017: Reconstruction quality of SIP parameters in multi-frequency complex resistivity imaging. *Near Surface Geophysics*, 15, 187-199.
- Williams, P., 1985: Subcutaneous hydrology and the development of doline and cockpit karst. *Zeitschrift für Geomorphologie*, 29, 463-482.
- Williams, P., Fowler, A., 2002: Relationship between oxygen isotopes in rainfall, cave percolation waters and speleothem calcite at Waitomo, New Zealand. *New Zealand Journal of Hydrology*, 41, 53-70.
- Williams, P., 2008: The role of the epikarst in karst and cave hydrogeology: a review. *International Journal of Speleology*, 37, 1-10.